SAPO-34 ZEOLITE MEMBRANES FOR KRYPTON/XENON SEPARATION

A Dissertation
Presented to
The Academic Faculty

by

Yeon Hye Kwon

In Partial Fulfillment
of the Requirements for the Degree
Doctor of Philosophy in Chemical Engineering
School of Chemical & Biomolecular Engineering

Georgia Institute of Technology
December 2018

SAPO-34 ZEOLITE MEMBRANES FOR KRYPTON/XENON SEPARATION

Approved by:

Dr. Sankar Nair, Advisor
School of Chemical & Biomolecular Engineering
Georgia Institute of Technology

Dr. Krista S. Walton
School of Chemical & Biomolecular Engineering
Georgia Institute of Technology

Dr. David S. Sholl
School of Chemical & Biomolecular Engineering
Georgia Institute of Technology

Dr. Ramesh Bhave
Materials Science & Technology Division
Oak Ridge National Lab

Dr. Carson J. Meredith
School of Chemical & Biomolecular Engineering
Georgia Institute of Technology

Date Approved: August 28th , 2018

Dedicated to my family with love,

Oh Yong, Se Mee, Yeon Soo, and Hak Rae

ACKNOWLEDGEMENTS

This thesis would not have been accomplished without guidance and support from many people around me during my Ph.D journey. I remember the day when I received an email from Prof. Sankar Nair in October 2014 that he decided to let me join his group. I felt like I was on top of the world at that moment and was very thrilled to have a chance to work with him. For about four years of research directed by Dr. Sankar Nair, I have gained invaluable experience on my research field and the trust to pursue my research with his support. Without any doubt, it has been a great honor for me to work with such an intelligent and supportive advisor.

I would also like to thank my thesis committees, Prof. David Sholl, Prof. Krista Walton, Prof. Carson Meredith, and Dr. Ramesh Bhave for their guidance throughout four years of my Ph.D work. I was able to be on track thanks to their insightful comments and fruitful discussion on my research. I wish to thank Dr. Ramesh Bhave especially for being a great collaborator and providing helpful suggestions to complete our project until the end.

I am grateful to my colleagues who provided various insights to my research and also collaborators in our group, Dr. Shaowei Yang for providing a massive amount of alumina hollow fibers and Byunghyun Min for zeolite characterization and distillation modeling. I would also like to thank Dr. Nitish Mittal and Prof. Michael Tsapatsis from University of Minnesota for their great collaboration on membrane modeling chapter. I was lucky to have a couple of nice undergraduate research assistances, Emily Benjamin

and Christine Kiang, who helped me with adsorption and permeation modeling which made my experimental works further reliable.

I want to thank all my friends in Atlanta for making my life wonderful in the U.S. and for making invaluable and unforgettable memories of amazing time we spent together over the years.

My deepest gratitude also goes to my family members with their unconditional love and belief towards me. My mother Se Mee Jang, my father Oh Yong Kwon have been the most supportive people throughout my entire life. Their love and sacrifice brought me to the place where I am now. I would also like to thank parents-in-law, Soon Ok Kim and Il Kyu Lee for their continuous affections. My sister Yeon Soo, a designer who works in a totally different field from me, has always been my best friend with whom I can share anything about myself.

Most importantly, my work is dedicated to my beloved husband, Hak Rae Lee, who have always believed in me and supported me in every single decision I have made for more than seven years. Thank you for being always there for me and I love you.

TABLE OF CONTENTS

LIST OF TABLES

LIST OF FIGURES

SUMMARY

The overall focus of this thesis is to develop and understand zeolitic membranes that can separate mixtures of radioisotope krypton-85 and xenon released as off-gases during used nuclear fuel recycling. The primary advantage of separating ^{85}Kr from Xe is to reduce the volume of radioactive waste for storage. Moreover, revenue is expected by the sale of high-purity Xe. Zeolite membranes are attractive because of their high resistance to radiation degradation and much lower energy requirement compared to cryogenic distillation. However, there is currently very little knowledge in the literature regarding the properties of zeolite materials and membranes for Kr/Xe separation. In this thesis, a detailed study of silicoaluminophosphate zeolite SAPO-34 materials and membranes is carried out and a potential role of membrane system is investigated for Kr/Xe separation.

The first Chapter presents the overview of used nuclear fuel reprocessing and the current technology for separating Kr and Xe mixture released as off-gas. Even though cryogenic distillation is the most mature gas separation technology, researchers look for alternative approaches due to high energy duty and safety concerns on cryogenic distillation. Zeolite membranes are assumed to be a great candidate for separation of Kr/Xe because they can separate molecules with very small molecular size differences (<0.1 nm) and because of their high radiation stability.

In Chapter 2, the adsorption and diffusion properties of Kr and Xe are investigated in SAPO-34 under various conditions. The main focus of this Chapter is a quantification of adsorption and diffusion behavior of Kr and Xe in SAPO-34, due to lack

of information on transport behavior of noble gases in zeolite materials. The mixture adsorption behavior of Kr and Xe is also examined using IAST and a double Langmuir model. Xe shows stronger adsorption than Kr in both single-component adsorption experiments and binary adsorption predictions. However, Kr shows much faster diffusion than Xe with a considerably lower activation energy of diffusion. Preliminary results confirm that SAPO-34 membrane is a promising candidate for Kr/Xe separation since favorable Kr diffusion selectivity would outcompete the stronger adsorption of Xe.

In order to justify the hypothesis on adsorption and diffusion selectivity of Kr and Xe, Chapter 3 deals with the synthesis of SAPO-34 membrane with high Kr/Xe selectivity and measurement of permeation properties of Kr and Xe in SAPO-34 membrane. Generally, it is difficult to obtain a compact seed layer on a low-quality macroporous substrate by conventional dip-coating or rub-coating seeding method. Therefore, steam-assisted conversion (SAC) seeding method is demonstrated in this Chapter by transforming a reactant paste into a compact seed layer with the aid of steam. Defect-free SAPO-34 membrane is synthesized on macroporous α-Al_2O_3 substrate using SAC seeding followed by the secondary growth, which can be confirmed by very low permeance of SF_6. Single component permeation results show the clear molecular sieving properties, and permeability results from of different gas molecules is comparable to other reported literature data. The detailed binary mixture permeation measurement reveal that SAPO-34 membrane have Kr permeance of ~ 10 GPU with Kr/Xe separation selectivity 12 – 25, with the highest selectivity at the lowest measurement temperature (255 K).

Even though defect-free SAPO-34 membranes are successfully synthesized, there is much potential for engineering the separation properties of these membrane with a view to improving selectivity and permeance. Therefore, three aspects can be taken into accounts to minimize the possible issue of high manufacturing cost of zeolite membranes; (1) improvement on Kr permeance without sacrificing Kr/Xe selectivity, (2) improvement of Kr/Xe permselectivity, and (3) scalability and low-cost fabrication of zeolite membranes. The first objective is achieved by reducing of the thickness of the membrane *via* a control of the amount of SAC paste per unit area. Thickness-reduced SAPO-34 membrane shows highly improved Kr permeance with slightly improved ideal selectivity due to well-interlocked crystals comprising the membrane. Secondly, Kr/Xe permselectivity is improved by post-synthesis monovalent cation exchange with Li^+, Na^+ or K^+ with a slight decrease in Kr permeance. Permeation measurements show that monovalent cation exchange in SAPO-34 results in tuning the effective pore size which can also be confirmed from adsorption and diffusion properties. Finally, scalability issue is expected to be solved by successful transfer of optimized synthesis protocol to ceramic hollow fiber supports. The consistent performance of membrane on ceramic hollow fiber and on disk type support reveal that this results will realize a compact and a low cost system.

In Chapter 5, the zeolite membrane system for Kr/Xe separation is evaluated as an alternative to cryogenic distillation. For the technoeconomic analysis of the membrane system, a predictive Maxwell-Stefan model of Kr/Xe permeation is developed in SAPO-34 membranes under various conditions. This M-S membrane model can then be integrated into an overall process model to estimate the size of the system and the

required cost for membrane system operation. The membrane cascade is a suitable configuration due to a small number of stages and its mild operating condition. The size of membrane system is calculated as only 13 m^2 in order to achieve 90 % Kr and 99.7 % Xe as product streams from feed mixture with 10 % Kr and 90 % Xe. Compared to cryogenic distillation, membrane system can save 70 % of energy cost and 40 % of capital cost, based on the calculation from ASPEN Plus. Therefore, SAPO-34 membrane system for Kr/Xe separation is expected to be highly favorable from its economically attractive features.

CHAPTER 1. INTRODUCTION

1.1 Used Nuclear Fuel Reprocessing and Off-gas Release

Nuclear energy is an important resource in addressing the problem of depletion of nonrenewable fossil fuels [1, 2]. In 2017, almost 20% of total electrical output in the U.S. was generated using nuclear energy with 99 nuclear reactors and two more new units are expected to be ready in 2021 [3]. Although nuclear energy is considered to be a clean and economical means of carbon-free energy which comprises 63% of carbon-free electricity in the U.S. [3], it also requires complex systems for nuclear waste management. The amount of waste is small in volume since nuclear power is produced by a very small amount of fuel. However, much of the waste products are radioactive with extreme effects on human health and environment, and therefore must be carefully managed as hazardous material. In order to safely dispose all radioactive waste byproducts and to recycle all used nuclear fuel, the U.S. has agreed to develop a closed nuclear fuel cycle [4]. Nuclear fuel is produced from fissionable materials such as uranium and plutonium through the nuclear fuel cycle, and used nuclear fuel (UNF) can be recycled through a set of reprocessing steps.

Reprocessing of UNF should be considered for several reasons such as recovery of valuable fissile components for subsequent reuse in recycle fuel, reduction in the volume of high-level waste and recovery of specific isotopes. **Figure 1.1** shows a proposed overall process for recycling UNF based upon work performed by the ORNL fuel cycle R&D group. The fuel bundle which contains fuel pins can be sheared and chopped into segments of 1–2 inches in length using shear blades. During voloxidation,

oxide fuel is heated with oxygen at 450 – 650 ^{o}C and UO_2 reacts with oxygen to form U_3O_8. A relatively fine powder (~ 44 µm) is generated due to a thermal expansion [5]. The fuel powder is then converted into aqueous chemical form suitable for subsequent separation steps during acid dissolution with nitric acid. The off-gas stream is generated during the shearing and chopping, voloxidation and acid dissolutions steps with ~2500 L/min flow rate assuming a typical 800 tons fuel/yr reprocessing facility.

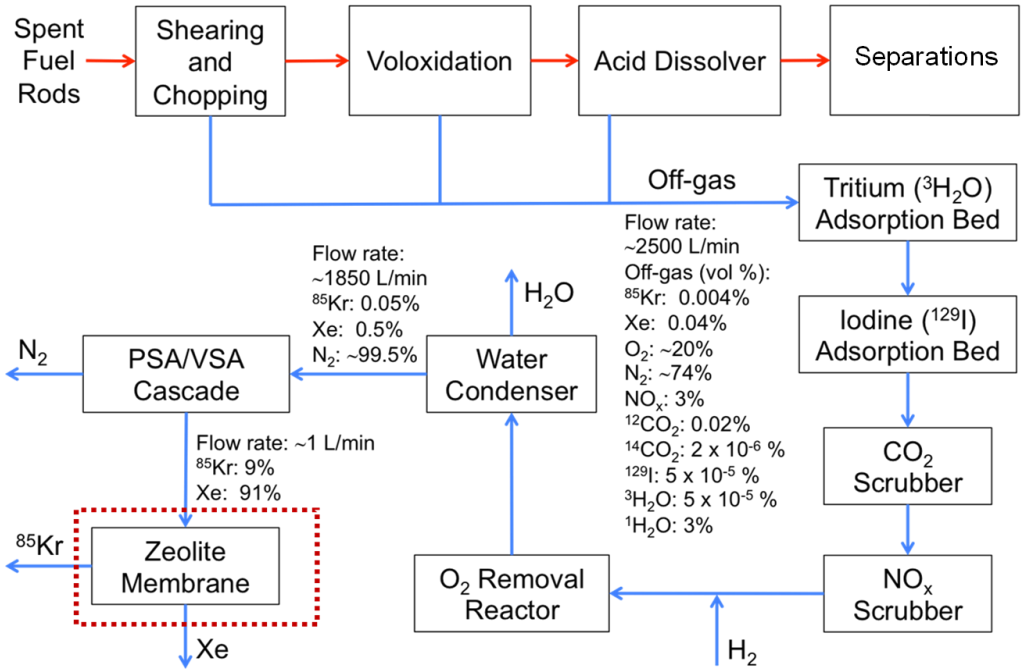

Figure 1.1. Process flow diagram for proposed off-gas treatment process [6, 7].

The off-gases from the initial steps are combined to obtain a stream that contains N_2, ^{129}I (radioisotope), NO, NO_2, CO_2 containing ^{14}C (radioisotope), ^3H_2O (radioactive tritium oxide), ^{85}Kr (radioisotope), and ^{136}Xe [8-10]. Capturing and separating each radioisotope is essential to minimize the volume of high-level radioactive waste for storage. Before the off-gas enters the tritium removal step, all the tritium is converted to tritiated water (^3H_2O) while flowing through a copper catalyst. The tritiated water is proposed to be removed by adsorption processes in type 3A zeolite and or anhydrous

$CaSO_4$. A number of technologies are being developed for the recovery of ^{129}I, including silver-exchanged solid sorbents or liquid scrubbing. Radioactive CO_2 and NO_x removal is proposed to be carried out with NaOH scrubbers. Any oxygen present in the off-gas would then be reacted with hydrogen over a Pd-Pt catalyst and condensed out as water. A series of zeolite-based pressure swing adsorption (PSA) or vacuum swing adsorption (VSA) steps are proposed to capture N_2 using existing technology. Alternatively, new adsorbents are under development that may allow capture and concentration of the noble gases Kr and Xe while rejecting N_2.

The last step in this process (Kr separation from Xe) is the subject of this research program. ^{85}Kr is a radioactive isotope which has a half-life of 10.7 years and cannot be released to the environment. Although Xe is generated as a fission product, all the radioactive isotopes (e.g. ^{127}Xe and ^{135}Xe) decay to very low concentration and only non-radioactive ^{136}Xe remains in the off-gas [11]. The Kr/Xe mixture is approximately 10/90 by volume and hence the separation of Kr would reduce the volume of radioactive ^{85}Kr waste for storage by a factor of ~10. There is no existing process for this separation that is suitable for use in UNF recycling. Kr/Xe separation is challenging since they are both chemically inert species and physically very similar (0.036 nm size difference). The high-quality separation of ^{85}Kr/Xe yields two main advantages: reducing the volume of radioactive waste and generating possible revenue from the sale of purified Xe which is a high-value gas (currently ~$8,000/kg) used in lighting and medical applications.

1.2 Krypton/Xenon Separation Technologies

1.2.1 Cryogenic Distillation

Cryogenic distillation is a commercially used and the most mature separation process, especially for separate gases from air. Gas separation by cryogenic distillation involves the separation of its components based on their different boiling points and volatilities. The boiling points of Kr and Xe are 120 K and 165 K, respectively, thus the operating temperature of the distillation column should be maintained between the boiling points of two gaseous components. Even though cryogenic distillation is a primary method to capture and separate radioactive Kr and Xe, researchers seek alternative approaches due to the high cost, large footprint, and safety concerns on cryogenic distillation.

1.2.2 Adsorption

Activated carbon or zeolite molecular sieves are traditional adsorbents that can be used for Xe/Kr separations. Even though the overall capacity of activated carbon was found to be high, the selectivity of Xe/Kr was only 2-3, which is considered too low for future use in nuclear reprocessing plants [12, 13]. Zeolite molecular sieves such as NaX and NaA have also been evaluated after ion-exchange with Xe/Kr selectivity of 4 – 6 [14]. However, the cations in the zeolite pores hindered Xe from being sufficiently adsorbed to the zeolite pores and hence the adsorbents are considered too low in capacity. Recent studies reported the potential of MOF materials that can perform Xe/Kr separations [15-19]. MOF adsorbents have advantages of high surface area and capacity compared to traditional porous adsorbents such as activated carbon. Wang et al

synthesized MOF-Cu-H with pore-cage structure which had Xe adsorption selectivity ~16 in a mixture (10% Kr/90% Xe) [20]. This is the one of the highest separation factors reported to date. Banerjee et al. suggested a scheme for separating Xe and Kr from off-gas as pure streams of Kr and Xe (**Figure 1.2**). They proposed from their molecular simulation results that the ideal MOF for the separation of Xe/Kr should have one or more properties among the following: (a) unsaturated metal centers on the pore surface, (b) narrow and uniform pores which are slightly larger than kinetic diameter of the adsorbates Xe and Kr, and (c) temperature-dependent separation of the gas mixture [16]. However, large-scale commercial use or economic analysis of MOF-based materials for noble gas separations has not yet been reported. More detailed studies on the future use of MOFs for Xe/Kr separation should follow in order to apply this technique to an industrial use.

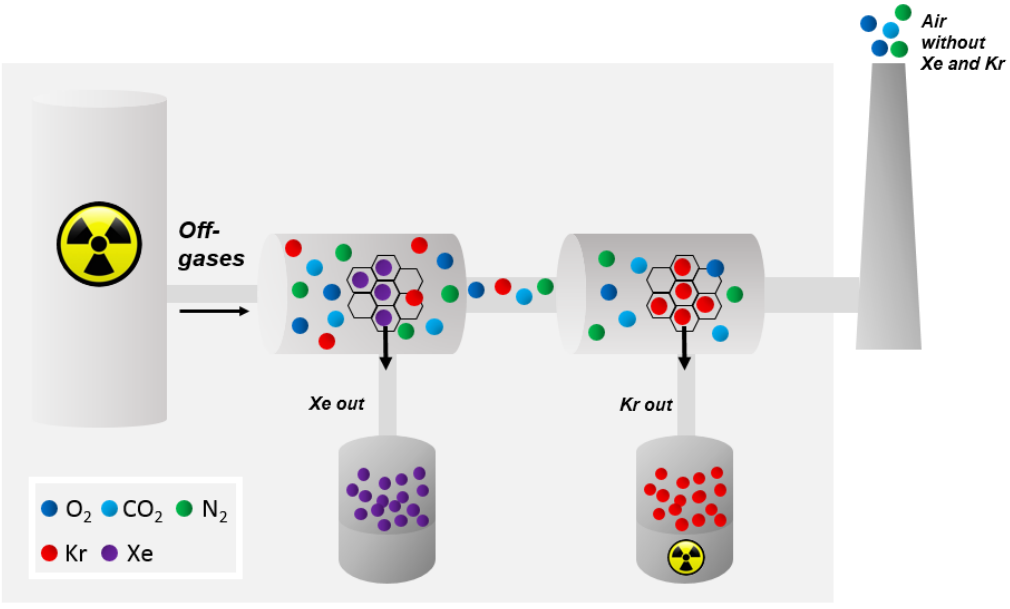

Figure 1.2. Potential Metal-organic frameworks adsorption bed for separation of Xe/Kr (scheme adapted from [16])

1.2.3 Membranes

A main advantage of membrane technology is that membrane system facilitates *continuous* operation over a *range of temperatures and pressures* close to ambient conditions, unlike cryogenic distillation or adsorption. Since it does not involve low-temperature phase transformation, membrane separation process can be a potential energy-saving method. Wu et al. reported that zeolitic imidazolate framework-8 (ZIF-8) membranes could separate Kr/Xe with Kr permeance in the range of 6 – 51 GPU and Kr separation selectivity as high as 14 [21]. ZIF-8 has an effective aperture size of ~0.4 nm and it showed a possibility of separating Kr/Xe due to its molecular sieving properties. However, a sharp molecular sieving effect was not seen due to the well-known dynamic flexibility of the ZIF-8 aperture [22]. It was also reported that membranes of microporous aluminophosphate AlPO-18 can separate Kr [23]. AlPO-18 has an average pore size ~ 0.38 nm with AEI topology which is generally used for CO_2/CH_4, CO_2/N_2, and H_2/CH_4 separations [24, 25]. Due to its high adsorption selectivity for Xe and the presence of non-zeolitic pathways, the AlPO-18 membrane showed relatively low Kr/Xe permselectivity ~6. These studies showed that Kr and Xe can be separated using nanoporous inorganic membranes, but significant improvements in performance are desired for a sharp separation of Kr/Xe by utilizing the chemical properties of inorganic materials. Furthermore, the scale-up and production of microporous membranes for Kr/Xe separation is also a significant issue [26, 27]. Unlike the case of high-volume commodity separations, the fuel cycle separation of noble gases is a specialty application that may offer a more near-term opportunity for scaling and demonstration of microporous membranes.

1.3 Membrane-based Gas Separations

Membrane-based gas separation is typically a pressure-driven process that has emerged as a competitive separation technology in different industrial applications since 1980, starting from the large-scale commercial production of polymeric membranes [27]. A membrane material can be chosen based on its physical and chemical properties for specific gas separation applications. Here I outline briefly the different classes of membrane materials.

1.3.1 Polymeric Membranes

A large number of polymers have been studied and developed for membrane applications due to their ease of processability. There are mainly two types of polymeric membranes in use; rubbery polymers and glassy polymers [27, 28]. Rubbery polymers generally possess higher permeability due to a large amount of free volume, and polydimethylsiloxane (PDMS) and silicon rubber composite membranes are general examples. The permselectivity of rubbery polymers is governed by the differences in the condensability of the gas species. Therefore, relatively large molecules with higher solubility (e.g., organic vapors) are more permeable than small gas molecules such as N_2. Glassy polymers have been more widely used for gas separation. Unlike rubbery polymers, molecules can be separated by their dimensions in the glassy polymers. One of great examples of glassy polymer for gas separation applications is polyimides (PI) which are mechanically robust and thermally stable [29]. However, polymeric membranes in general have the disadvantage that their performance is limited by the so-called Robeson trade-off relationships between gas permeability and selectivity (**Figure 1.3.**) [30, 31],

wherein the log-log plots of selectivity versus permeability show clear “upper bounds” on performance. Other than the upper bound, there is one more important factor relevant to fuel cycle applications: little is currently known about the long-term radiation stability of polymeric materials and the rate of formation of radiation-induced defects or morphological changes.

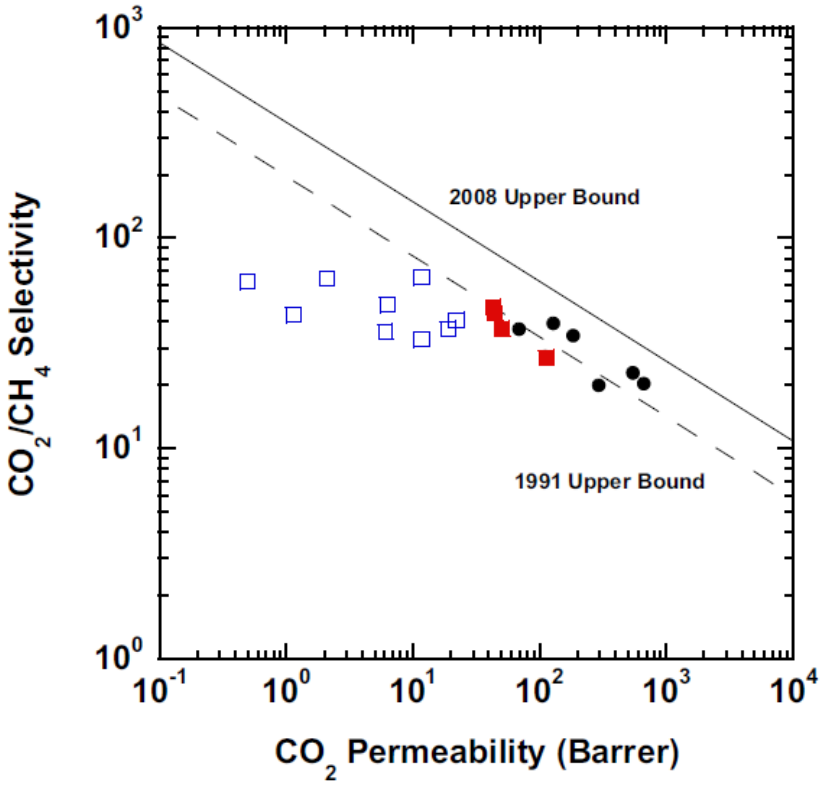

Figure 1.3. Robeson upper bound plot for CO2/CH4 separations. First generation polyimides (□) from Ref. [32]. Current generation polyimides (●) from Refs. [33-35]. Treated polyimides (■) from Ref.[33].

1.3.2 Zeolite Membranes

Zeolites are microporous crystalline aluminosilicates, composed of T-atoms (T = Si, Al) connected by oxygen atoms (O-bridges), forming tetrahedral TO_4 units. Other than Si or Al, different elements such as phosphorus, germanium, or zinc can also be T-

atoms in zeolite materials [36]. Due to their highly ordered pore and channel structures, zeolites have been extensively studied as molecular sieving membranes for various gas or liquid separations [37-40]. Zeolite membranes can separate molecules that may have very small molecular size differences (< 0.1 nm) due to its rigid pore structure. **Figure 1.4** shows the framework projections and the ring size for commonly studied frameworks. The crystalline characteristics of the framework shows that the pore openings are uniform throughout the crystal and can readily separate molecules even with small size differences.

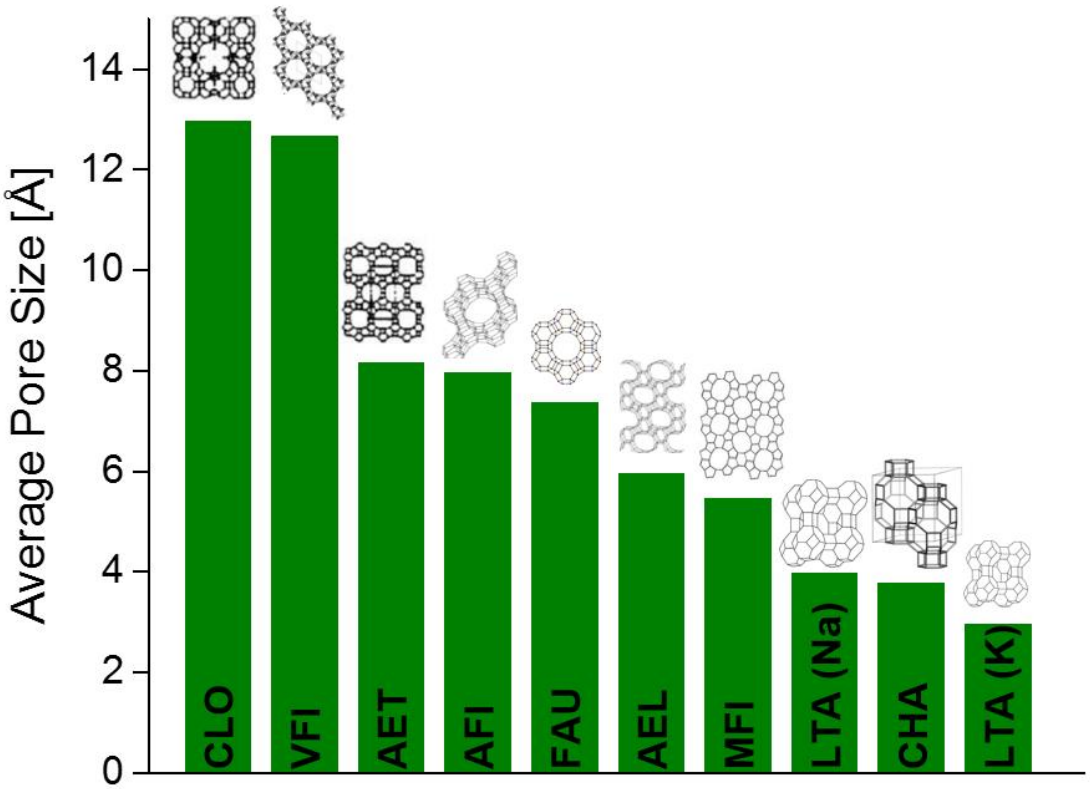

Figure 1.4. Comparison of pore sizes of different framework structures (adapted from Ref. [41])

Many types of zeolite materials (e.g. MFI, LTA, FAU, CHA) have been studied as zeolite membranes. The first commercial application of zeolite membranes was alcohol dehydration using LTA type membranes developed by Kita et al. [42] . However, issues still exist for the further industrial applications, due to the challenges in membrane fabrication (such as membrane defect control) and the high capital costs (most importantly the cost of ceramic support materials) [43]. Therefore, reducing the capital cost of zeolite membranes is desired in order to enable industrial applications, by the improvement of the flux, selectivity, and membrane fabrication on scalable/economical supports.

1.3.3 SAPO-34 zeolite membranes for gas separation

SAPO-34 is a silicoaluminophosphate zeolite which has chabazite (CHA) topology with a pore size of 0.38 nm. SAPO-34 has been widely studied for light gas separation, especially for CO_2/CH_4 separations [26, 44, 45]. Li et al reported that average CO_2/CH_4 separation selectivity of SAPO-34 was ~250 with CO_2 permeance of approximately 1500 GPU. I hypothesized that SAPO-34 membranes can separate Kr and Xe since the pore size of SAPO-34 (0.38 nm) is intermediate between the kinetic diameters of the two gases (**Figure 1.5**). However, there are several interesting differences between Kr/Xe separation and CO_2/CH_4 separation with small-pore zeolite (*e.g.*, SAPO-34) membranes. The Kr/Xe case is more challenging since it is expected to be influenced by competing effects of diffusion selectivity (favoring Kr) and adsorption selectivity (favoring Xe)[12, 46, 47], whereas in the CO_2/CH_4 case the diffusion and adsorption selectivities both favor CO_2. Therefore, it is important to understand the transport properties of each gas in

SAPO-34 thorugh a detailed study of their adsorption, diffusion and permeation properties using experimental techniques as well as modeling methods.

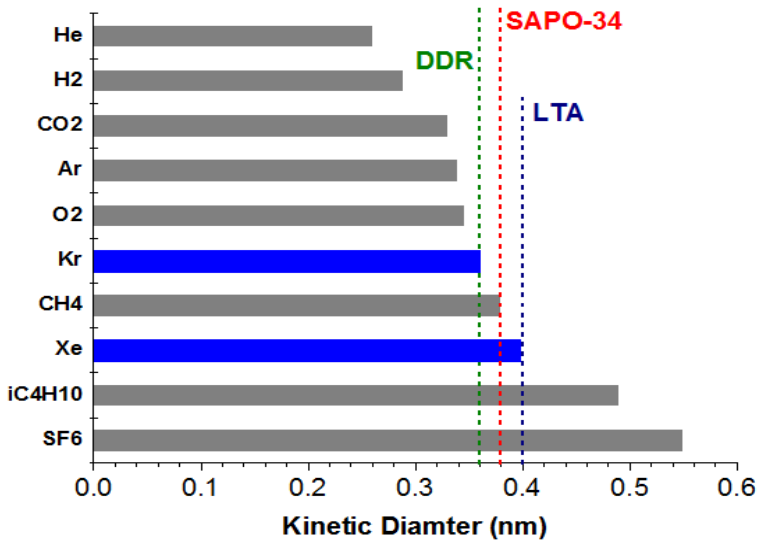

Figure 1.5. Kinetic diameter of various molecules including Kr and Xe and pore size of candidate zeolite materials with different pore size

1.4 Transport Mechanisms in Zeolite Membranes

The permeation flux of a gas component may be determined by the adsorption and diffusion characteristics of all the components in the mixture. Since the separation properties cannot be determined by single component data alone, an appropriate description of zeolite membrane permeation should be carried out with proper assumptions [48, 49]. Here we briefly review the key aspects of gas transport in zeolite membranes.

1.4.1 Single-Component Adsorption

Different types of adsorption models for gas components have been developed empirically, including linear, Langmuir, and Freundlich adsorption model etc., depending on the adsorption behavior (**Figure 1.6**) [50, 51].

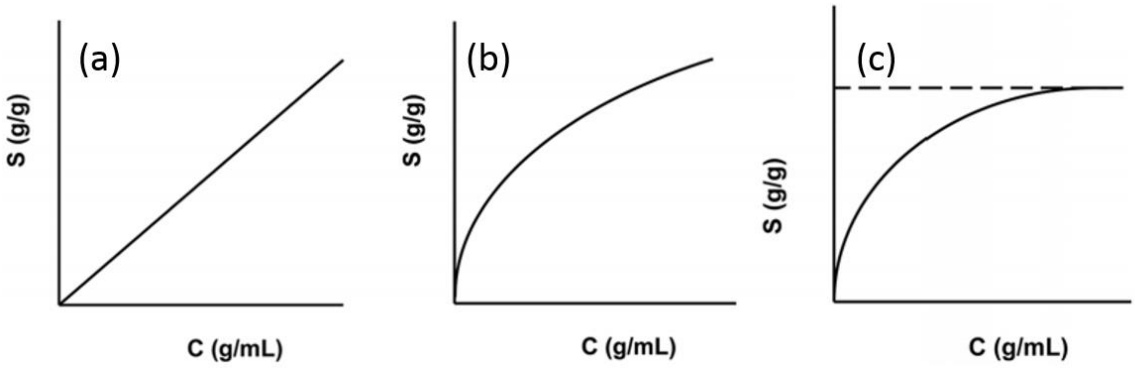

Figure 1.6. Schematics depicting the form of the adsorption isotherm equations: (a) Linear, (b) Freundlich adsorption isotherm, (c) Langmuir adsorption isotherm.

Among them, the Langmuir isotherm assumes that the adsorption takes place at specific homogeneous sites on the surface of the adsorbent and form a monomolecular adsorbed layer, which can be expressed as the following equation;

$$q = \frac{q_{sat} bp}{1 + bp} \tag{1.1}$$

where q is the adsorbate concentration in the sample, q_{sat} the saturation coverage, p the pressure and b the Langmuir constant which can be expressed in terms of the enthalpy of adsorption (ΔH_{ads}) and the pre-exponential entropic factor $b_o = \exp(\Delta S_{ads}/R)$. Langmuir adsorption isotherm assumes four hypotheses. (1) The surface of the adsorbent is uniform and adsorption sites are equal. (2) Adsorbed molecules do not interact. (3) Every adsorption occurs *via* the identical mechanism. (4) At the maximum adsorption, a

monolayer is formed and adsorption only occurs on the free surface of the adsorbent; molecules of adsorbate do not deposit on already adsorbed molecules.

1.4.2 Multicomponent Adsorption

Since the separation occurs from a mixture, multicomponent adsorption equilibria must be considered in the design of zeolite membrane systems. The multicomponent adsorption is usually determined by models based on the information obtained from single component isotherms. Since it is rather difficult to validate the results experimentally, they can alternatively be validated by molecular simulations [50, 52, 53]. For a simple prediction, binary mixture adsorption predictions can be made using the double Langmuir isotherm, with the adsorption parameters already determined from the single-component Langmuir isotherms (Equation 1.1).

$$q_i = \frac{q_{i,sat} b_i p_i}{1 + \sum_{j=1}^{2} b_j p_j} \tag{1.2}$$

where q is the loading in the sample, q_{sat} the saturation coverage, p the pressure and b the Langmuir constant.

In 1965, ideal adsorption sorption theory (IAST) was developed by Prausnitz and Myers, which predicts multicomponent adsorption selectivity more precisely [52]. IAST can be used for accurate prediction of binary adsorption isotherms using the adsorption isotherms of pure Kr and Xe. This theory is analogous to Raoult's law of vapor-liquid equilibrium model with additional equations on adsorbed phases. The chemical potential of adsorbed phase can be estimated equal to the gas phase at equilibrium. For binary component *i* and *j* in the assumption of ideal mixing, the equation is:

$$y_i P = x_i P_i^o \tag{1.3}$$

Here, y_i represents the adsorbed phase and x_i is the molar fraction of i in gas phase. P_i^o and P are pressure of component i in gas phase and total pressure, respectively. The reduced spreading pressure (ψ_i) of the adsorbed phase is calculated as:

$$\psi_i = \int_0^{p_i^o} \frac{q_i}{p_i} dp_i = \int_0^{p_j^o} \frac{q_j}{p_j} dp_j \tag{1.4}$$

By assuming ideal mixing, the total adsorbed amount (q_t) can then be calculated as:

$$\frac{1}{q_t} = \sum_i \frac{x_i}{q_i(P_i^o)} \tag{1.5}$$

with the constraint $\sum_i^N x_i = 1$. A two phase model selectivity can be defined as the ratio of mole fraction of component i in the adsorbed state (y_i) over the mole fraction of Xe in the gas phase (x_i) divided by the same correlation of component j ($y_j$and x_j).

$$S_{i/j} = \frac{y_i/x_i}{y_j/x_j} \tag{1.5}$$

One of the main disadvantages of IAST is that it assumes ideal mixing of multicomponent. Therefore, it is inappropriate to describe the adsorption behavior of non-ideal mixture with hydrogen bonding effects such as water-ethanol mixture in zeolite materials. Nevertheless, it is adequate to use this theory for the adsorption of Kr-Xe mixture in SAPO-34 zeolite since both components are chemically inert and interact relatively weakly with each other and with the zeolite pores by van der Waals interactions.

1.4.3 Diffusion

For the effective use of zeolite membranes in separation applications, a proper description of diffusive transport in zeolite materials is required [54]. Among several diffusion-related quantities, the *transport diffusivity* can be phenomenologically defined by the net gas flux divided by a concentration (or pressure) gradient as described in Fick's law (Eq. 1.6.), where *J* is diffusion flux, *C* is concentration and *D* is transport diffusivity [55].

$$J_i = -D_i \frac{dC_i}{dx} \tag{1.6}$$

Transport diffusivity is strongly affected by the adsorption equilibrium and diffusion mechanism, and thus cannot be easily associated with a simple molecular interpretation. Therefore, a more fundamental concept is desired to describe the molecular level understanding for macroscopic transport. The *Maxwell-Stefan (M-S) diffusivity* is a thermodynamically corrected diffusivity which can be taken as representing the intrinsic rate of diffusive hopping of molecules in the zeolite pores. Transport diffusivity and M-S diffusivity can be correlated as:

$$D_i = \mathbb{D}_i \Gamma \tag{1.7}$$

where Γ is the thermodynamic correction factor defined as:

$$\Gamma \equiv \theta_i \frac{\partial ln p_i}{\partial \theta_i} \tag{1.8}$$

A third quantity called the *self-diffusivity* is determined as the diffusivity directly arising from a random walk of a molecule in the porous material under conditions where the chemical potential gradient is zero ($\nabla\theta_i \equiv 0$). **Figure 1.7** shows the comparison between self, Maxwell-Stefan and transport diffusivities, and at zero loading, all three diffusivities are identical each other.

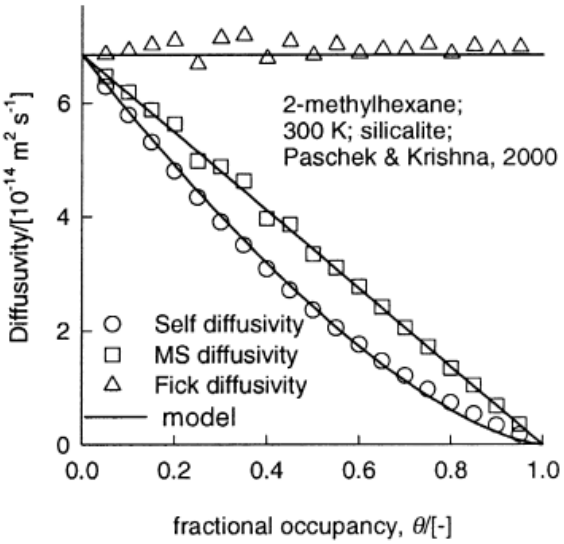

Figure 1.7. Relationship between self, Maxwell-Stefan and transport diffusivities of 2-methylhexane in silicalite at 300 K.(Reproduced from [54])

1.4.4 Permeation through Zeolite Membranes

Transport through zeolite membranes occurs by diffusion in the pores. Surface diffusion occurs when the molecules adsorb onto the inner surface of the pores and then travel through the pores by successively desorbing and adsorbing onto adjacent adsorption sites across the length of the membrane. Consider a membrane of thickness δ, which separates two well-mixed compartments (**Figure 1.8**). We ignore the external mass

transfer resistances to the membrane and assume the transfer fluxes is solely determined by intramembrane transport.

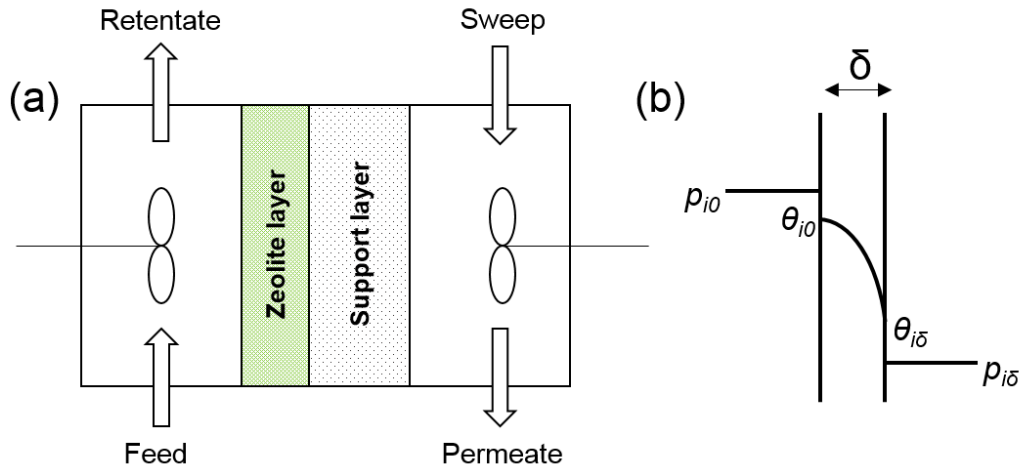

Figure 1.8. Schematic representation of (a) zeolite membrane setup and (b) loading profile within the zeolite membrane without effect of support layer

The steady-state transmembrane flux for single gaseous component across a membrane is

$$N_i = \frac{P_{Mi}}{\delta}\left(p_f - p_p\right) = \overline{P_{Mi}}(p_f - p_p) \tag{1.9}$$

where N_i is the steady-state molar transmembrane flux, P_{Mi} is the permeability of *i* across the membrane, $\overline{P_{Mi}}$ is the permeance of component *i*, δ is the thickness of the membrane, p_f and p_p are the pressure of feed and permeate, respectively. Permeability of the membrane can be calculated from the pressure difference between feed and permeate side and thickness normalized gas flux. The measure permeance ($\overline{P_{Mi}}$) is the effective permeance which is the combined permeance of zeolite layer and support layer (**Figure 1.8a**).

$$\frac{1}{\overline{P_{Mi}}} = \frac{1}{\bar{P}_{Mi,zeolite}} + \frac{1}{\bar{P}_{Mi,support}} \tag{1.10}$$

The ideal selectivity of component *i* over *j* ($\alpha_{i,j}$, *i* is the more permeable component) can then be defined as the permeance ratio of *i* over *j*:

$$\alpha_{i,j} = \frac{\bar{P}_{Mi,zeolite}}{\bar{P}_{Mj,zeolite}} \tag{1.11}$$

1.5 Objectives and Aims

The overall goal of this thesis is to develop a SAPO-34 membrane technology that can separate Kr/Xe mixtures relevant to used nuclear fuel (UNF) reprocessing. This aim is pursued *via* the development of scalable approaches for fabrication of high-performance SAPO-34 membranes, detailed investigation of transport properties, and a preliminary analysis of its economic potential. These aspects are summarized in the form of four specific objectives as follows:

A. *Understanding intrinsic krypton and xenon adsorption and diffusion behavior in SAPO-34 materials.*

   A main feature of this work is to synthesize SAPO-34 crystals with appropriate dimensions and investigate the adsorption and diffusion parameters which can be experimentally obtained from the isotherm. Due to lack of information on transport behavior of noble gases in zeolite materials, this study focuses on the quantification of adsorption and diffusion properties of Kr and Xe in SAPO-34.

Additionally, IAST and double Langmuir models are used to examine the mixture adsorption behavior of Kr and Xe in SAPO-34.

B. *Synthesis of SAPO-34 membranes and permeation properties of Kr and Xe*.

One of the major issues in the fabrication of zeolite membranes on macroporous ceramic substrates is to synthesize high-quality membranes with high reproducibility. SAPO-34 membranes are synthesized *via* a steam-assisted conversion (SAC) seeding technique followed by hydrothermal secondary growth. By the SAC method, a compact seed layer is formed by the transformation of reactant paste to seed crystals on the α-alumina substrate. In this work, SAC method is introduced to prepare defect-free SAPO-34 membranes with high Kr/Xe selectivities.

C. Enhancement of SAPO-34 membrane performance for Kr/Xe separation.

High manufacturing cost of zeolite membrane is one of the main factors which hinders the industrial use of zeolite membranes. There are three aspects that we can take care of in order to reduce the system size and cost for membrane system for gas separation, which will be main features of this work. Firstly, we study in detail the reduction of membrane thickness through a recently reported membrane fabrication method referred to as steam-assisted conversion (SAC). By reducing the thickness of the membrane, it is possible to achieve corresponding increase in flux through the membrane. Secondly, detailed study of cation exchange of SAPO-34 membranes is conducted with the objective of increasing the Kr permeation selectivity. The reproducibility of zeolite membrane properties

is also investigated. Finally, the issue of scalability and low-cost fabrication of zeolite membranes is addressed by transferring the optimized SAC and ion-exchange methods to ceramic hollow fiber substrates, and I demonstrate the fabrication of SAPO-34/α-alumina hollow fiber membranes with separation characteristics consistent with those of the membranes developed on disk substrates.

D. Zeolite membrane transport modeling and technoeconomic analysis.

The goal of this work is to first develop a predictive Maxwell-Stefan model of Kr/Xe permeation in SAPO-34 membranes. M-S model describes the permeation through the zeolite membrane mathematically and explains the interplay between adsorption and diffusion. Among 5 different types of membranes introduced in the previous chapters, the best membrane with the highest selectivity is chosen and then M-S model is integrated into an overall model of a cross-flow tubular membrane module in order to predict the size of gas separation system to achieve the desired specifications of products. Finally, by using the information obtained from the crossflow model, a system analysis is performed in order to calculate the required capital cost and operating cost including maintenance and energy cost per year. This component of the work has been carried out in collaboration with Prof. Michael Tsapatsis and Dr. Nitish Mittal at the University of Minnesota.

1.6 Potential Impact of This Work

In this thesis, three main advances are addressed which support the off-gas capture and separation strategy proposed by DOE. Firstly, it is shown that the adsorption,

diffusion, and permeation behavior of Kr and Xe in SAPO-34 crystals membranes, which indicate their high potential for the use in Kr-Xe separation membranes. This achievement includes the use of steam-assisted conversion (SAC) seeding method that can be applied to any type of substrates with different geometry with high reproducibility. In particular, we expect that successful synthesis of zeolite membranes on ceramic hollow fibers supports will broaden the spectrum of zeolite membranes in the industrial applications. Secondly, this work shows the optimized synthesis protocol of SAPO-34 membrane. In order to reduce the required system size, thickness reduction and cation exchange strategy are used to improve the gas flux and separation selectivity of Kr/Xe. The membrane thickness is controlled by simply changing the amount of SAC paste, whereas previous studies have focused on thickness reduction by controlling the secondary growth condition or the size of seed crystals. This methodology presents a different aspect of the thickness reduction of zeolite membrane without any need to optimize the other parameters. In addition, a detailed study on cation exchange of SAPO-34 membranes provides insights on controlling the selectivity by changing the effective pore size of SAPO-34. By transferring the optimized SAC and ion-exchange method to ceramic hollow fiber substrates, the scalability and low-cost fabrication of zeolite membranes are expected to be realized. Finally, a systematic and critical engineering analysis of membrane process for gas separation is addressed in this study. This work includes the comparison between the experimental data and the system modeling by using Maxwell-Stefan equation for a gas separation system. To our best knowledge, the techno-economic analysis of zeolite membrane system is lacking for gas separation application which can substitute the conventional separation method (e.g. cryogenic

distillation). Therefore, a potential role of membrane permeation system is clarified in this work by determining the system size, capital cost and operating cost. Overall, this work will bring us closer to the real use of zeolite membranes for an efficient separation of Kr/Xe mixtures from spent nuclear fuel recycling into pure gas streams.

CHAPTER 2. UNDERSTANDING KRYPTON AND XENON ADSORPTION AND DIFFUSION BEHAVIOR IN SAPO-34[1]

2.1 Introduction

As described in Chapter 1, zeolite membranes can provide an attractive alternative to conventionally used energy intensive separation processes for Kr/Xe separation. Zeolitic molecular sieve membranes offer an opportunity to exploit the size difference of Kr (kinetic diameter 0.36 nm) and Xe (0.396 nm) to obtain preferential permeation of the minority component (Kr) from the mixture, thereby achieving an efficient separation with low energy requirements. A schematic of a zeolite membrane is shown in **Figure 2.1**. The membrane structure is composed of a zeolite membrane layer on a macroporous support. When a binary gas mixture is fed from the feed side, molecules in the feed stream adsorb into the nanopores of the membrane, diffuse through the nanopores to the permeate side, and then desorb into the permeate stream.

The zeolite SAPO-34 has chabazite (CHA) topology with a well-defined 0.38 nm pore aperture which is hypothesized to be ideally suited for Kr/Xe separation by molecular sieving. SAPO-34 is known to be useful for gas separations such as CO_2/CH_4 or CO_2/N_2 [26, 44, 56, 57]. There are several interesting differences between Kr/Xe separation and CO_2/CH_4 separation with small-pore zeolite (*e.g.*, SAPO-34) membranes. The Kr/Xe case is more challenging since it is expected to be influenced by competing

[1] Reprinted with permission from Y. H. Kwon, C. Kiang, E. Benjamin, P. Crawford, S. Nair, R. Bhave, "Krypton-xenon separation properties of SAPO-34 zeolite materials and membranes", AIChE Journal, 63, pp. 761-769. Copyright 2017 John Wiley & Sons.

effects of diffusion selectivity (favoring Kr) and adsorption selectivity (favoring Xe) [12, 46, 47], whereas in the CO_2/CH_4 case the diffusion and adsorption selectivities both favor CO_2. Therefore, for determining the permeation through zeolite layer, it is necessary to fundamentally understand the transport phenomena underlying the membrane operation such as adsorption and diffusion through the zeolite materials.

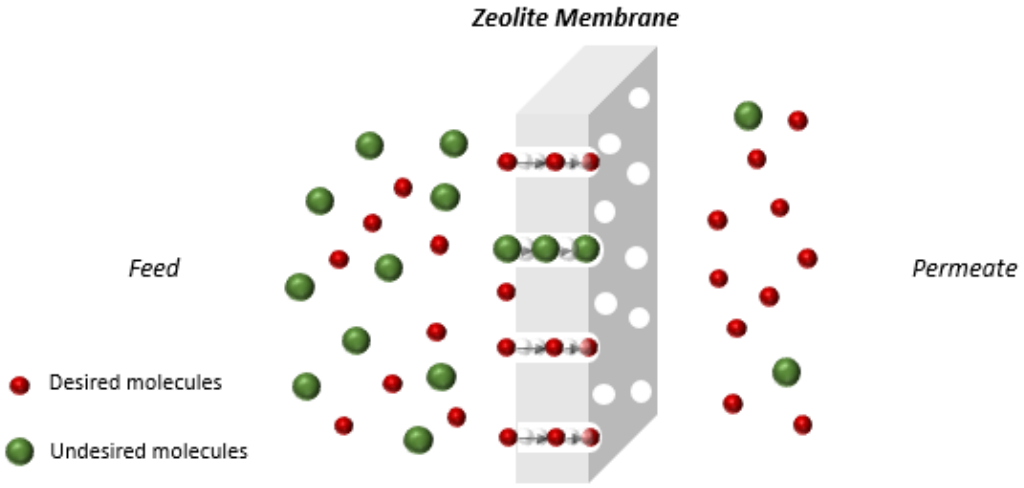

Figure 2.1. Zeolite membrane-based molecular separation.

In this Chapter, we investigate the adsorption and diffusion properties of Kr and Xe in SAPO-34 under various conditions. We hypothesized that SAPO-34 material may have excellent performance in separating Kr and Xe with the assumption that Kr diffusion selectivity outcompetes adsorption selectivity of Xe. We synthesize SAPO-34 material in an appropriate dimension and investigate. Single component adsorption behavior was examined experimentally and the experimental data was fitted to appropriate adsorption model. Mixture adsorption behavior was modeled by ideal adsorption solution theory (IAST) using the pure component Langmuir adsorption parameters. This allows us a comprehensive understanding of adsorption and diffusion of

Kr and Xe in SAPO-34 which will have a strong influence on the separation properties of SAPO-34 membranes.

2.2 Experimental Methods

2.2.1 Materials

Aluminum hydroxide ($Al(OH)_3$, 99 %), phosphoric acid (H_3PO_4, 85 wt% in water), LUDOX-AS40 colloidal silica (40 wt% suspension in water), tetraethylammonium hydroxide (TEAOH, 35 wt% in water), and cyclohexylamine (99 %) were purchased from Sigma-aldrich and used as received.

2.2.2 Synthesis of SAPO-34 crystals

SAPO-34 crystals were synthesized from a reactant molar composition of 1.0 Al_2O_3:1.0 P_2O_5:0.32 SiO_2:1.0 TEAOH:1.6 CHA (cyclohexylamine):52 H_2O. In order to avoid the influence of external and intercrystalline mass transfer resistance during diffusivity measurement, cyclohexylamine was used to as a secondary structure directing agent (SDA) which is known to result in large SAPO-34 crystals by controlling pH of synthesis solution [26]. Aluminum hydroxide, phosphoric acid and water were stirred for 3 h at room temperature to obtain a clear solution followed by adding Si source. The resulting mixture stirred for another 3 h. TEAOH and cyclohexylamine were then added and the synthesis gel solution was aged for 4 days at room temperature for aging step. SAPO-34 crystals were hydrothermally synthesized at 493 K for 24 h in Teflon-lined autoclave reactors (Parr) and washed thoroughly by repeated centrifugation and

dispersion in DI water. The resultant precipitate was then dried at 333 K for 24 h in a drying oven. SAPO-34 powder was calcined at 823 K in stagnant air for 6 h to remove the SDAs with 1 K/min heating and cooling rates.

2.2.3 Structural characterization

X-ray diffraction (XRD) patterns of synthesized crystals were obtained using a PANalytical X'pert diffractometer operating with a Cu-Kα source (λ=1.5418Å) in a scanning range of 5-40^{o} 2θ. The surface of crystals and membranes were observed by scanning electron microscopy (SEM) on a JEOL LEO-1530 at a landing energy of 10 kV using an InLens detector. SAPO-34 powders were dispersed with 0.1 wt % in a filtered ethanol solution by sonication for 10 min and the dispersion was dried as mounted on the sample holder. Crystal size distributions were obtained from statistica analysis of multiple SEM images to obtain sample sizes more than 500 crystals in each case. N_2 adsorption–desorption isotherms and BET surface areas were measured with a Tristar II 3020 (Micromeritics). Samples were degassed for pore activation at 423 K with a duration of 16 h before the measurement.

2.2.4 Single Component Adsorption and Diffusion Measurements

The single-gas adsorption isotherms and transport diffusivities were measured in a pressure decay cell (PDC) built in-house.[22, 58] A known amount of sample was sealed into a 0.5 μm filtered container and the container was installed in the sample chamber. The sample chamber and reservoir chamber is separated by the valve and the system was degassed at 393 K for 12 h under vacuum prior to measurement. Adsorption isotherms were measured at temperatures from 308 K, 323 K and 343 K and the isotherm data were

fitted to the Langmuir model. Transport (Fickian) diffusivities were measured from the PDC data by fitting the kinetic gas uptake curves at low loadings of the gas in the zeolite.

2.2.5 Multicomponent Adsorption Model

Since membrane separation occurs under mixture conditions, we also used the Langmuir-fitted single-component isotherms to predict the binary adsorption behavior *via* ideal adsorbed solution theory (IAST) [50]. The IAST equilibrium relationship for solid-fluid equilibrium is analogous to Raoult's law for vapor-liquid equilibrium. We hypothesized essentially ideal mixing in the adsorbed phase, which is an excellent assumption for noble gas mixtures in non-cationic zeolites. The adsorbed amounts of gas as well as total adsorbed amounts were calculated at different conditions of Kr-Xe mixture composition, total pressure, and temperature. A Matlab code was written to generate these predictions, according to the details of practical application of IAST as described in detail elsewhere.[50, 59] The double Langmuir approximation was also used for comparison to the IAST predictions. The calculation methods and main equations have been previously discussed in Chapter 1.4.2.

2.3 Results and Discussion

2.3.1 Synthesis of SAPO-34 crystals

Figure 2.2a shows XRD pattern of SAPO-34 seed crystals made with cyclohexylamine (CHA) as a secondary SDA. The quantification of crystal size

distributions (**Figure 2.2c**) were obtained using image analysis of a sufficient number of SEM micrographs (**Figure 2.2b**). The average crystal size and standard deviation was 10.7±2.3 μm and calculated by the equation:

$$\bar{R} = \frac{\sum V_i R_i}{\sum V_i} = \sum_i X_i R_i \tag{2.1}$$

where R_i and V_i are the equivalent spherical crystal radius and volume of each individual crystal, X_i is the volume/weight fraction of crystals with a radius of R_i. As will be shown later, the crystal size distributions illustrated in **Figure 2.2** were used to estimate effective diffusivities in SAPO-34. The edge dimension of the cuboid crystals is used as the effective crystal diameter, since this achieves the required equivalence of surface area-to-volume ratio with a spherical crystal of the same diameter.

N_2 physisorption measurements at 77 K on the calcined large crystals showed a micropore volume of 0.22 cm^3/g and BET surface area of 490 m^2/g which are in good agreement with the previously reported value [44], thus confirming that the organic SDAs were sufficiently removed from the pores.

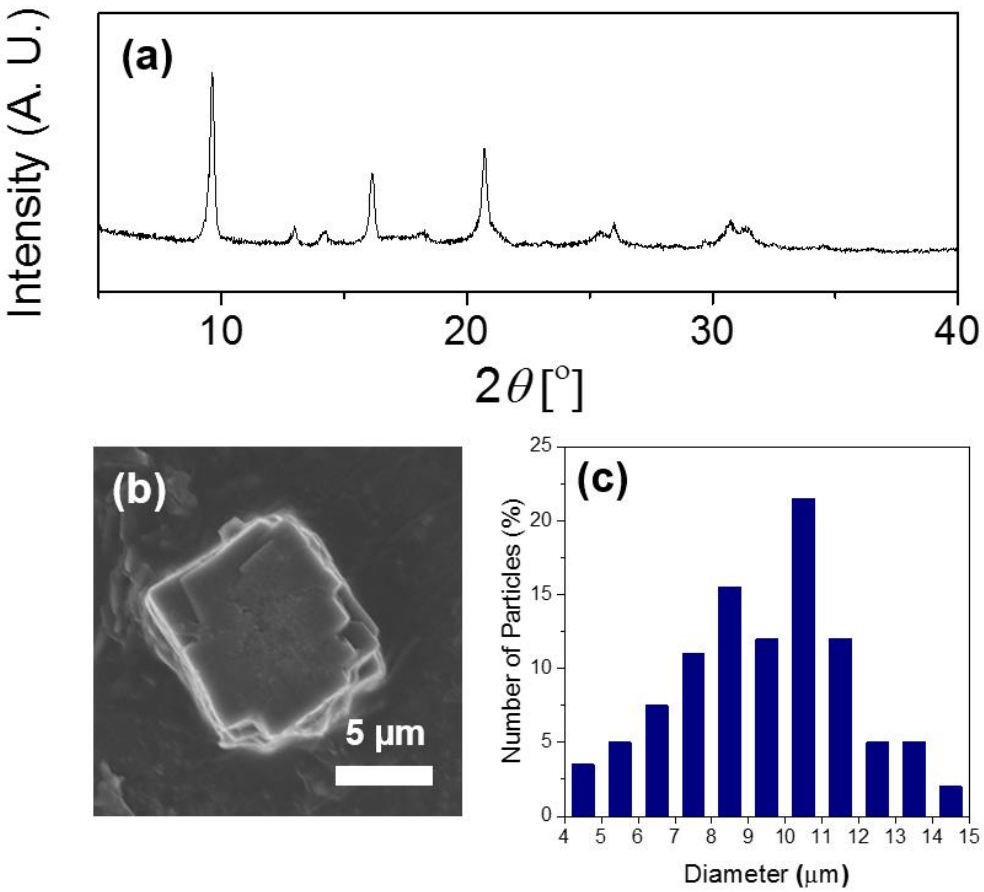

Figure 2.2. (a) XRD patterns of SAPO-34 crystals as a function of 2θ diffraction angle; (b) example SEM images of SAPO-34 crystals showing the characteristic SAPO-34 cuboidal shape; and (c) crystal size distributions of SAPO-34 crystals. The "crystal diameter" is defined as discussed in the results and discussion section.

2.3.2 Single Component Adsorption Behavior

The single component adsorption properties of light gases (e.g. CO_2, CH_4, N_2, and H_2 etc.) have widely been studied [44, 45, 60, 61]. However, limited results have been reported on adsorption of noble gases such as Kr and Xe in SAPO-34. A pressure decay cell (PDC) with a dual-volume adsorption apparatus was used to calculate adsorption uptake of each gas. By measuring the pressures of reservoir chamber (RC) and sample

chamber (SC) at t=0 and at equilibrium, the adsorbed amounts can be calculated at different temperatures and pressures [58].

Single-component adsorption isotherm data were fitted to the Langmuir model:

$$q = \frac{q_{sat}\, b\, p}{1 + b\, p} \tag{2.2}$$

where q is the adsorbate concentration in the sample, q_{sat} the saturation coverage, p the pressure and b the Langmuir constant which can be expressed in terms of the enthalpy of adsorption (ΔH_{ads}) and the pre-exponential entropic factor b_o = exp ($\Delta S_{ads}/R$). These values were obtained by fitting to the b values using isotherms measured at three different temperatures (308 K, 323 K, and 343 K).

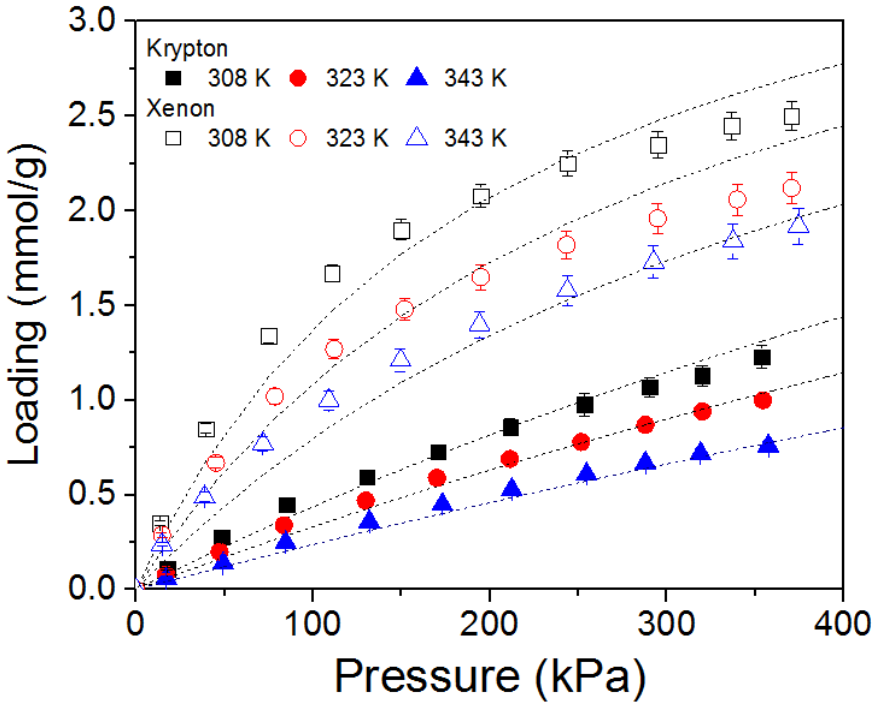

Figure 2.3. Single gas Kr and Xe adsorption isotherms on SAPO-34. Symbols are experimental data and dashed lines are Langmuir model fits

Figure 2.3 shows the experimental single-component Kr and Xe adsorption isotherms collected at three different temperatures over the pressure range 10-400 kPa. SAPO-34 shows preferential adsorption of Xe over Kr (*e.g.*, by a factor of roughly 3 at 100 kPa). The Langmuir adsorption thermodynamic parameters are shown in **Table 2.1**, which were obtained from a global fit of the isotherms over all three temperatures. The heat of adsorption ($-\Delta H_{ads}$) can be calculated using Arrhenius plot of b at different temperatures ($b = b_0 e^{-\Delta H_{ads}/RT}$), which indicates the strength of the interaction between an adsorbent and adsorbate. The heat of adsorption of Xe (18.3 kJ/mol) in SAPO-34 is higher than that of Kr (16.1 kJ/mol), thus leading to stronger adsorption of Xe. Overall the Langmuir model provides an excellent fit of the adsorption isotherms.

Table 2.1. Langmuir adsorption parameters for Kr and Xe in SAPO-34 as obtained from experimental adsorption isotherms.

Gas	q_{sat} (mmol/g)	$-\Delta H_{ads}$ (kJ/mol)	b_0 ($\times 10^{-6}$ kPa^{-1})
Kr	6.1 ± 0.2	16.1 ± 0.3	1.4 ± 0.3
Xe	4.2 ± 0.1	18.3 ± 0.4	3.8 ± 0.2

2.3.3 Modeling for Binary Component Adsorption

Since the Langmuir model provided an excellent fit of the adsorption isotherms in previous chapter, and we used it directly in the IAST calculations. IAST is an analog of Raoult's law applied to adsorbed mixtures which enables the prediction of mixture adsorption isotherms from single component adsorption data. It is extensively used for

the prediction of multicomponent adsorption behavior and does not account for the intermolecular interactions between the adsorbates. However, if there exist non-idealities in the mixture coming from energetic or surface heterogeneity, or a non-ideal mixture, extended version of IAST must be used, so-called real adsorption solution theory (RAST). Therefore, IAST provides a good estimation for noble gases such as Kr and Xe which are assumed to not interact each other.

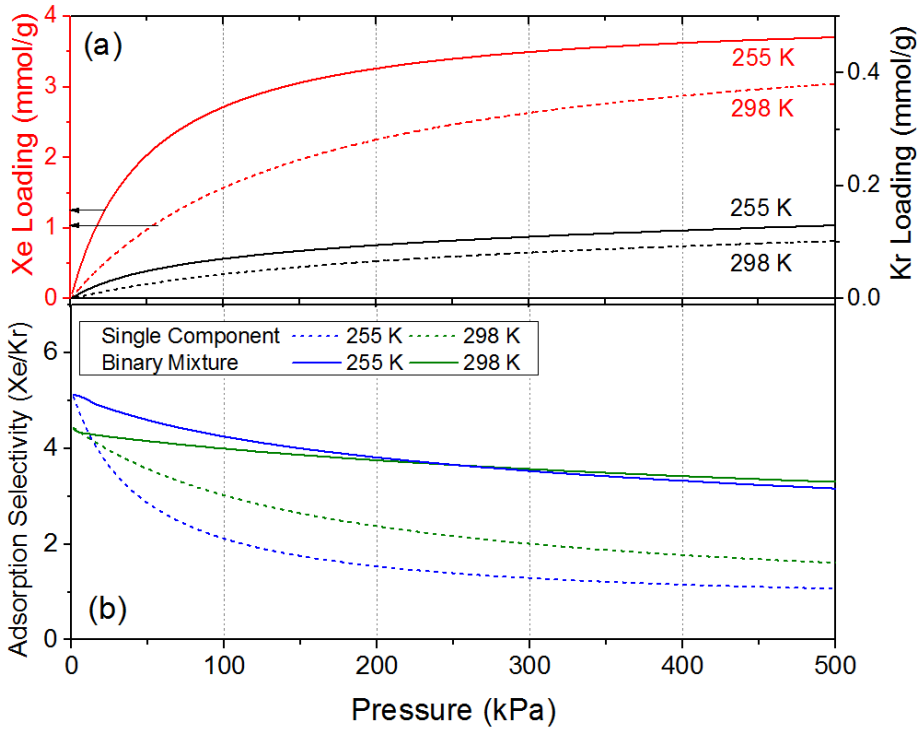

Figure 2.4. IAST predictions of (a) Xe and Kr adsorption on SAPO-34 from a 10/90 Kr/Xe binary feed mixture; and (b) the corresponding Xe/Kr adsorption selectivity; at two temperatures of 255 K and 298 K.

Figure 2.4(a) shows the IAST predictions of binary adsorption from a 10/90 Kr/Xe feed gas mixture at two temperatures (298 K and a sub-ambient temperature of 254 K) for pressures up to 500 kPa. Selectivity can be defined as the ratio of mole

fraction of Xe in the adsorbed state (y_{Xe}) over the mole fraction of Xe in the gas phase (x_{Xe}) divided by the same correlation of Kr ($y_{Kr}$and x_{Xe}).

$$S_{Xe/Kr} = \frac{y_{Xe}/x_{Xe}}{y_{Kr}/x_{Kr}} \tag{2.3}$$

The IAST-predicted binary adsorption selectivity for Xe is significantly higher (e.g., ~4 at 298 K and 100 kPa) than that predicted by a simple weighting of the single-component isotherms (~3). The preferential adsorption of Xe over Kr can be explained by the higher Van der Waals force of Xe compared to Kr, which have been observed in chabazite zeolite crystals.

Thus in a binary mixture, Xe is preferentially adsorbed and blocks the adsorption site of Kr in the binary mixture. Xe adsorption selectivity decreases as we pressurize, but the change is pretty moderate at the pressure higher than 100 kPa. Therefore, in order to allow the expected Kr diffusion selectivity to counteract the Xe adsorption selectivity, the membrane is good to be operated at atmospheric conditions. The IAST predictions were then used for comparison with the single site Langmuir model.

$$q_i = \frac{q_{i,sat} b_i p_i}{1 + \sum_{j=1}^{2} b_j p_j} \tag{2.4}$$

The parameters used in the double Langmuir model are, by definition, the same as those already obtained from the single-component Langmuir isotherms (**Table 2.1**). This comparison is useful because the double Langmuir model (unlike the IAST) is very convenient for use in Maxwell-Stefan modeling of membrane transport owing to its simple mathematical form as well as the ease of deriving analytical expressions for the

thermodynamic correction factors. As shown in **Figure 2.5**, the double Langmuir isotherm matches very well with the IAST predictions for Xe over the entire pressure range and for Kr at atmospheric or lower pressures (< 100 kPa). Since the present study focuses on Kr-Xe separation from a feed at atmospheric pressure conditions, **Figure 2.5** indicates that the double Langmuir model is acceptable for use in Maxwell-Stefan modeling of transport in the SAPO-34 membrane.

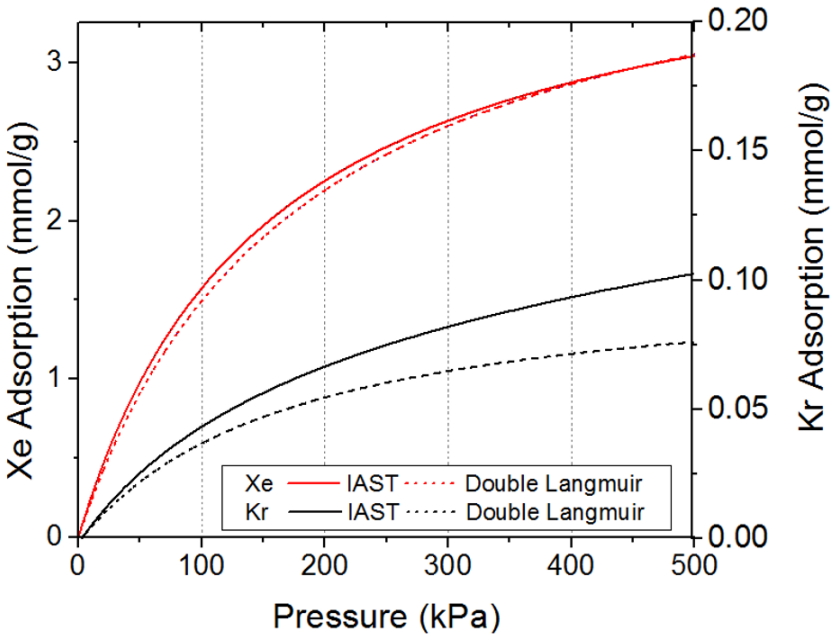

Figure 2.5. Comparison between double Langmuir approximation and IAST predictions for 10 % Kr/ 90 % Xe mixture adsorption in SAPO-34 at 298 K.

2.3.4 Diffusion Behavior of Kr and Xe in SAPO-34

Transport (Fickian) diffusivities were measured from the PDC data by fitting the kinetic gas uptake curves at low loadings of the gas in the zeolite. However, Fickian diffusivities cannot explain the intrinsic hopping rate of individual molecules. In order to elucidate the thermodynamically corrected diffusion through the pore windows of

material, the Maxwell-Stefan diffusivity should be considered. Therefore, SAPO-34 crystals with appropriate dimension (~ 10 μm) were used to minimize any intercrystalline diffusion resistance and to calculate the diffusivities of Kr and Xe across the zeolite pores.

The model used has been described in detail in previous literature [22, 62]. Generally, the effective intracrystalline transport diffusivity can be calculated by fitting the experimental kinetic uptake curve (M_t/M_∞) in terms of time ($t^{1/2}$), where M_t represents moles adsorbed by sample at time t and M_∞ adsorbed moles at infinity time (mmol). In the short time region, the kinetic uptake curve is essentially linear and approximated by the equation below.

$$\frac{M_t}{M_\infty} = 1 - \frac{6}{\pi}\sum_{n=1}^{\infty}\frac{1}{n^2}\exp\left(-\frac{n^2\pi^2 Dt}{R^2}\right) \approx \frac{6}{\sqrt{\pi}}\sqrt{\frac{Dt}{R^2}} \tag{2.5}$$

However, this equation assumes that the crystals have uniform sizes, which is not reliable for crystals with wide size distribution [49]. Therefore, a modified diffusivity model is used in this study considering the crystal size distributions as well as the time-dependent pressure boundary condition [63]. The equation is then be rewritten by considering the crystal size distributions:

$$\frac{M_t}{M_\infty} = 1 - \frac{6}{\pi}\sum_{i}\sum_{n=1}^{\infty}X_i\frac{1}{n^2}\exp\left(-\frac{n^2\pi^2 Dt}{R^2}\right) \approx \frac{6}{\sqrt{\pi}}\sum_{i}X_i\sqrt{\frac{Dt}{R^2}} \tag{2.6}$$

Eqn. 2.6 can then be simplified as:

$$\frac{M_t}{M_\infty} \approx \sum_i X_i(1+\alpha)\left[1 - \frac{\gamma_1}{\gamma_1+\gamma_2} eerfc\left\{\frac{3\gamma_1}{\alpha}\left(\frac{Dt}{R_i^2}\right)^{\frac{1}{2}}\right\} - \frac{\gamma_2}{\gamma_1+\gamma_2} eerfc\left\{\frac{3\gamma_2}{\alpha}\left(\frac{Dt}{R_i^2}\right)^{\frac{1}{2}}\right\}\right] \quad (2.7)$$

$$\alpha = \frac{1}{\Lambda} - 1$$

$$\gamma_1 = \frac{1}{2}\left\{\left(1 + \frac{4}{3}\alpha\right)^{1/2} + 1\right\}$$

$$\gamma_2 = \gamma_1 - 1$$

$$eerfc(z) = \exp(z^2) \times erfc(z)$$

where Λ is the adsorbed loading fraction at time t and X_i is the mass fraction of the crystals with the radius R_i as obtained from the crystal size distribution. From this equation, the transport diffusivities were calculated by taking into account the crystal size distribution and pressure changes with uptake time. The thermodynamically corrected Maxwell-Stefan (M-S) diffusivity, which can be taken as representing the intrinsic rate of diffusive hopping of molecules in the zeolite pores, is then obtained from the Fickian diffusivity.

$$D = D_{MS}\frac{d\ln p}{d\ln q(p)} = D_{MS}\Gamma \quad (2.8)$$

$$D_{MS} = D_{MS}^{o} e^{-\frac{Ea}{RT}} \quad (2.9)$$

where D is transport diffusivity obtained from fitting Eqn. (2.7) to the experimental data, D_{MS} is the M-S diffusivity and Γ is thermodynamic correction factor obtained from the

adsorption isotherm. **Figure 2.6** shows an example of fitting Eqn. (2.7) to the uptake data.

Table 2.2. Maxwell-Stefan diffusion parameters for Kr and Xe in SAPO-34 as obtained from experimental adsorption isotherms and kinetic uptake data.

Gas	D^0_{MS} ($\times 10^{-10}$ m^2/s)	E_a (kJ/mol)
Kr	2.5 ± 0.3	13.9 ± 1.0
Xe	2.0 ± 0.05	23.6 ± 0.8

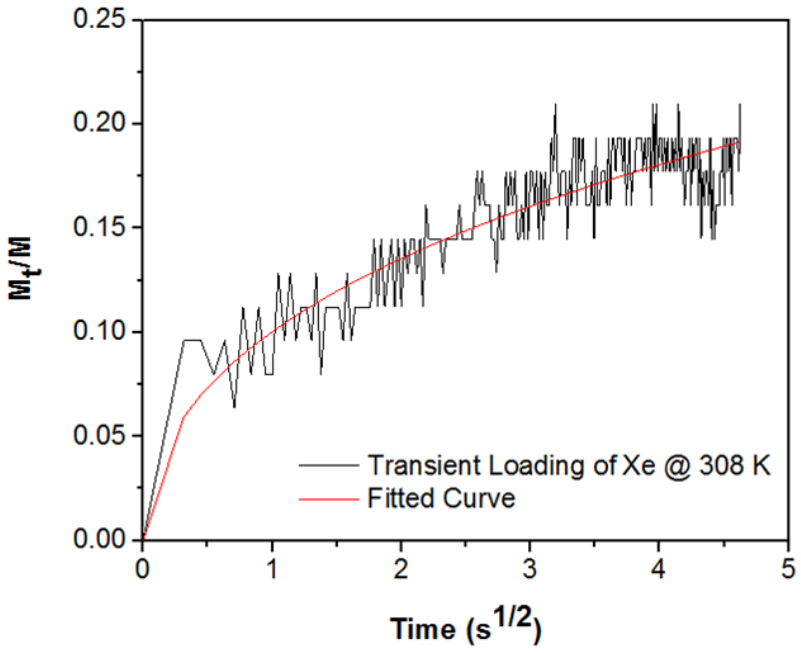

Figure 2.6. Example of transient uptake curve and fitting. Transient adsorption loading of Xenon and fitted curve at 308 K. Transport diffusivity was estimated as 2.0×10^{-14} m^2/s.

Based on the kinetic uptake data and transport diffusivities calculated from **Figure 2.6**, Maxwell-Stefan diffusivities were calculated at different temperatures and the results are shown in **Figure 2.7**. The thermodynamic correction factors (Γ) were estimated using the Langmuir isotherm curves and then diffusivity parameters including D0MS and activated energy of diffusion (E_a) **Table 2.2** shows the M-S diffusion parameters obtained from the kinetic uptake data (**Figure 2.6**). While the D^0_{MS} values for Kr and Xe are similar in magnitude, the diffusion activation energy of Kr is much lower than that of Xe. This is consistent with the kinetic diameters of Kr (0.36 nm) and Xe (0.396 nm) in relation to the crystallographic pore size of SAPO-34 (0.38 nm).[44, 45]

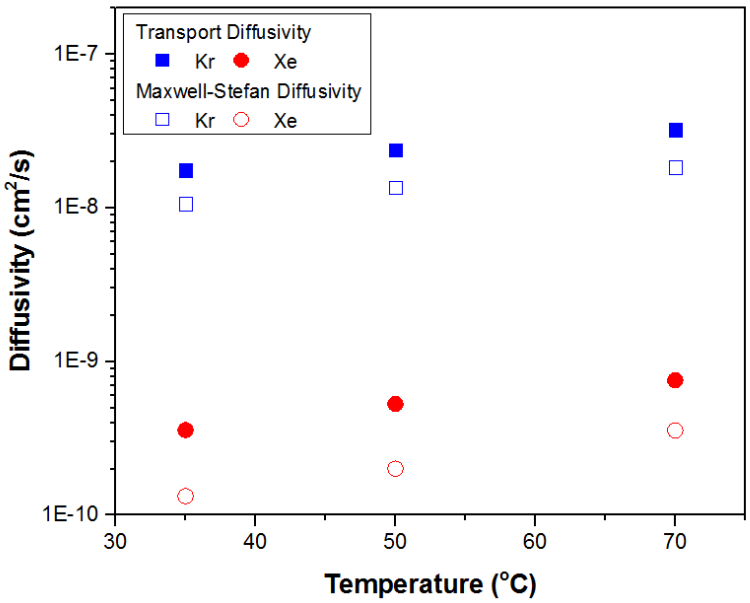

Figure 2.7. Transport diffusivity and Maxwell-Stefan diffusivity calculated at three different temperatures

2.4 Conclusion

In this Chapter, we have studied in detail the adsorption and diffusion behavior of Kr and Xe in SAPO-34 material and shown their potential for membrane-based Kr/Xe separation. Firstly, SAPO-34 crystals with large dimensions (~ 10 μm) were synthesized using cyclohexylamine as a secondary SDA. The use of cyclohexylamine led to control the pH of synthesis solution and the size of SAPO-34 crystals was large enough to minimize the intercrystalline mass transfer resistance. SAPO-34 crystals with appropriate dimension were then evaluated as a potential candidate for Kr/Xe separation process. Adsorption and diffusion behavior of Kr and Xe in SAPO-34 have been investigated experimentally using gravimetric uptake curves and the experimental data at equilibrium was fitted to the single-site Langmuir model. It was found that Xe showed stronger adsorption than Kr in both single-component adsorption experiments and binary adsorption predictions. However, due to its smaller molecular size, Kr showed much faster diffusion than Xe with a considerably lower activation energy of diffusion. The overall membrane performance under mixture permeation conditions can be determined by the adsorption and diffusion behavior of mixture in SAPO-34 materials. Although competitive adsorption and diffusion constitute the overall separation mechanism, the present results suggest that the diffusivity differences and molecular sieving (rather than adsorption) would be the dominant mechanism in SAPO-34 membranes.

CHAPTER 3. SYNTHESIS OF SAPO-34 MEMBRANES AND PERMEATION PROPERTIES OF KRYPTON AND XENON[2]

3.1 Introduction

Since our investigation of adsorption and diffusion behavior of Kr and Xe in SAPO-34 (Chapter 2) showed promising separation properties, in this Chapter I investigate the fabrication of SAPO-34 membranes and measurement of their permeation properties. One of the main issues in zeolite membrane synthesis is the control of defects such as pinholes or non-zeolitic pores. In order to synthesize defect-free zeolite membranes by the "secondary growth" technique, it is required to make high-quality seed layers on the substrate surface from which a well-intergrown polycrystalline membrane can be grown. However, it is difficult to form a compact seed layer on low-quality macroporous substrate by conventional dip-coating seeding or rub-coating seeding method. Our initial trials involved mechanical seeding (rubbing) of crystal powders on the support [64] or dip-coating from a colloidal suspension [40], but the selectivity of Kr/Xe was merely 5 after the secondary growth and SF_6 (0.55 nm) permeance was about 1 GPU, which means the existence of non-zeolitic pores. Therefore, I demonstrate steam-assisted conversion (SAC) seeding method to selective zeolite membranes on low-cost macroporous ceramic substrate. The SAC technique was first introduced by Zhou et al [65], and involves the transformation of a reactant paste/gel containing zeolite seed

[2] Reprinted with permission from Y. H. Kwon, C. Kiang, E. Benjamin, P. Crawford, S. Nair, R. Bhave, "Krypton-xenon separation properties of SAPO-34 zeolite materials and membranes", AIChE Journal, 63, pp. 761-769. Copyright 2017 John Wiley & Sons.

crystals into a compact seed layer with the aid of steam. I hypothesized that the SAC technique provides a promising starting point for the fabrication of high-performance SAPO-34 membranes.

In this Chapter, a detailed investigation of the SAC-based method is conducted for preparation of SAPO-34 membranes to achieve high Kr/Xe selectivities. In addition, the single-component permeation properties of various gases are investigated in SAPO-34 membranes to assess the molecular sieving properties. The contribution of defects in the SAPO-34 membrane is assessed using the time-lag method and permeance measurements of large gas molecules that cannot permeate through the zeolite pores. I further present detailed binary Kr-Xe gas mixture permeation measurements at different temperatures. Finally, the impact of radiation exposure is investigated on SAPO-34 membrane performance.

3.2 Experimental Methods

3.2.1 Synthesis of SAPO-34 seed crystals

SAPO-34 crystals with the size of ~ 500 nm were prepared from a mixture with molar composition of 1.0 Al_2O_3:1.0 P_2O_5:0.32 SiO_2:1.0 TEAOH:1.6 DPA (diropylamine):52 H_2O. The Al source was alumina isopropoxide ($Al(i\text{-}Pr)_3$), the P source was phosphoric acid (H_3PO_4, 85 wt% in water) and the Si source was LUDOX AS-40 colloidal silica (40 wt% suspension in water). The structure directing agents (SDAs) were tetraethylammonium hydroxide (TEAOH, 35 wt% in water) and

dipropylamine (DPA, 99% pure). All chemicals were purchased from Sigma-Aldrich and used as received. In a typical synthesis method, the Al source, P source and water were stirred for 3 h to obtain a clear solution and then the Si source was added and the mixture stirred for another 3 h. The SDAs were then added and the synthesis gel solution was aged for 4 d at room temperature. Both types of SAPO-34 crystals were hydrothermally synthesized at 493 K for 6 h in Teflon-lined autoclave reactors (Parr) and calcined at 823 K in stagnant air for 6 h to remove the SDAs.

3.2.2 Synthesis of SAPO-34 membranes

Disk-type α-alumina supports (25.4 mm diameter and 1 mm thickness, Coorstek) and tube-type α-alumina supports (11 mm OD, 8 mm ID, 30 mm length, Ceramco) were cleaned by sonication in acetone for 10 min and dried in an oven at 100°C for 24 h before use. The substrates were seeded using the smaller-size SAPO-34 crystals *via* the steam-assisted conversion (SAC) method reported by Zhou et al.[65] The seed crystals were added to a synthesis mixture that had a molar composition of 1.0 Al_2O_3:2.0 P_2O_5:0.6 SiO_2:4.0 TEAOH:75 H_2O. , and the Al source was alumina isopropoxide and LUDOX AS-40 was used as Si source. The seeds/synthesis mixture ratio was 15 mg/g. After evaporating 90 % water from the mixture at 353 K and converting the synthesis mixture into a gel-like paste, the disk support was hand-coated with the paste containing the seeds. For the tubular substrate, the inner surface was coated with the paste. The substrates were then dried for 2 h at 323 K and subsequently placed in Parr autoclaves with 5 mL of DI water introduced at the bottom. The SAC process was then carried out at 473 K for 24 h in order to convert the paste coating into continuous seed layer.

Well-intergrown SAPO-34 membranes were then prepared from the post-SAC substrates by contacting them with a synthesis mixture of molar composition 0.85 Al_2O_3:1.0 P_2O_5:0.3 SiO_2:1.75 TEAOH:155 H_2O. $Al(OH)_3$ (Al source) and DI water were mixed and stirred for 30 min, followed by phosphrous source addition and stirring for 2 h. The Si source (colloidal silica) was added to the mixture and stirred for additional 30 min. Then TEAOH was added and the mixture was aged for 12 h at 328 K. The seeded substrate was placed vertically in a Parr autoclave and hydrothermal growth was carried out at 493 K for 6 h. The outer surfaces of the tubes were tightly wrapped in Teflon tape before immersion in the synthesis mixture, so that the membrane growth can occur only at the inner surfaces. After the secondary growth, the membranes were washed thoroughly and dried overnight. The membranes were then calcined at 873 K for 6 h in stagnant air using a slow 0.5 K/min heating and cooling rate to avoid potential cracks caused by rapid temperature changes. For comparison, disk membranes seeded by the conventional rubbing method[64] and tubular membranes seeded by dip and rub coating (from a colloidal solution of small SAPO-34 crystals)[40] were also prepared. First, the polished disk or tubular substrate are dipped into a seed dispersion (1 wt% in DI water) for 10 s. In order to avoid any seed crystal deposition on the outer surface of tubular substrate, tubular substrates are tightly wrapped with Teflon tape. The seeded substrates are then dried for 1 h in the drying oven. The dried seed layer is forcefully rubbed with finger or cotton swab for a tight coverage of seed layer. This procedure is repeated two more times, and rubbing procedure is not followed for the last time.

3.2.3 Permeation Measurements

Single-component permeation measurements were carried out on disk and tube-type SAPO-34 membranes using in-house built permeation units operating in dead-end mode (**Figure 3.1**).

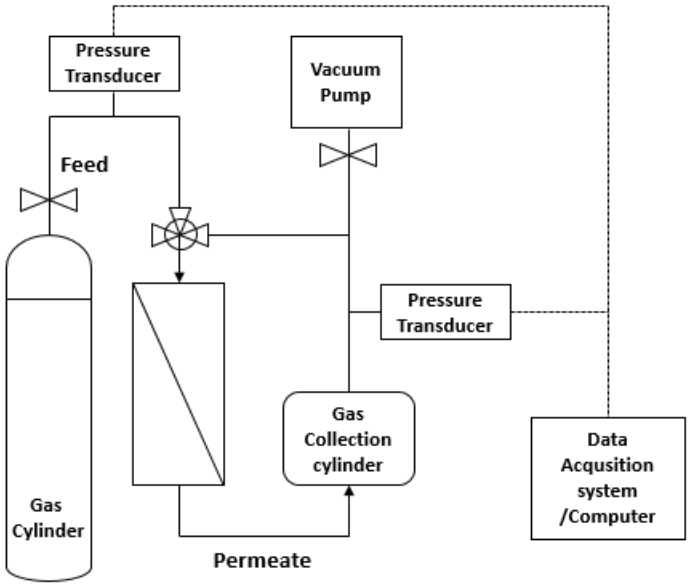

Figure 3.1 Schematic diagram of dead-end mode single gas permeation unit.

Various gases were measured at ambient temperature (295 K), but Kr and Xe permeation measurements were additionally conducted at temperatures ranging from 254 K to 343 K. For sub-ambient operation, the membrane module was submerged in a salt water-ice cooling bath at 254 K. Prior to measurement, the membranes were degassed *in situ* under vacuum at 373-473 K for 1-4 h prior to measurement. The feed pressure was maintained at 110 kPa and the permeate side was at vacuum. The fluxes were obtained by the standard method of measuring the rate of the initial linear pressure rise in a collection vessel on the permeate side after isolating the vacuum. The permeance is then obtained as

the ratio of the measured flux and the pressure drop between the feed and permeate side. Finally, the ideal selectivity (permselectivity) of Kr over Xe is the ratio of their respective permeances.

Binary mixture permeation was measured in a Wicke-Kallenbach mode at a system pressure of 1 atm (**Figure 3.2.**). The feed was 10 mol% Kr/90 mol% Xe mixture, generated by two mass flow controllers. The total flow rate of feed was 30 mL/min. A helium sweep (20 mL/min) was used to collect the permeate, whose composition was then analyzed by a gas chromatograph (Shimadzu GC-TCD-2014) equipped with a HP-PLOT 5A column (Agilent) and a TCD. The permeance of each component is obtained as its flux normalized by its transmembrane partial pressure. The Kr/Xe selectivity of the membrane is given as the ratio of permeances of each gas.

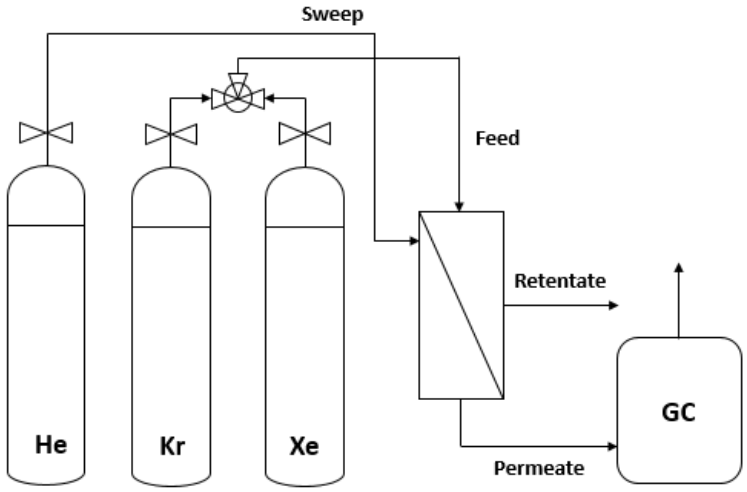

Figure 3.2. Schematic diagram of cross-flow mode binary gas permeation unit.

3.3 Results and Discussion

3.3.1 SAPO-34 seed crystal characterization

In order to improve the attachment of seed crystals on the alumina substrate, small size of SAPO-34 crystals were synthesized using dipropylamine as a secondary structure directing agent (SDA). **Figure 3.3a** shows XRD pattern of the small crystals (labeled SAPO-34-DPA) made with dipropylamine (DPA) SDA. Image analysis of a number of SEM micrographs (*e.g.*, **Figures 3.3b**) allows the quantification of crystal size distributions (**Figures 3.3c**). The average crystal size and standard deviation is 0.5±0.1 µm (SAPO-34-DPA).

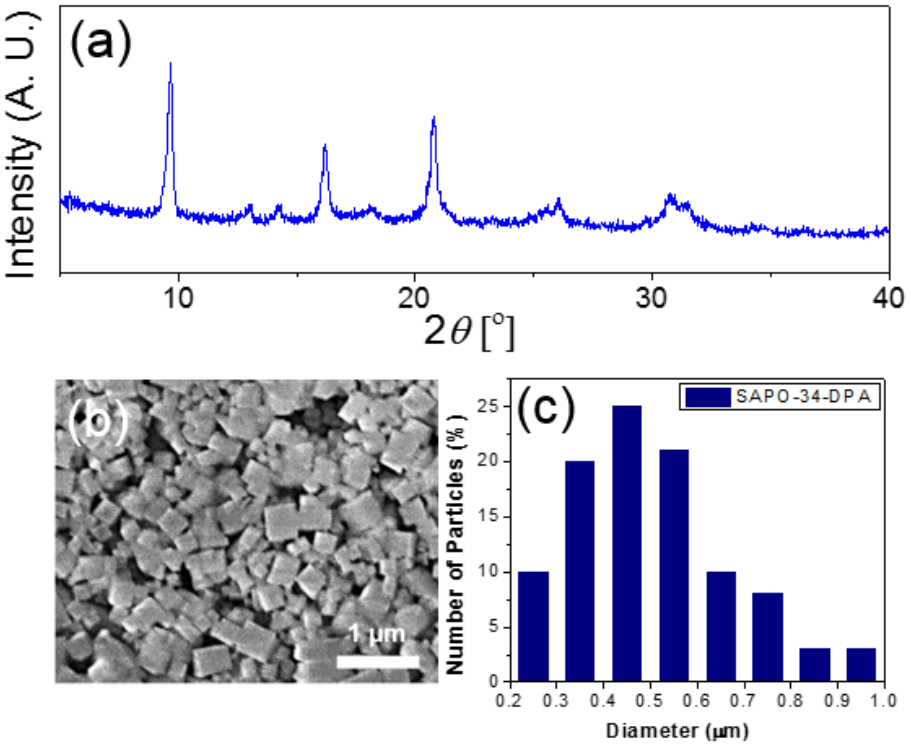

Figure 3.3. (a) XRD patterns of SAPO-34 seed crystals as a function of 2θ diffraction angle; (b) example SEM images of SAPO-34 crystals showing the characteristic SAPO-34 cuboidal shape; and (c) crystal size distributions of SAPO-34 crystals.

3.3.2 SAPO-34 Membrane Synthesis Technique

In order to synthesize defect-free molecular sieve membranes with desired properties, it is important to coat a continuous layer of seed which would be used for subsequent crystal growth. Therefore, various seeding methods including rub-coating[39], dip-coating[26, 40, 44], and vacuum seeding[66] have been reported for zeolite membrane fabrication. For our first trial, I used dip and rub coating method to get a seed layer on the surface of substrate (**Figure 3.4**). However, it was difficult to obtain a continuous seed layer due to the nature of macroporous alumina substrates, which have large alumina chunks and micrometer sized pores resulting in bad affinity with SAPO-34 crystals. Therefore, for SAPO-34 membranes seeded by dip and rub coating method, the resulting membrane showed the ideal selectivity of merely 2 -5 for Kr/Xe and considerably high SF_6 permeance (~2 GPU), which means this membrane is defective (**Table 3.1**).

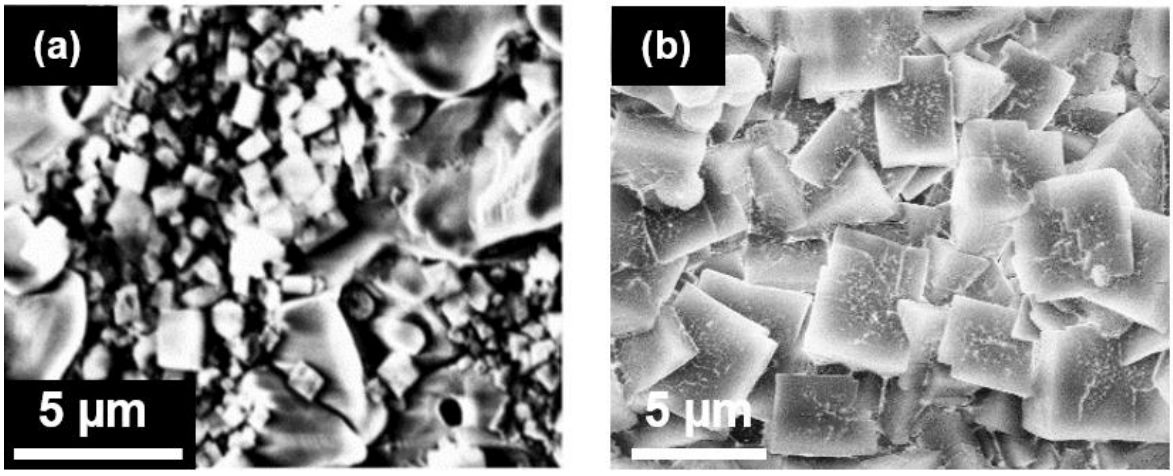

Figure 3.4. SEM images of (a) dip-coated alumina substrate and (b) Membrane surface after secondary growth

Zhou et al. reported that SAPO-34 membranes seeded by steam-assisted conversion (SAC) showed a smooth and continuous morphology with high H_2 permeance of 6.96×10^{-8} $mol.m^{-2}.s^{-1}.Pa^{-1}$ (or 208 GPU, where 1 Gas Permeation Unit = 3.348×10^{-10} $mol.m^{-2}.s^{-1}.Pa^{-1}$) and a good H_2/CH_4 single-gas selectivity of 15.[65] Based upon this initial report, I employed SAC as a seeding method for the fabrication of SAPO-34 membranes discussed in this report. **Figure 3.5** shows SEM images of the α-Al_2O_3 disk substrate (**Figures 3.5a-3.5b**) and the SAPO-34 membrane after SAC seeding (**Figures 3.5c-3.5d**) and final hydrothermal growth (**Figures 3.5e-3.5f**). The SAC method is seen to provide a continuous and dense "seed" covering, and is particularly useful for coating low-cost α-Al_2O_3 supports such as those used here. Such supports typically display large (~1 μm) particles of alumina sintered together with pores in between (rather than a more uniformly porous surface obtained from packing of smaller alumina particles), which makes it difficult to obtain good seed coverage using conventional dip-coating or rub-coating seed methods. The seed layer does not grow beyond a few hundreds of nm, since there is only a limited supply of reactants available in the initial gel paste coated on the substrate. Finally, continuous membranes were synthesized containing interlocked cuboidal crystals of 1-3 μm size. The final membrane thickness was determined as 4.9±0.2 μm based upon the average of SEM-measured thicknesses at different cross-sectional locations.

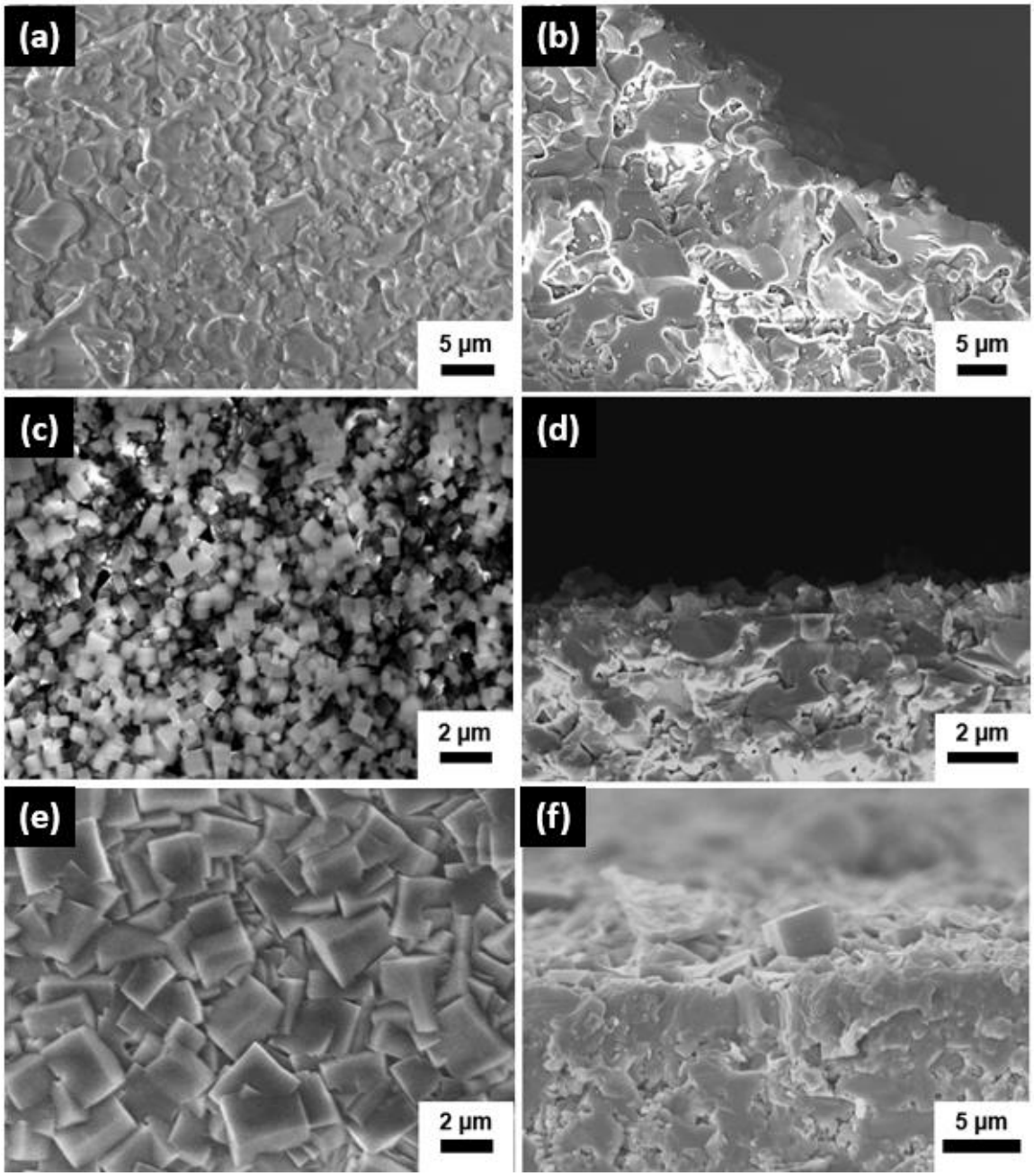

Figure 3.5. Top view and cross-section SEM images of (a-b) α-alumina disk support, (c-d) SAC seed layer, (e-f) final SAPO-34 membrane

Even though the SAPO-34 membrane is successfully synthesized on the disk type substrate, it is necessary to transfer the synthesis method to the substrates with different

geometry (e.g. tube or hollow fiber) for their use in the industry. Therefore, SAPO-34 membrane was synthesized on the macroporous alumina substrate *via* the same synthesis protocol .The SAC and hydrothermal growth was then successfully transferred to tubular supports, and the resulting membranes are shown in **Figures 3.6a-3.6b**. The tubular membrane thickness was determined as 4.1±0.1 μm.

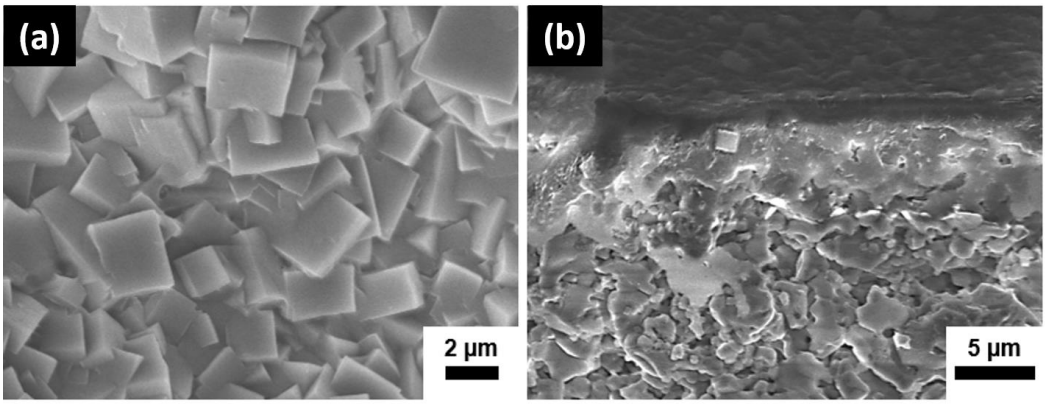

Figure 3.6. Top view and cross-section SEM images of final SAPO-34 membrane synthesized by the same technique on tubular α-alumina support.

3.3.3 Single-component permeation

Table 3.1 compares the single-gas permeances of Kr, Xe, and SF_6 (kinetic diameter 0.55 nm) in the bare alumina supports and the SAPO-34 membranes synthesized after dip-coat seeding and SAC seeding. SF_6 is included as a sensitive probe of membrane quality since it is much larger than the pore size of SAPO-34. As expected, the bare alumina supports have permeances that are orders of magnitude higher than those of the molecular sieving membranes. Compared to the conventional dip-coat seeding method, the membranes synthesized by steam-assisted seeding method shows 4-8 times higher selectivity for Kr over Xe because of the reduction in defects resulting from the high quality seed layer. The significant level of SF_6 permeance reveals the presence

of nanoscale defects in the membranes synthesized with conventional dip-coating. The SF_6 permeance drops by more than an order of magnitude when using the SAC method.

Table 3.1. Effect of membrane seeding method on single-gas Kr and Xe permeances at 295 K.

	Permeance			**Single-gas Selectivity**
Sample	Kr	Xe	SF_6	Kr/Xe
	(10^{-10} mol/m^2·s·Pa)			
Bare disk support	7130	6220	-	1.1
Bare tube support	6860	5730	-	1.2
SAPO-34 disk (rub coat seeded)	38.8	8.1	3.8	4.8
SAPO-34 disk (SAC seeded)	26.2	1.5	0.1	13.8
SAPO-34 tube (dip coat seeded)	31.5	7.7	4.2	4.09
SAPO-34 tube (SAC seeded)	37.4	2.1	0.1	17.8

Figure 3.7 shows the single-gas permeances through the SAC-seeded SAPO-34 disk and tube membranes at 295 K as a function of molecular kinetic diameter. The trends in permeance are the same in disk and tubular membranes, showing a successful transfer of the membrane synthesis from disk to tubular supports. Even though H_2 has the smallest kinetic diameter, CO_2 shows the highest permeance due to its strong adsorption in SAPO-34.[44]

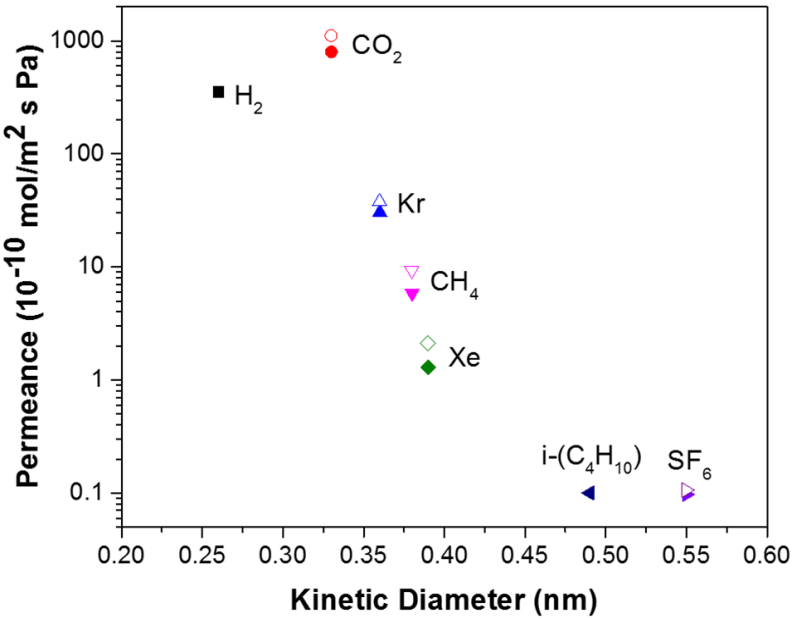

Figure 3.7. Single-gas permeances of different gases at 295 K in SAPO-34 disk and tubular membranes at a feed pressure of 100 kPa. Closed symbols: disk membrane, open symbols: tubular membrane.

I can also compare these permeances to other reported literature data. For example, the permeability of CO_2 through the disk membrane is 4.0×10^{-13} mol.m.m^{-2}.s^{-1}.Pa^{-1} (1200 Barrer), which is comparable to the range of reported literature values of 2.0-9.2 $\times10^{-13}$ mol.m.m^{-2}.s^{-1}.Pa^{-1} (600 - 2700 Barrer)[40, 60, 67]. Similarly, the H_2 permeability of the disk membrane was 1.8×10^{-13} mol.m.m^{-2}.s^{-1}.Pa^{-1} (520 Barrer) which is in the range of reported values (300-600 Barrer) [60]. The CO_2 permeances as well as ideal selectivities of different gas pairs at 295 K are listed in **Table 3.2**. The CO_2 permeances and ideal selectivities of H_2/CH_4, CO_2/CH_4, and Kr/Xe are all high, confirming the high quality of the membranes. Furthermore, these data compare well to the data available in the reported literature.

Table 3.2. Comparison of ideal selectivities of different gases at ambient temperature and feed pressure of 100 kPa. NR = not reported.

	CO_2 permeance (10^{-7} mol.m^{-2}.s^{-1}.Pa^{-1})	**Single-gas Permselectivity**			
		CO_2/ CH_4	H_2/ CH_4	H_2/ CO_2	H_2/ i-C_4H_{10}
This work (disk/tube)	0.8/1.1	116/121	60.6/NR	0.4/NR	2650/NR
Ref [40]	1.3	106	NR	NR	NR
Ref [60]	0.4	NR	NR	0.5	NR
Ref [67]	2.3	150	NR	NR	NR

Figure 3.8 shows the temperature dependence of single-gas permeation of Kr and Xe through a tubular SAPO-34 membrane. At ambient temperature (298 K), the ideal selectivity of Kr/Xe was ~17 with Kr permeance of 11 GPU. The permeance of Kr decreases with increasing temperature, whereas the Xe permeance increases. This temperature dependence results in the highest Kr/Xe ideal selectivity of 23 at the slightly sub-ambient temperature (254 K) and the lowest selectivity of 12 was obtained at 343 K. This behavior can be explained by different limiting factor of each gas on the transport through the membrane. Kr transport is controlled by weak adsorption (since diffusion of Kr is already fast), which decreases as the temperature increases. On the other hand, Xe transport is controlled by activated diffusion (since it has a high activation energy). The single component permeation measurement showed that SAPO-34 membrane is a promising candidate for Kr/Xe separation since favorable Kr diffusion selectivity outcompetes the stronger adsorption of Xe.

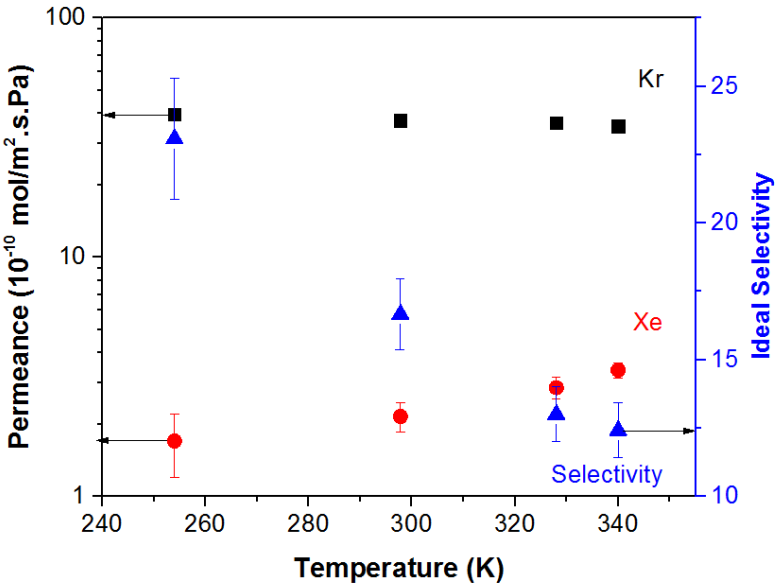

Figure 3.8. Temperature dependence of Kr and Xe single-gas permeances and ideal Kr/Xe selectivity for tubular SAPO-34 membranes.

3.3.4 Kr/Xe mixture Separation

Since the real composition of Kr and Xe mixture is 10/90 of Kr/Xe by volume in the off-gas, the separation of a binary mixture was investigated using tubular SAPO-34 membranes. **Figure 3.9** shows the temperature dependence of Kr/Xe binary mixture permeation. Similar to the single gas permeation behavior, the binary Kr permeance decreases but Xe permeance increases with increasing temperature, which reduces the separation selectivity of Kr/Xe at higher temperatures. Even though the membrane suffers from the competitive effect of Xe-favoring adsorption and Kr-favoring diffusion, it showed a clear molecular sieving effect especially at ambient or at sub-ambient temperatures. Kr permeance at 255K was about 10 GPU with the separation selectivity of 25, which is similar to the value from the single component permeation results. In spite of favorable adsorption selectivity of Xe at lower temperature within the range of 0 – 100

kPa (**Figure 2.4b**), the permselectivity of Kr/Xe was higher at lower temperature due to the stiffness of framework leading to slow down the movement of Xe. This result is clearly promising for the application of SAPO-34 membranes in Kr/Xe separation because it is contrary to our initial speculation that Kr permeance would be severely slowed down by Xe in the binary mixture. From experimental investigation, the operation of the membrane at slight sub-ambient condition may be favorable since the permeance of Kr remains high and the selectivity dramatically increases with decrease in temperature. Therefore, cooling the membrane to 20 – 30 K below ambient may be useful with only a small energy cost compared to cryogenic distillation.

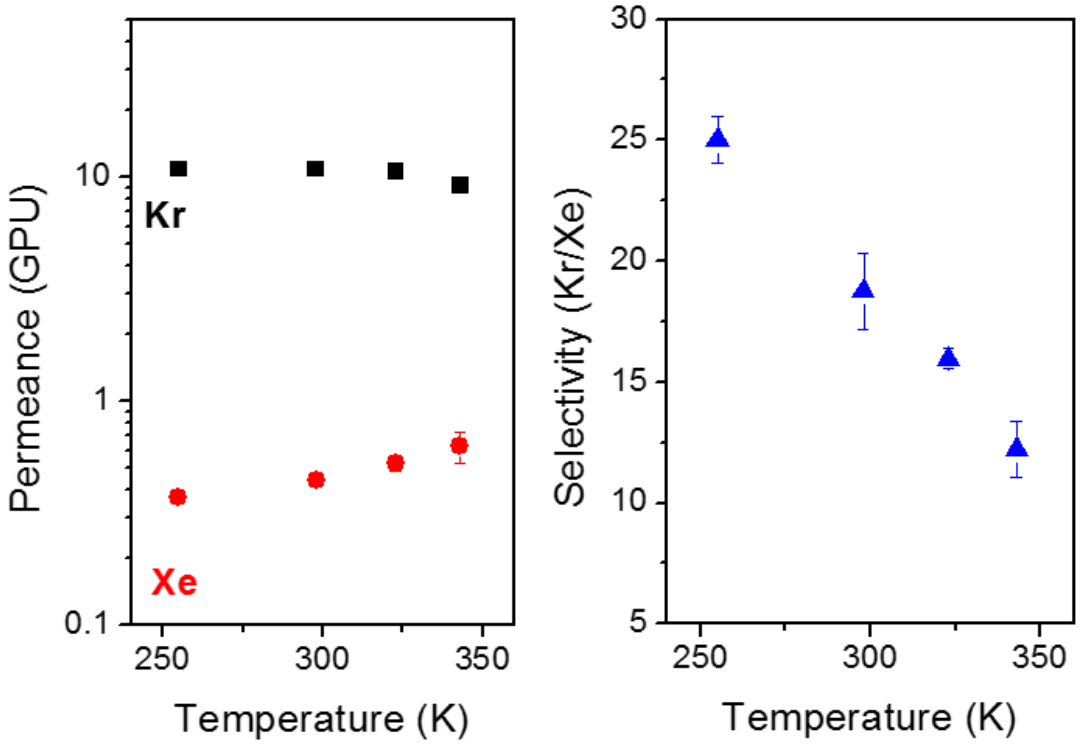

Figure 3.9. Temperature dependence of Kr and Xe mixture permeances and Kr/Xe mixture selectivity for tubular SAPO-34 membranes. The feed mixture is at 1 atm with 10 vol % Kr/ 90 vol % Xe.

3.3.5 Impact of radiation exposure on SAPO-34 membrane performance

An important question relating to the eventual application of the present membranes is the impact of radiation exposure (due to the radioactive off-gas feed streams) on membrane integrity and performance. In practice, the membranes would be exposed to ^{85}Kr, which is a lower-energy gamma emitter. The total activity of ^{85}Kr per unit membrane mass is limited by the gas-phase concentration and the relatively small amount of ^{85}Kr present in the membrane due to low concentration of ^{85}Kr in feed mixture. However, it is useful to evaluate the radiation stability since the zeolite membrane will receive a high gamma radiation dose over months/years of operation, which may result in radiation-induced crystal defects or crystal structure changes. We hypothesized that the present membrane would have good stability under radioactive Kr/Xe, mixtures since several zeolites are known to function effectively as adsorbents in other off-gas separations [68-70].

To obtain a reliable characterization of membrane performance under long-term radiation exposure, radiolytic exposure was performed using a ^{60}Co beta-gamma irradiator at Oak Ridge National Laboratory (ORNL). The ^{60}Co irradiator employed for this test was a JL Shepherd & Associates Model 109-68. It has a cavity 6 inches in diameter and 8 inches tall, which generates an unshielded exposure rate at 12,000 Roentgen hr^{-1}. Two membranes (R1 and R2) were prepared with Kr permeance of 10.4 ± 1.7 GPU and ideal selectivity of 15.5 ± 1.5 for radiolytic exposure. Since the interior of the irradiator is maintained under the same conditions as ambient air (containing atmospheric CO_2 and water vapor), a control sample was also prepared to investigate the

effect of humid (~ 40 % RH) CO_2 (410 ppm as of April 2018) under non-radioactive ambient conditions.

Table 3.3 shows the effect of radiation exposure on the performance of SAPO-34. After 30–60 days of ambient exposure in either radioactive (R1 and R2) or non-radioactive (Control) conditions, the Kr permeances of all the membranes increased by about 16% but the ideal Kr/Xe selectivity dropped by ~35%. Thus, the following conclusions can be drawn. Firstly, the change in SAPO-34 membrane performance is due to partial degradation by ambient air, most likely due to water vapor and CO_2 (an acid gas). It is reported that water vapor causes slow degradation of SAPO-34 due to breakage of Si-O-Al and Al-O-P bonds [71]. The continuous off-gas stream in practice, however, will be under dry conditions without water vapor or acid gases. Secondly, radiolytic exposure had no statistically significant additional effect over and above degradation by ambient air. Considering that 30 days of exposure to accelerated ^{60}Co gamma irradiation simulates about one year exposure to the off-gas containing ^{85}Kr, the results suggest that radiation stability is not a serious concern in SAPO-34 membranes for Kr/Xe separations. This should be confirmed with an experiment done under controlled dry conditions wherein the degradation effect of humidity and CO_2 does not exist. Unfortunately, such a setup is not available to us.

Table 3.3. Effects of radiolytic treatment of SAPO-34 membranes using Co-60 irradiator

		Before exposure			After exposure				
	Exposure time [days]	**Permeance [GPU]** Kr	Xe	**Ideal Selectivity (Kr/Xe)**	**Permeance [GPU]** Kr	Xe	**Ideal Selectivity (Kr/Xe)**	**Kr Permeance Increase [%]**	**Selectivity drop [%]**
R1	30	11.2	0.6	17.8	12.9	1.1	11.7	15.2	34.2
R2	60	13.1	0.8	16.1	15.4	1.5	10.2	17.6	36.6
Control – ambient for 60 days		9.5	0.7	14.6	10.7	1.1	9.8	12.7	32.8

3.4 Conclusion

SAPO-34 membranes that are selective for Kr/Xe separations were prepared on macroporous α-Al_2O_3 substrates *via* a steam-assisted seeding method followed by hydrothermal growth of polycrystalline membranes. SAC seeding method provided a continuous seed layer on the surface of the substrate, leading to the synthesis of defect-free SAPO-34 zeolite membrane. The observed permeance of Kr in SAPO-34 membrane was ~ 10 GPU with Kr/Xe separation selectivity 12 – 25, with the highest selectivity at the lowest measurement temperature (255 K). The temperature dependence of Kr and Xe permeances showed that the dominant transport mechanisms for Kr and Xe are different. Despite competing effects of adsorption and diffusion, the experimental results showed that SAPO-34 membranes effectively separate Kr form Xe due to their molecular sieving characteristics.

CHAPTER 4. ENHANCEMENT OF SAPO-34 MEMBRANE PERFORMANCE FOR KRYPTON / XENON SEPARATION[3]

4.1 Introduction

CHA (chabazite) framework type zeolites have a nominal pore size of 0.38 nm, which is in between the kinetic diameters of Kr (0.36 nm) and Xe (0.396 nm), and it has been shown that silicoaluminophosphate CHA (also referred to as SAPO-34) membranes are good candidates for Kr/Xe separation.[72, 73] Although the work described in Chapter 3 clearly shows that SAPO-34 membranes are promising for Kr/Xe separation, there is much potential for engineering the separation properties of these membranes with a view to improving selectivity and permeance, in order to mitigate the possible issues of high manufacturing cost of zeolite membranes.[74] In particular, three aspects are of interest in the present Chapter as described below.

Firstly, I study in detail the reduction of membrane thickness through a recently reported membrane fabrication method referred to as steam-assisted conversion (SAC) [65]. High manufacturing cost is a key factor limiting the commercial applications of zeolite membranes [75]. The most straightforward way to reduce the membrane cost is to reduce the required membrane area, which in turn can be accomplished by increasing the flux (throughput) *via* a reduction in the membrane thickness. However, thin (~ 1 μm)

[3] Reprinted with permission from Y. H. Kwon, B. Min, S. Yang, D.-Y. Koh, R. R. Bhave, S. Nair, "Ion-Exchanged SAPO-34 Membranes for Krypton–Xenon Separation: Control of Permeation Properties and Fabrication of Hollow Fiber Membranes", ACS applied materials & interfaces, 10, pp. 6361-6368. Copyright 2018 American Chemical Society.

zeolite membranes are challenging to fabricate since the control of defects becomes more difficult when growing thin zeolite layers on low-cost supports. The goal of this work is to develop approaches for SAPO-34 membrane thickness reduction (*i.e.*, Kr permeance increase) without reduction of Kr selectivity. Conventionally, polycrystalline zeolite membrane thickness control has been achieved by controlling the characteristics of deposition of seed crystals on to the membrane support (*e.g.*, porous disk, tube) from suspensions, and/or by controlling the secondary growth conditions that convert the seed layer into a continuous membrane.[76-78] However, the SAC method offers a different way of controlling membrane thickness: *in situ* formation of a thin zeolite seed layer by transformation of an amorphous reactant gel layer coated on to the substrate. Here I report significant decreases in membrane thickness and corresponding increases in flux by optimization of the SAC method.

Secondly, reports of SAPO-34 membranes for gas separation have mainly focused on the as-synthesized protonated form H-SAPO-34. It is well known that ion exchange of the extra-framework protons in zeolites with metal cations allows modulation and control of molecular flux and selectivity. However, very little is known about this aspect in the context of SAPO-34 membranes for Kr/Xe separation. The SAPO-34 crystal has a chabazite (CHA) zeolite topology, which is characterized by octahedral pore windows bounded by 8 T-atoms (T = Si, Al, or P). SAPO-34 is a silicoaluminophosphate zeolite with low Si/Al molar ratio < 1 and a chemical formula of $(Si_xAl_yP_z)O_2$, where x+y+z=1. In the SAPO-34 structure, Si atoms substitute P and Al at tetrahedral sites, avoiding Si-O-P linkages since Si-O-P bridges are energetically unfavorable [79]. Tuning the composition of Si, Al, and P leads to subtle variations in unit cell dimensions, which I

hypothesize to result in pore size changes (and hence changes in selectivity). Considering the formal charges on the Si (+4), Al (+3), P (+5), and O (-2) atoms, a net negative framework charge occurs when there are more Al atoms than P atoms (i.e., $y > z$) for a given number of Si atoms (i.e., fixed x). The negative charges must be balanced by cations (either H^+, or a metal cation if present in the synthesis solution) that are occluded in the pores. Here I report a detailed study of cation exchange of SAPO-34 membranes with the particular objective of increasing the Kr permeation selectivity. I interpret these results in relation to the existing knowledge of cation siting in the CHA-type materials. In addition, the reproducibility of zeolite membrane properties is an important issue in the literature, especially when characterizing performance improvements. In this work, through synthesis of ~30 membrane samples in total, I obtain a better assessment of membrane performance improvements based upon the average properties of the sample set.

Thirdly, I address the issue of scalability and low-cost fabrication of zeolite membranes by transferring the optimized SAC and ion-exchange methods to ceramic hollow fiber substrates. In general, membrane gas separation facilities have employed hollow fiber modules as separation units because of their unique characteristic of high membrane packing density, and high membrane surface to volume ratio. Normally, the membrane surface to volume ratio is about 300 – 500 m^2/m^3 for plate and frame modules, 600 – 800 m^2/m^3 for spiral wound modules and 2000 – 4000 m^2/m^3 for hollow fiber modules, which makes the system compact and economical. In addition, ceramic hollow fiber can be produced by a much cheaper process such as spinning, whereas tubular substrates are fabricated by slip casting method. Therefore, I demonstrate the fabrication

of SAPO-34/α-alumina hollow fiber membranes with separation characteristics consistent with those of the membranes developed on disk substrates.

4.2 Experimental Methods

4.2.1 Synthesis of SAPO-34 nanocrystals

SAPO-34 nanocrystals (~550 nm in average size) were prepared for seeding the α-alumina substrate prior to membrane synthesis. They were synthesized from a reactant molar composition of 1.0 Al_2O_3:1.0 P_2O_5:0.32 SiO_2:1.0 TEAOH:1.6 DPA (dipropylamine):52 H_2O. To prepare the seed crystals, Al(*i*-$C_3H_7O)_3$ (98%, Sigma-Aldrich), H_3PO_4 (85 wt% aqueous solution, Sigma-Aldrich), and deionized water were stirred for 3 h to form a homogeneous solution, then Ludox AS-40 colloidal silica was added, and the mixture was stirred for another 3 h. The TEAOH structure-directing agent (35 wt% aqueous solution) and DPA were then added and the homogeneous synthesis gel solution was aged for 4 days at 328 K. The solution was then placed in a Teflon-lined stainless steel autoclave (Parr) and heated at 493 K for 6 h. The solution was centrifuged and washed repeatedly for three times, and then dried overnight at 333 K. For the purpose of ion exchange, the crystals were calcined at 823 K for 6 h to remove the SDA.

4.2.2 Synthesis of SAPO-34 disk-type membranes

Porous α-alumina support disks (25.4 mm diameter, 1 mm thickness, Coorstek) were cleaned by sonication in acetone for 10 min and dried in an oven at 373 K for 24 h before use. In this study, two membrane fabrication methods were used (referred to as

M1 and M2 in the following discussion). For both methods, the substrates were seeded *via* the steam-assisted conversion (SAC) method.[65, 73] In order to avoid penetration of SAC solution into the pores, substrates were wetted with water and dried at ambient temperature for 1–2 min prior to coating. A clear solution was prepared by mixing deionized water, alumina isopropoxide (Al source), Ludox-AS40 (Si source), TEAOH, and phosphoric acid (P source), followed by addition of the previously synthesized seed nanocrystals with a concentration of 15 mg seeds/g mixture. The molar composition of the mixture (excluding the seed crystals) was 1.0 Al_2O_3:2.0 P_2O_5:0.6 SiO_2:4.0 TEAOH:75 H_2O. After evaporating 90% of water from the mixture at 353 K, the resulting gel-like paste was used to coat (with a gloved finger) the disk substrates with 0.06 mL paste/cm^2 support (for M1 membranes) or 0.02 mL paste/ cm^2 support (for M2 membranes). After drying at 323 K for 2 h, the substrates were placed vertically in Teflon-lined autoclaves with 4 mL of deionized water. The SAC process was carried out at 473 K for 24 h for the conversion of paste coating into continuous seed layer. For both M1 and M2, the synthesis gel for membrane growth had a molar composition of 1.0 Al_2O_3:1.0 P_2O_5:0.6 SiO_2:1.75 TEAOH:155 H_2O. Typically, the Al source, DI water, and P source were mixed and stirred for 2 h to form a homogeneous solution, then the Si source was added, and the mixture was stirred for an additional 30 min. Then TEAOH was added, and the resulting mixture was aged for 12 h at 328 K. The SAC-treated substrates were placed vertically in Parr autoclaves and hydrothermal growth was carried out at 483 K for 6 h. The membranes were calcined in air at 823 K for 6 h to remove the SDA.

4.2.3 Preparation of α-alumina hollow fibers

The alumina hollow fibers were prepared by a previously published recipe using a dry-wet spinning method followed by sintering in air.[37] The spinning dope suspension had a composition (wt%) of 38.0 NMP: 6.8 PES: 54.7 Al_2O_3: 0.5 PVP. First, *N*-methyl-2-pyrrolidone (NMP) and Al_2O_3 powder were mixed and sonicated (Branson digital sonicator) in eight sonication (30 s)-pause (30 s) cycles. The mixture was then heated in oil bath at 333 K under vigorous stirring. Polyvinylpyrrolidone (PVP) was added slowly into the mixture until dissolved. Then polyethersulfone (PES) was added and dissolved in four aliquots. After adding PES, the mixture was kept at 333 K and stirred for an additional 5 h. Then it was stored in vacuum overnight to remove air bubbles before use in fiber spinning. The spinning was conducted with dope and bore fluid flow rates of 120 and 80 mL/h, respectively. DI water and tap water were used as the bore fluid and external coagulant fluid respectively. Both the dope and water bath were at room temperature. The air gap was 3 cm. The fibers fell freely into the water bath bucket and were collected, soaked in DI water for 3 days (with the water changed daily) to exchange the residual solvent, and thoroughly dried. The raw fibers were then sintered at 873 K for 2 h followed by 6 h at 1773 K with a temperature ramping rate of 5 K/min. The finished fibers were of ~800 μm OD, ~160 μm wall thickness, and 35% porosity. Fiber lengths of 7 cm were used for membrane fabrication.

4.2.4 Synthesis of SAPO-34 hollow fiber membranes

SAPO-34 membranes on hollow fibers were fabricated by a process similar to disk-type membrane synthesis. Hollow fiber substrates were dipped in water and dried at

ambient temperature for 1 – 2 min. The SAC gel was then hand-coated on the fibers with 0.02 mL paste/cm^2 support. For this purpose, the gel was placed at one end of the fiber, held with two gloved fingers, and coated on the fiber in a single pass. The synthesis mixture composition was 1.0 Al_2O_3:1.0 P_2O_5:0.6 SiO_2:1.75 TEAOH:155 H_2O and the hollow fiber support seeded *via* SAC method was placed vertically in the autoclave. Zeolite membrane synthesis was carried out at 483 K for 6 h and the resulting membrane was calcined at 823 K for 6 h.

4.2.5 Ion-Exchange of SAPO-34 membranes

The acetate salts of three different monovalent cations (Li^+, Na^+, and K^+) were dissolved in ethanol to prepare ion exchange solutions. It is reported that exposure to water causes slow degradation of SAPO-34 due to breakage of Si-O-Al and Al-O-P bonds upon hydration.[71] Therefore, using ethanol as a solvent instead of water enables maintenance of SAPO-34 stability. Calcined H-SAPO34 membranes (M2 synthesis) were kept in the ion-exchange solution, which was stirred at 100 rpm at 333 K for 5 h. Ion exchange process was repeated three times until the amount of alkali cation in the SAPO-34 framework reaches equilibrium and does not change. The membranes were then rinsed with fresh ethanol thrice (1 h each time) and dried at 343 K overnight. Ion-exchanged M2 membranes were denoted M-M2 (M = Li^+, Na^+, or K^+).

4.2.6 Permeation Measurements

Single-component permeation measurements were conducted using in-house built permeation units operating in dead-end mode. Kr and Xe permeation measurements were carried out from 254 K to 298 K. For sub-ambient temperature (254 K), the membrane

module was submerged in a salt water-ice cooling bath. The membranes were degassed *in situ* under vacuum at 473 K for 12 h prior to each measurement. The feed pressure was maintained at 140 kPa and the permeate side was at 1 kPa. The fluxes were obtained by the standard method of measuring the rate of the initial linear pressure rise in a collection vessel on the permeate side after isolating the vacuum. The permeance is then calculated as the ratio of the measured flux and the pressure drop between the feed and permeate. Binary mixture permeation was measured in Wicke-Kallenbach mode at a system pressure of 110 kPa. The feed was 10 mol% Kr/90 mol% Xe mixture, generated by two mass flow controllers. A helium sweep (10 mL/min) was used to collect the permeate, whose composition was then analyzed by a gas chromatograph (Shimadzu GC-TCD-2014) equipped with a HP-PLOT 5A column (Agilent). The permeance of each component is obtained as its flux normalized by its transmembrane partial pressure. The Kr/Xe selectivity of the membrane is given as the ratio of permeances of each gas. For all reported permeation measurements, the permeances and selectivities are average values with standard deviations recorded from more than three membrane samples synthesized independently.

4.3 Results and Discussion

4.3.1 Development of Thinner Membranes for Enhanced Permeation Properties

Generally, thinner zeolite membranes are challenging to fabricate since the control of defects is more difficult when growing thin zeolite layers on microporous substrates. As I reported previously [73], the SAC seeding method provided smoother seed layers without pinholes or cracks, resulting in continuous SAPO-34 membrane layers after hydrothermal synthesis. In the present work, I hypothesized that the use of a thinner seed gel coating prior to SAC would result in the eventual formation of a thinner membrane upon secondary growth. **Figures 4.1a-4.1d** show SEM images of the surface and cross-section of polycrystalline M1 and M2 SAPO-34 membranes. The thicker M1 membranes are synthesized as described in our previous work[73], and are treated as a baseline. The average crystal grain sizes were found to decrease considerably from 5 μm (M1) to 2 μm (M2) as the SAC gel layer thickness was decreased. I also measured the membrane thicknesses using the P/Al ratio depth profile obtained by EDX line scanning on multiple samples (example shown in **Figures 4.1e-4.1f**).

The M1 membranes were found to have an average thickness of 5.6±0.5 μm, and after using smaller amount of SAC paste, the thickness of M2 membranes was considerably reduced and was determined as 2.1±0.5 μm.

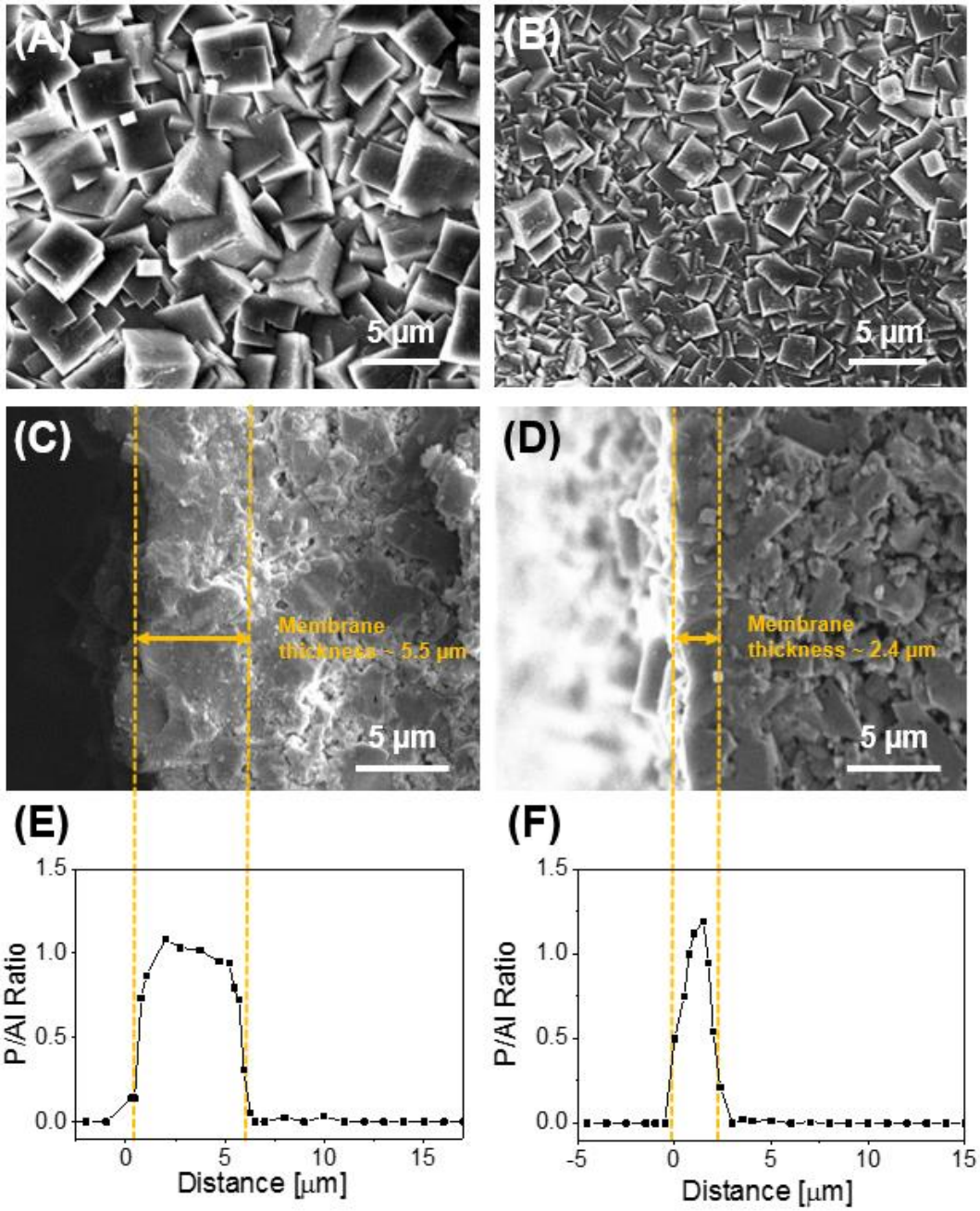

Figure 4.1. Example surface and cross-sectional SEM images of M1 (a, c) and M2 (b, d) membranes, and (e,f) the corresponding cross-sectional P/Al ratio profiles of each membrane as determined by EDX analysis. The yellow lines define the thickness of the membrane.

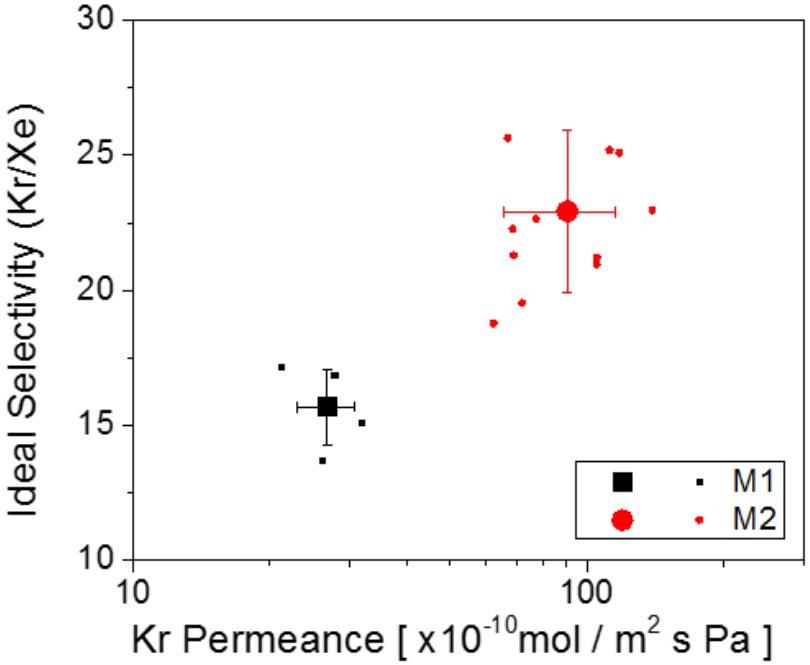

Figure 4.2. Single gas Kr permeances and ideal Kr/Xe selectivities of M1 (average thickness = 5.6 μm) and M2 (average thickness = 2.1 μm) membranes at 298 K. Each membrane sample is represented by the small symbols, and the large symbols are the averaged values.

Figure 4.2 shows the single-gas Kr and Xe permeances of a larger number of SAC-seeded SAPO-34 membranes at 298 K and 140 kPa feed pressure. The average Kr permeance of M1 membranes was obtained as $2.7\pm0.4\times10^{-9}$ mol m^{-2} s^{-1} Pa^{-1} with Kr/Xe ideal selectivity of 16±2. After thickness reduction (M2 membranes), the permeances systematically increased. The Kr permeance increased greatly to $9.1\pm2.4\times10^{-9}$ mol m^{-2} s^{-1} Pa^{-1}, with ideal selectivity 23±3. While the increase in permeance is a direct result of thickness reduction, the accompanying increase in Kr ideal selectivity is also significant and interesting. Although the reason for this effect is yet uncertain, it might be explained by the size of crystals comprising the membrane. M1 membranes have grain sizes of ~5

μm on the membrane surface whereas ~ 1.5 μm grains are seen in M2 membranes (**Figure 1a-1b**). Small crystal grains may interlock better than larger ones, resulting in the observed improvement in selectivity.

4.3.2 Control of Separation Properties via Ion Exchange

4.3.2.1 Ion Exchange of SAPO-34 Membranes

The greatly increased permeance of the M2 membranes suggests the application of ion exchange techniques to increase their selectivity while retaining a good Kr permeance (which should be at least as high as the baseline M1 membranes). **Figure 4.3** shows XRD patterns of ion-exchanged M2 membranes with different cations in the structure. The crystallinity of the SAPO-34 membranes is retained and no new (impurity) phases are seen, confirming that the use of ethanol as the ion exchange solvent prevents degradation or transformation of the SAPO-34 structure. The bulk compositions of the as-synthesized H-SAPO-34 and cation-exchanged M-SAPO-34 (M = Li, Na, K) membranes were determined using ICP-MS (H-SAPO-34 and Li-SAPO-34) and EDX analysis (H-SAPO-34, Na-SAPO-34, and K-SAPO-34) of the Si, P, and Al content. H-SAPO-34 was used as a reference to verify consistency between ICP-MS and EDX analysis. The H stoichiometry was calculated using a charge balance based upon the Based upon the measured atomic content of the other elements and the crystallographic SAPO-34 structure[71] with a fixed/known O stoichiometry. The composition (expressed on a unit-cell basis) of H-SAPO-34 membranes was estimated as $H_{1.5}Si_{4.3}Al_{16.6}P_{15.1}O_{72}$ (ICP-MS) and $H_{1.7}Si_{4.5}Al_{16.6}P_{14.9}O_{72}$ (EDX), which are in close agreement. The equilibrium degree of alkali cation exchange is notably different for the three cations

(Li^+, Na^+, and K^+). After Li^+ ion exchange, only 61% of the protons were exchanged to yield a composition of $H_{0.7}Li_{1.1}Si_{3.6}Al_{17.1}P_{15.3}O_{72}$, whereas the level of Na^+ ion exchange was 82% ($H_{0.3}Na_{1.3}Si_{4.3}Al_{16.7}P_{15.1}O_{72}$) and that of K^+ was 92% ($H_{0.1}K_{1.5}Si_{3.8}Al_{16.9}P_{15.3}O_{72}$). These results are found to be consistent with a previous computational study [80] that suggested a cation ion exchange selectivity order of K^+ > Na^+ > Li^+. Even though there is little information on the maximum amount of cations that can occupy the cation sites in SAPO-34, I verified that the amount of cations exchanged did not increase after repeated ion exchange. This creates confidence that the measured compositions represent the equilibrium/maximum extent of ion exchange for each cation under our ion-exchange experimental conditions.

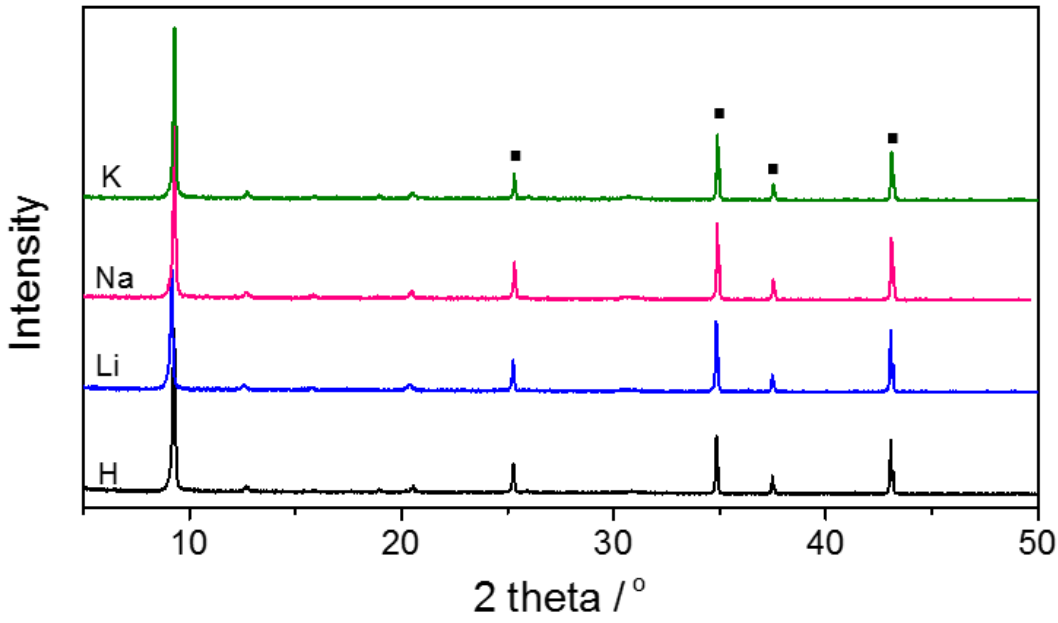

Figure 4.3. XRD patterns of H-SAPO-34 and M-SAPO-34 M2 membranes. (■): peaks from the underlying α-Al_2O_3 support.

The location, size, and number of cations can have significant effects on adsorption and diffusion behavior. **Figure 4.4** depicts the cation site locations in SAPO-34 [81]. Site I is located in a corner of the large ellipsoidal cage, site II is near the center of the cage, site III is in the double-six-membered ring (D6MR), and site IV is close to the 8MR window which is the limiting aperture for Kr and Xe transport [82].

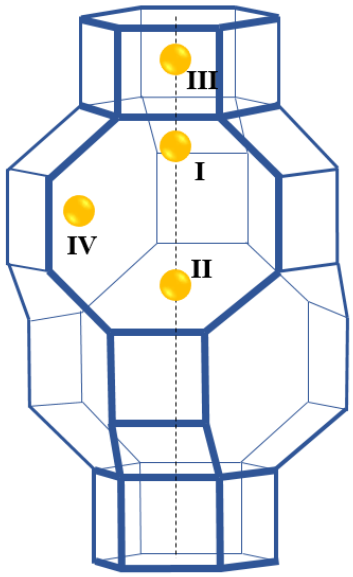

Figure 4.4. SAPO-34 (CHA) framework topology showing the four proposed cation sites (I-IV) in the large cages and in the double-six-membered rings (D6MRs). The vertices represent T-atoms (Si, Al, P) and the lines represent the T-O-T oxygen bridges

The small Li^+ cations strongly prefer site I and site II rather than site IV, whereas larger cations (K^+, Rb^+) prefer sites II and IV [83]. The intermediate-sized Na^+ cations showed a moderate preference for site IV over sites II and I at low loadings, but can be located in all three sites [84]. Sites I and II are expected to be fully filled with 0.5 Li^+ cations and site IV with 0.1 Li^+ cations respectively. For Na+ cations, sites IV and II are fully occupied with 0.5 Na^+ cations and the remaining 0.3 Na^+ cations are expected to be in site I. All three cation sites I, II, and IV are fully occupied with 0.5 K^+ ions since the

ion exchange selectivity is the highest for potassium ions [80]. Site III is not accessible to larger cations, and is only weakly occupied by smaller cations which have limited interactions with diffusing molecules. Cations in site II, being at the center of the CHA cage, may also not have a large effect on the transport of gases with kinetic diameters < 0.4 nm. Sites IV and I are likely to have the largest influence on modulating gas transport through CHA. Therefore, K^+ exchanged membranes are hypothesized to show the largest steric modulation of gas transport.

4.3.2.2 Adsorption Properties of Ion-exchanged SAPO-34

Figure 4.5 shows experimental single-component Kr and Xe adsorption isotherms on H-SAPO-34 and the three ion-exchanged M-SAPO-34 materials at 298 K over 10-300 kPa. All the materials preferentially adsorb Xe over Kr. Table 4.1 summarizes the textural properties obtained by N2 physisorption at 77 K, and the results of fitting the Kr and Xe adsorption isotherms with the Langmuir model. The BET surface area and micropore volume decrease monotonically (by 10 – 36 %) as the cation size increases (H+ < Li+ < Na+ < K+). I have shown by compositional analysis that the ion-exchanged cation loadings also increase with cation size. The Langmuir constants (b) are not strongly influenced by ion exchange, indicating that the van der Waals interactions between the noble gas atoms and SAPO-34 are not substantially affected by the cations. This is consistent with a previous report that lithium cation exchange does not notably change the heats of adsorption of CO_2 and CH_4 in SAPO-34 [71]. However, the Kr and Xe saturation capacities (qsat) decrease in the same order as the micropore volume, consistent with the decreased pore volume available as larger sizes and numbers of cations are introduced.

Table 4.1. Gas adsorption and textural properties of SAPO-34 materials as obtained from Kr and Xe adsorption (298 K) and nitrogen physisorption (77 K) isotherms.

		H-SAPO-34	Li-SAPO-34	Na-SAPO-34	K-SAPO-34
BET surface area [m^2/g]		480	429	323	306
Micropore volume [cm^3/g]		0.23	0.21	0.20	0.18
q_{sat} **[mmol/g]**	**Kr**	6.7	6.1	5.6	5.2
	Xe	5.2	4.8	4.4	4.1
b **[10^{-4} kPa^{-1}]**	**Kr**	9.0	8.3	8.2	8.2
	Xe	39	37	36	39

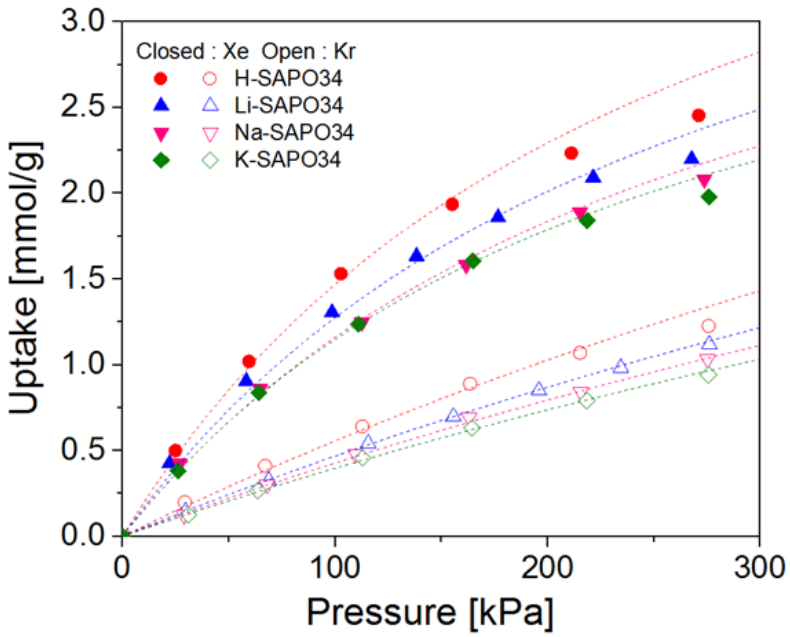

Figure 4.5. Single-gas Kr and Xe adsorption isotherms on H-SAPO-34 and ion-exchanged M-SAPO-34 materials. Symbols: experimental data, dashed lines: Langmuir model fits.

4.3.2.3 Single-component permeation and binary Kr/Xe separation

Figure 4.6a shows single-gas Kr permeance and Kr/Xe ideal selectivity data from the ion-exchanged M2 membranes at 298 K and 140 kPa feed pressure. For comparison, the data from M1 (baseline) and as-synthesized M2 membranes are also included from **Figure 4.2**. In **Figure 4.6b** I also plot the Kr permeabilities against the ideal selectivities to gain better insight on the effects of ion exchange. The Kr permeability of each membrane sample is obtained by dividing the Kr permeance by the apparent thickness of that membrane, the latter being determined from multiple SEM-based measurements along the cross-section. In **Figures 4.6a-4.6b**, the single-component Kr permeances and permeabilities of all the three types of ion-exchanged membranes decrease relative to the as-synthesized M2 (H-SAPO-34) membranes, but there are significant differences between the ion-exchanged membranes. At a feed pressure of 140 kPa, **Figure 4.5** shows that the differences in Kr adsorption are not large (~25%) and cannot by themselves explain the reduction in permeability relative to the H-SAPO-34 membranes. Therefore, it is attributed mainly to the reduction in diffusivity as a result of a lower effective pore size after alkali cation exchange. However, the Xe adsorption isotherms show larger differences and hence may play a more significant role along with diffusivity decreases. To separate these effects formally, I use the Maxwell-Stefan equation for the single-component permeability (P) of a nanoporous membrane [48]:

$$P = \rho q_{sat} D_{MS}^{o} \exp\left(\frac{-E_a}{RT}\right) \ln\left(\frac{1+bp_f}{1+bp_p}\right) \tag{4.1}$$

Here, p_f and p_p are the pressures of the feed and permeate, ρ is the density (1800 kg/m^3) of the SAPO-34 zeolite, and q_{sat} and b values are adsorption parameters given in **Table 4.1**. Using the experimental permeability data (**Figure 4.6b**) and the Langmuir adsorption parameters (**Table 4.1**), I obtain the effective M-S diffusivity of Kr and Xe for each membrane sample, and then average these to obtain statistically valid M-S diffusivities for each of the four types of M2 membranes (as-synthesized and ion-exchanged). These values are shown in **Table 4.2.** For all the SAPO-34 membranes considered here, the diffusion selectivity (molecular sieving effect) for Kr exceeds the preferential adsorption of Xe, leading to high Kr/Xe permeation selectivity. It is seen that the M-S diffusivities of Kr and Xe decrease monotonically as the size of the cation increases. This is attributed to the reduction in effective pore size which hinders the passage of molecules through the 8MR windows [57]. M-S diffusivities of both Kr and Xe decrease after ion exchange, but the effect of cation exchange on diffusivities is more significant for Xe (50-58% reduction) than Kr (23-26%), thereby leading to a large increase in diffusion selectivity. Combined with the adsorption behavior, I also obtain large increases in permeation selectivity as well. The ideal (single-component) permeation selectivity of cation-exchanged membranes increases by 40-63% relative to H-SAPO-34 membranes. Although the permeances are reduced after ion exchange, the resulting values are still considerably higher than the baseline M1 membranes due to the effect of thickness reduction in M2 membranes.

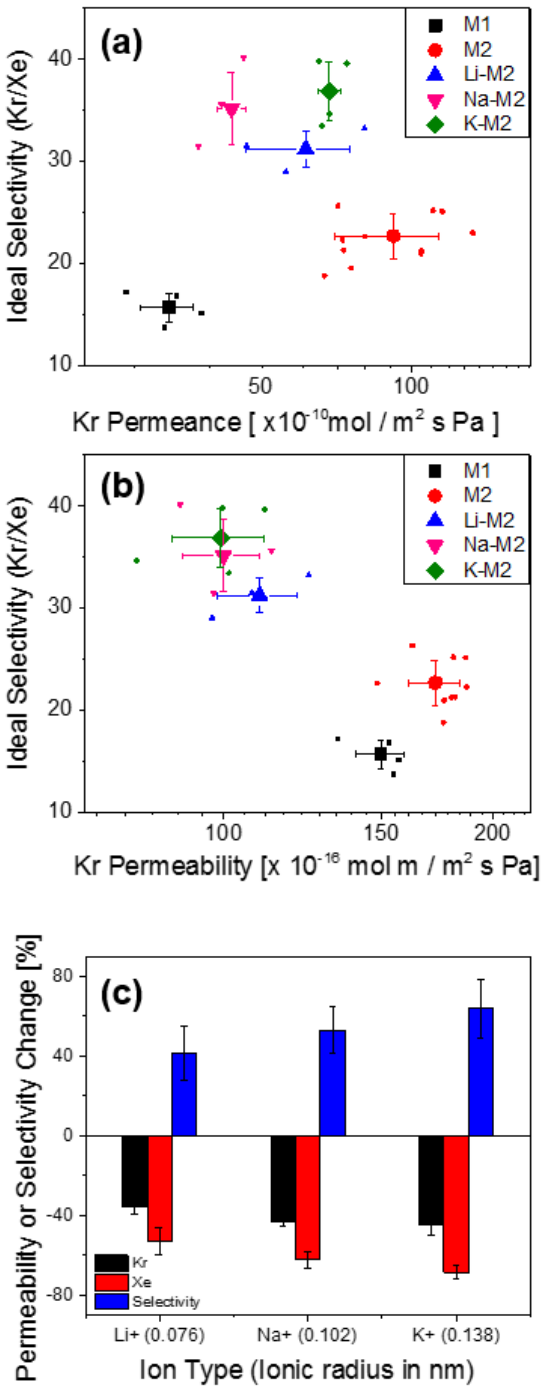

Figure 4.6. (a) Single-component Kr permeances versus selectivities, and (b) Single-component Kr permeabilities versus selectivities, for M1, M2, and ion-exchanged M2 membranes at 298 K and 140 kPa feed pressure. Each membrane sample is represented by small symbols and corresponding large symbols are the averaged values for each type of membrane. (c) Percent changes (from M2) in permeabilities and Kr/Xe selectivities as a function of cation radius.

Overall, there are large differences between the Kr permeabilities of H-SAPO-34, Li-SAPO-34, and Na-SAPO-34 membranes. Additionally, the Kr/Xe selectivities of the above three membranes are very different, as a result of significant difference in Xe permeabilities are very different. K-SAPO-34 shows smaller differences from Na-SAPO-34 in both adsorption and permeation properties, but **Table 4.2** and **Figure 4.6c** show that the Kr/Xe diffusion selectivity and permeation selectivity of K-SAPO-34 are higher than that of Na-SAPO-34. Among the ion-exchanged membranes in **Figure 4.6**, K-SAPO-34 appears to be the best candidate due to its high ideal selectivity (~37) and only modestly reduced Kr permeance ($6.3\pm0.3\times10^{-9}$ mol m^{-2} s^{-1} Pa^{-1}). The separation properties of K-M2 and M2 membranes for a binary 10/90 (molar ratio) Kr/Xe mixture were characterized as a function of temperature at a feed pressure of 100 kPa (**Figure 4.7**). The binary Kr permeances increase with decreasing temperature whereas Xe permeances decrease. As a result, the binary Kr/Xe separation factor increases with decreasing temperature. Clear molecular sieving effects are seen. The Kr/Xe separation factor in K-SAPO-34 membranes is 48±3 at 253 K and 30±5 at 298 K.

Table 4.2. M-S diffusivities and Kr diffusion selectivities in SAPO-34 membranes.

	D_{Kr} [$\times 10^{-14}$ m^2/s]	D_{Xe} [$\times 10^{-14}$ m^2/s]	Diffusion Selectivity
M2	172 ± 12	2.78 ± 0.5	65.2 ± 8.7
Li-M2	133 ± 13	1.51 ± 0.1	94.3 ± 6.2
Na-M2	130 ± 12	1.26 ± 0.2	107 ± 10.3
K-M2	128 ± 12	1.04 ± 0.1	122 ± 8.9

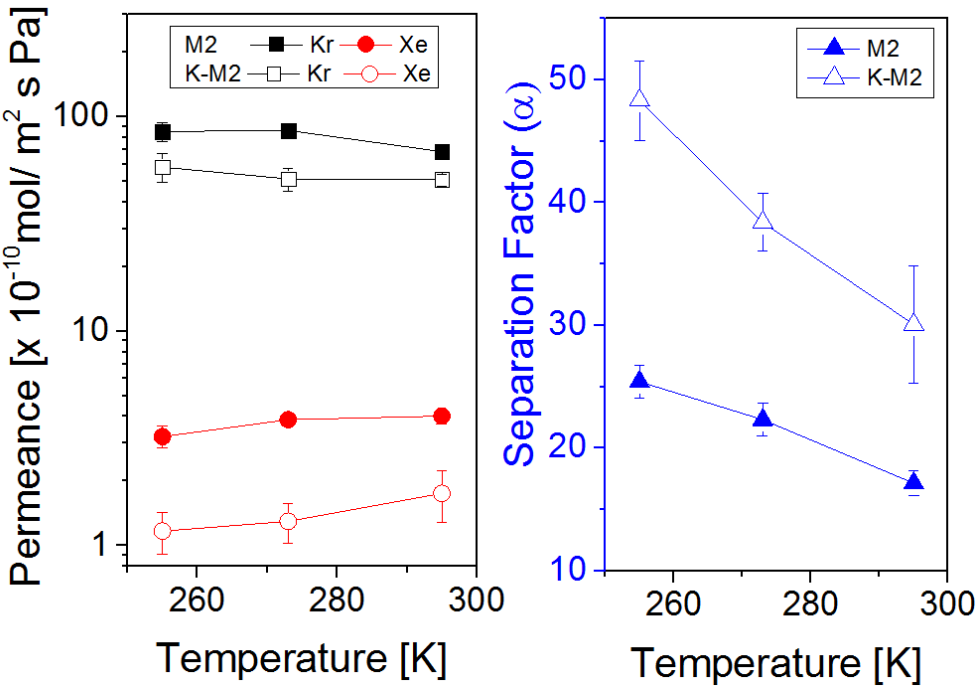

Figure 4.7. Temperature dependence of binary Kr and Xe permeances and Kr/Xe separation factors in disk H-SAPO-34 (M2) and ion-exchanged K-SAPO-34 (K-M2) membranes.

4.3.3 SAPO-34 Membrane Synthesis on Ceramic Hollow Fiber

The SAC and hydrothermal growth methods for M2 membranes were applied to α-alumina hollow fiber supports of 800 μm OD. **Figure 4.8** shows representative SEM images of a H-SAPO-34 membrane fabricated on the outer surface of a hollow fiber. The average crystal grain size is ~3 μm and the apparent (SEM) membrane thickness is determined as 3.2±0.4 μm. The average single-gas Kr permeance is $6.5 \pm 0.4 \times 10^{-9}$ mol/m^2 s Pa with ideal selectivity of 31.7 ± 13.3 at ambient temperature, which is comparable to the permeation performance of K-M2 disk-type membranes. I then investigated the separation of a binary Kr/Xe mixture with hollow fiber SAPO-34 membranes before and after ion exchange with potassium cations. **Figure 4.9** shows the temperature dependence of Kr/Xe binary mixture permeation. The binary mixture separation showed improved selectivities after ion exchange at all temperatures with clear molecular sieving effects. Comparison with **Figure 4.7** shows similar separation characteristics of the hollow fiber membranes and the disk-type membranes.

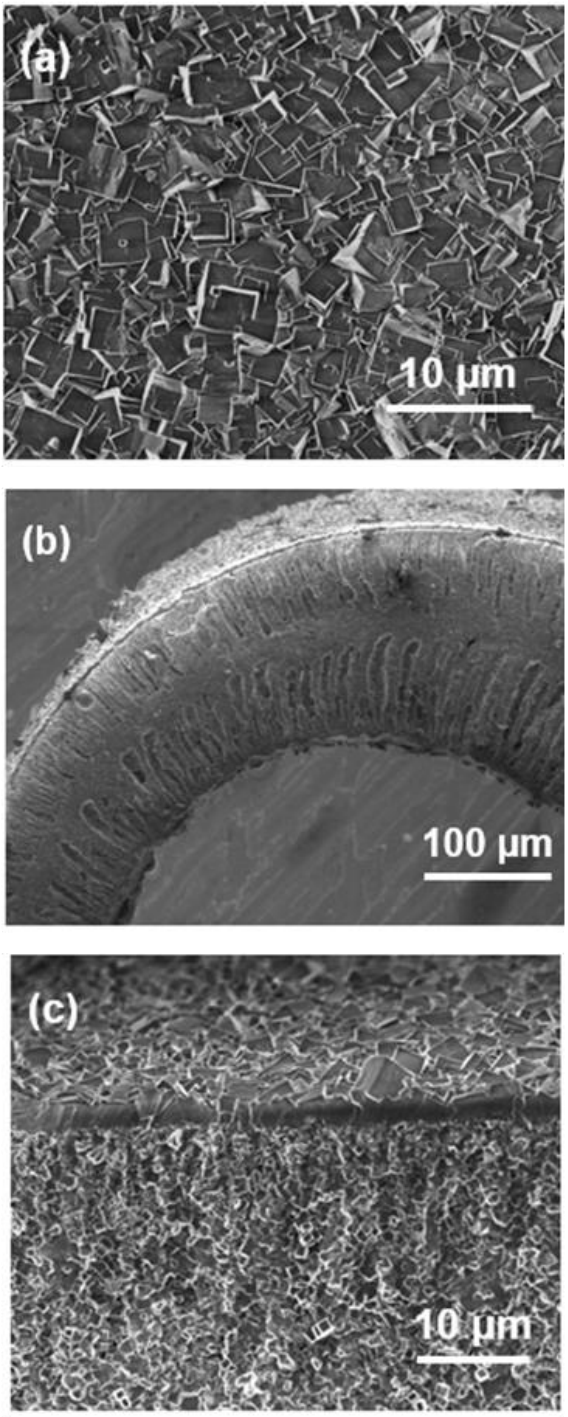

Figure 4.8. (a) Top view and (b), (c) cross-sectional SEM images of a SAPO-34 membrane fabricated by SAC seeding, hydrothermal secondary growth, and ion exchange on an α-alumina hollow fiber.

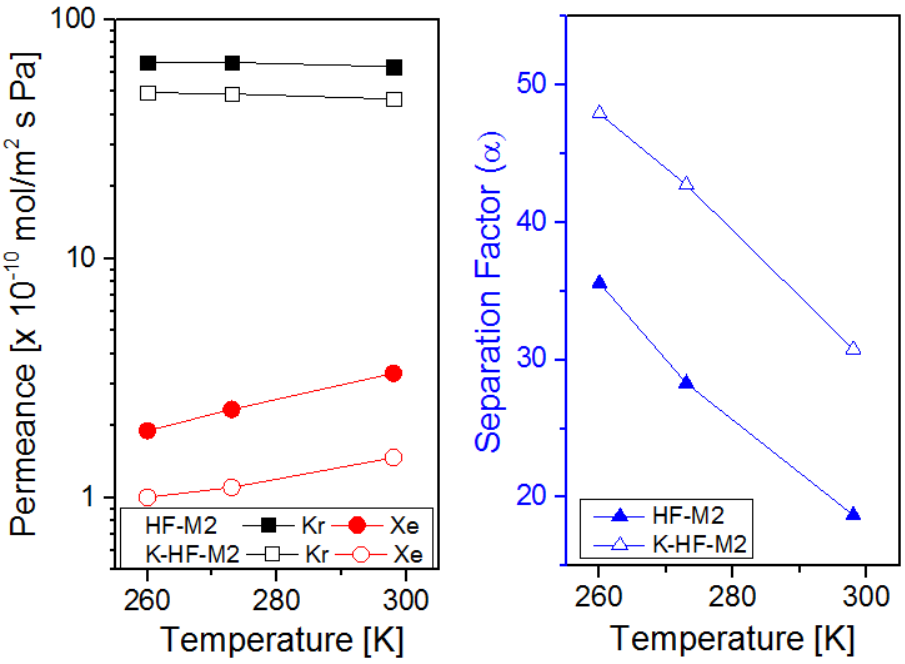

Figure 4.9. Temperature dependence of binary Kr and Xe permeances and Kr/Xe separation factors in hollow fiber H-SAPO34 and ion-exchanged K-SAPO-34 hollow fiber membranes.

4.4 Conclusion

SAPO-34 membranes with reduced thickness and increased permeance were successfully synthesized by controlling the steam-assisted conversion (SAC) seeding method followed by hydrothermal secondary growth. This work is of significance because it shows that the final membrane thickness can be controlled by simply controlling the applied amount of the SAC paste per unit area without changing any other parameters of the secondary growth procedure. These results were reproducible for ~30 membranes in different batches, which is an encouraging result for scaled-up fabrication. After post-synthesis ion exchange with alkali metal cations, excellent Kr/Xe permeation

selectivity was obtained with slight decrease in Kr permeance. The adsorption, diffusion, and permeation characteristics of the cation-exchanged membranes were obtained experimentally and revealed the enhanced molecular sieving effect of the cations in the pores of SAPO-34. Having obtained high-performance ion-exchanged SAPO-34 membranes on disk-type supports, I successfully transferred the fabrication methodology to ceramic hollow fiber supports. The high quality of the SAPO-34 hollow fiber membranes make it possible to realize a compact and low-cost Kr/Xe separation membrane system in the future, for noble gas separation processes in nuclear fuel reprocessing and other applications.

CHAPTER 5. ZEOLITE MEMBRANE TRANSPORT MODELING AND TECHNOECONOMIC ANALYSIS

5.1 Introduction

As mentioned in Chapter 1, zeolite membranes have shown great separation properties at laboratory scale for a variety of applications such as hydrogen recovery, CO_2 capture, xylene isomer separation, and butane isomer separation [85-88]. Due to their simplicity, scalability, and compactness, membranes are considered as an attractive process alternative for gas separations [89, 90]. The operation and maintenance of zeolite membrane system is minimal because there are not moving parts so the systems can be operated in remote areas. However, few industrial application such as solvent dehydration and liquid separation has been developed as separation system that utilizes zeolite membrane for separation in industry [37, 38, 42, 91]. Therefore, an industrial implementation of zeolite membrane is still required for gas separation application and it is necessary to evaluate it first whether the technology is economically beneficial and can substitute the current technology. Previous reports have shown that I can evaluate the membrane system by estimating the size of system and required cost of membrane separation by mathematical modeling and process design using finite differential equations. It is expected that the techno-economic evaluation will provide the perspective of membrane system which can substitute energy-intensive cryogenic distillation.

For the technoeconomic analysis (TEA) of the membrane system, a reliable model should first be developed to predict the membrane performance under different

conditions. Krishna and co-workers developed the Maxwell-Stefan approach of gas transport through zeolite membranes which provides a proper description of multi-component diffusion in defect-free zeolite membranes [48, 54, 92-95]. The generalized Maxwell-Stefan equations have been applied successfully into many systems to describe diffusive transport phenomena in multicomponent mixture such as hydrocarbon separation in MFI zeolite membrane [93, 96-98]. SAPO-34 is a well-known zeolite with chabazite topology, and so I can use Maxwell-Stefan equations with appropriate assumptions for prediction of Kr/Xe separation. This model can then be verified by comparing with experimental data and included in the actual model describing the permeation through zeolite membranes within a wide range of operating conditions in industrial use. Previous studies have examined the viability of membrane technology for H_2 purification or CO_2 capture from syngas streams [89, 99-101]. Therefore, one can utilize this systematic analysis methodology to analyze the economic potential of zeolite membranes for Kr/Xe separation. The implementation of membrane technology in Kr/Xe separation step from the nuclear fuel cycle is expected to yield two main advantages. The primary advantage is to minimize the gaseous radioactive waste volume contaminated by ^{85}Kr. Moreover, a possible revenue can be generated by the sale of purified Xe, which can only be produced from cryogenic distillation of air [102, 103].

In this chapter, a multicomponent Maxwell-Stefan model for Kr and Xe permeation in SAPO-34 membranes is developed. This Maxwell-Stefan equation includes the adsorption and diffusion parameters which were obtained from Chapter 3 and Chapter 4. The Maxwell-Stefan membrane model is then integrated into an overall process model for a cross-flow membrane system. The number of stages required to

achieve specified product purity is calculated by multi-stage system modeling and optimized scheme for each case is suggested. This work has been carried out in collaboration with Prof. Michael Tsapatsis and Dr. Nitish Mittal at the University of Minnesota. In particular, the work described in Section 5.2 was carried out entirely at Georgia Tech and independently validated/cross-checked at the University of Minnesota, whereas the work described in Section 5.3 and Section 5.4 was carried out in close coordination with approximately equal effort at Georgia Tech and the University of Minnesota.

5.2 Transport Model for Zeolite Membrane Layer

5.2.1 Single component Maxwell-Stefan Model

The permeation properties of Kr and Xe through the zeolite membrane can be modelled by a well-known Maxwell-Stefan equation for the interpretation of measured experimental data on permeation. The Maxwell-Stefan formulation of single component membrane can be expressed as:

$$N_i = -\rho \mathrm{q}_{i,sat} \mathcal{D}_i \left(\frac{\theta_1}{RT} \nabla \mu_i \right) \tag{5.1}$$

where $q_{i,sat}$ represents the saturation loading, θ_i is a fractional occupancy, and μ_i is the chemical potential of the sorbed species *i*. D_i is the M-S diffusivity which reflect interactions between species *i* and the zeolite matrix. This equation is solved analytically

by assuming equilibrium between sorbed species and the bulk fluid phase, and using single component Langmuir isotherm.

$$N = \frac{\rho q_{sat} \mathcal{D}_{i0}}{L} \exp\left(\frac{-E_a}{RT}\right) \ln\left(\frac{1+bp_f}{1+bp_p}\right) \tag{5.2}$$

Here, p_f and p_p are the pressures in the feed and permeate, ρ is the density of the zeolite, and L is the membrane thickness. The above equation is valid for the regime when the M-S diffusivity is not a function of the adsorption loading, *i.e*. the hopping rate of a molecule is not significantly slowed down by the presence of other molecules. This is called the "weak confinement" scenario. For the diffusion of large guest molecules such as SF_6 or CF_4, diffusivitiy is dependent on loading and $\mathcal{D}_i$ decreases strongly with the loading, i.e. a "strong confinement" scenario. The two cases can be modeled approximately with the following equations:

$$\mathcal{D}_i(\theta) \sim \mathcal{D}_i(0)(1-\theta) \text{ (strong confinement)} \tag{5.3}$$

$$\mathcal{D}_i(\theta) \sim \mathcal{D}_i(0) \text{ (weak confinement)} \tag{5.4}$$

The weak confinement scenario is generally a good assumption in zeolites that have multidimensional pore networks (such as SAPO-34) and at low/moderate pressures (such as those considered here).

The adsorption and diffusion parameters in **Table 2.1** and **Table 2.2** were used for these predictions, whose results are shown as solid lines in **Figure 5.1**. Overall, the model predictions are in very good agreement with the experimental data, and they

correctly predict the magnitude and the temperature dependence of the permeances of both Kr and Xe. It is also important to note that the M-S permeation equation used here corresponds to the regime in which the M-S diffusivity is essentially independent of adsorption loading, *i.e*. the hopping rate of a molecule is not significantly affected by the presence of other molecules. The correctness of this assumption is corroborated by several factors. Firstly, I have also predicted the temperature dependence using the M-S equation for the opposing case in which the M-S diffusivity is taken as a linearly decreasing function of the loading and approaches zero as the saturation capacity is reached.[94] However, this equation does not correctly predict the temperature dependence or the magnitude of the permeances. Secondly, the adsorption isotherms (**Figure 2.3**) show that a membrane operating at a feed pressure of 100 kPa and vacuum on the permeate side is quite far from saturation loading of either Kr or Xe. Finally, other

researchers have recently proposed the same explanation for gas permeation through other small-pore zeolite or MOF materials, based upon experimental and molecular simulation data [17].

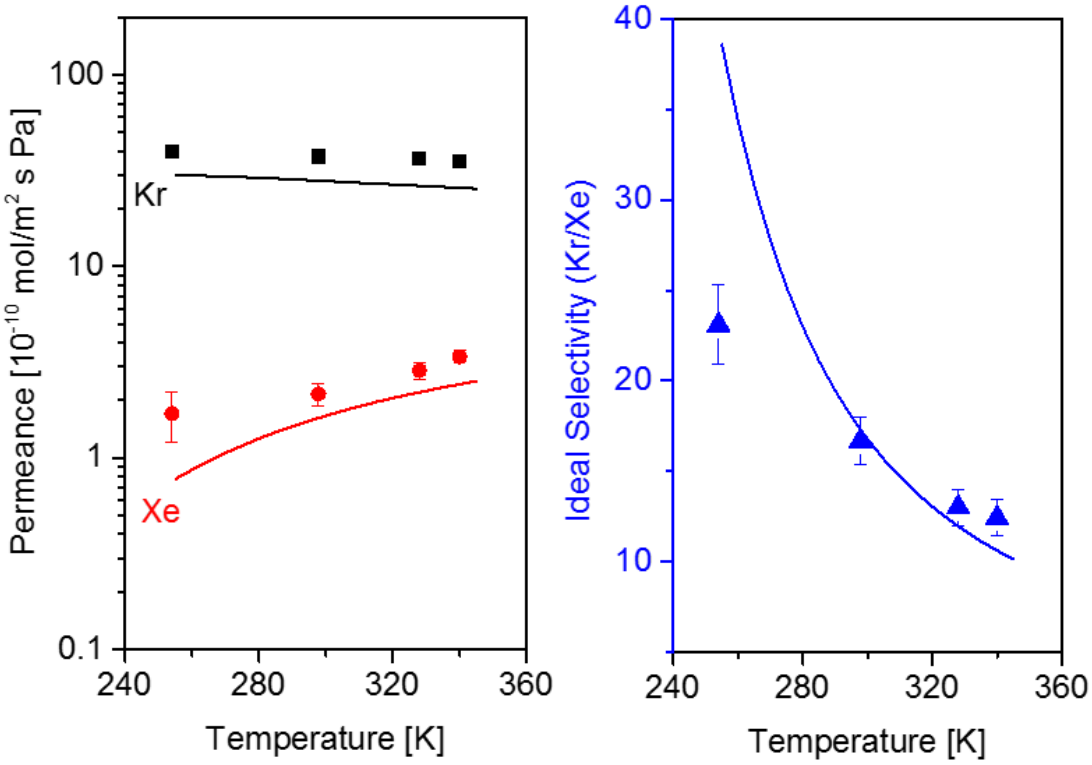

Figure 5.1. Comparison of experimental data and Maxwell-Stefan model prediction in single component permeation in tubular membrane.

Some quantitative deviation in the selectivity value is seen at sub-ambient conditions (254 K). This may be due to the fact that the selectivity (in this case) is a ratio of a large and a small permeance value, which becomes highly sensitive to the Xe permeability at sub-ambient conditions wherein the Xe permeability is very small. The Xe permeability can be strongly influenced by the presence of even a small number of defects. One way to quantify the extent of defects is to treat the measured permeance of SF_6 - a large molecule with kinetic diameter 0.55 nm - as arising entirely from Knudsen

diffusion through non-zeolitic pores (defects). The SF_6 permeance is 0.9×10^{-11} $mol.m^{-2}.s^{-1}.Pa^{-1}$ at 254 K. The corresponding Kr and Xe defect permeances are estimated by multiplying with the Knudsen factor (the square root of the ratio of inverse molecular masses, which is equal to 1.31 for Kr and 1.04 for Xe). When the observed permeances of Kr and Xe are corrected by subtracting the estimated defect permeance, the ideal Kr/Xe selectivity is calculated to be marginally higher (26).

The time-lag method [104] can also be used to estimate the defect permeance of Xe in the SAPO-34 disk membrane. It is assumed that permeation of gas molecules through defects is governed by Knudsen diffusion. The defect permeance can be calculated using the time-lag analysis. Consider a defect-free membrane across which a pressure gradient is maintained by a vacuum pump. At time t = 0, the vacuum pump is isolated and permeate-side pressure is allowed to build up. However, there will be an initial time lag (breakthrough time) for gas molecules to diffuse through the membrane layer of known thickness. During this time lag period, no increase in permeate-side pressure will be seen. In a defective membrane, an initial increase in permeate-side pressure will occur due to fast permeation through defects, followed by an inflection and change in slope of the permeate-side pressure as gas molecules diffusing through the membrane also break through (**Fig. 5.2**). The defect permeance can be calculated by assuming that all the observed flux through the membrane before the time-lag inflection point is through the defects. Eqn. 5.5 is then used to calculate the defect permeance. The flux through the defects can be estimated by:

$$N_i = \frac{D_{e_i}}{l_M}\left(C_{i_L} - C_{i_0}\right) \tag{5.5}$$

where D_{e_i} is the effective diffusivity through the membrane defect, l_M is the membrane thickness, Ci_L and Ci_0 is the concentration at permeate and feed side, respectively.[104]

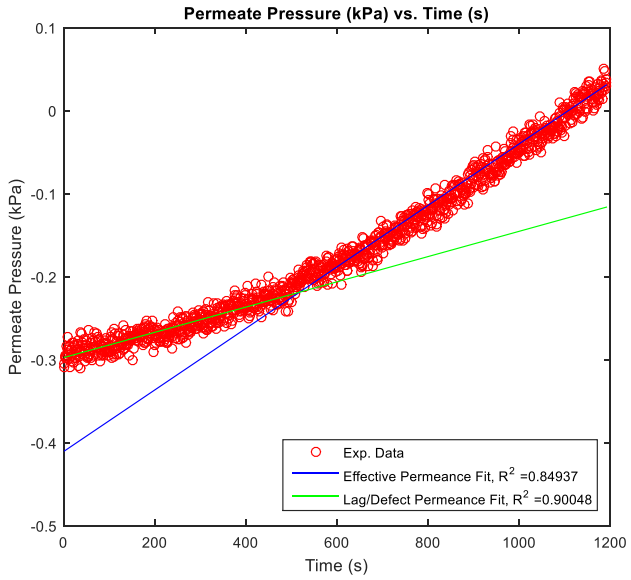

Figure 5.2. Permeate-side pressure of Xe measured versus time at 255 K. The lag time was estimated as 437 s.

By this method, the Xe defect permeance was estimated as 4.1×10^{-11} mol.m^{-2}.s^{-1}.Pa^{-1}. The ideal selectivity of a defect-free SAPO-34 membrane at 254 K is extrapolated to be 30, which is closer to the M-S prediction of 38. It is also possible that polycrystalline zeolite films may exhibit some differences in diffusion and adsorption characteristics compared to powder crystals (*e.g.*, due to the existence of tensile or compressive stresses in the film), and these differences may also depend on the membrane type (disk versus tube). However, our main objective in this work was to evaluate whether the MS model – parameterized from adsorption and diffusion measurements on crystals – can quantitatively predict the trends in membrane permeation properties. The results of **Figure 5.1** show that such a hypothesis is overall justified.

5.2.2 Multicomponent Maxwell-Stefan Model

Krishna et al. have extended the single component permeation model into multi-component Maxwell-Stefan approach, which provides a fundamental description of gaseous mixture permeation though the membrane.

$$-\rho\frac{\theta_i}{RT}\nabla\mu_i = -\rho\sum_{j=1}^{n}\Gamma_{ij}\nabla\theta_j = \sum_{j=1,j\neq i}^{n}\frac{q_jN_i - q_iN_j}{q_i^{sat}q_j^{sat}\mathcal{D}_{ij}} + \frac{N_i}{q_i^{sat}\mathcal{D}_i} \qquad i = 1,2,..n \quad (5.6)$$

where ρ is the density of the zeolite, q_i^{sat} represents the saturation loading, θ_i is a fractional occupancy, and μ_i is the chemical potential of the sorbed species *i*. Γ is the thermodynamic correction factor, $\mathcal{D}_i$ is the M-S diffusivity, *N* is flux, and $\mathcal{D}_{ij}$ is the exchange coefficient. Equation 5.6 can then be rewritten as n-dimensional matrix expressing the fluxes as

$$(N) = -\rho[q_{sat}][B]^{-1}[\Gamma](\nabla\theta) \quad (5.7)$$

where M-S diffusivity matrix is defined as

$$B_{ii} = \frac{1}{D_i} + \frac{\theta_j}{D_{ij}} \;;\; B_{ij} = -\frac{\theta_i}{D_{ij}} \quad (5.8)$$

The estimation of $\mathcal{D}_{ij}$ was suggested by Krishna and Wesselingh with the logarithmic interpolation formula, which is called as Vignes correlation.

$$\mathcal{D}_{ij} = [\mathcal{D}_i]^{\theta_i/(\theta_i+\theta_j)}[\mathcal{D}_j]^{\theta_j/(\theta_i+\theta_j)} \quad (5.9)$$

For zeolite topologies with high connectivities between pores and channels, the exchange coefficient $\mathcal{D}_{ij}$ is assumed to be infinite, which means that particle-particle

exchange is facile (**Figure 5.3**). For zeolites such as CHA and DDR, it is reported that the inter-cage hopping of Kr or Xe molecules through the pore windows are independent each other at lower pressures where neither molecule approaches its saturation loading. As a result, the off-diagonal terms of the *B* matrix are zero.

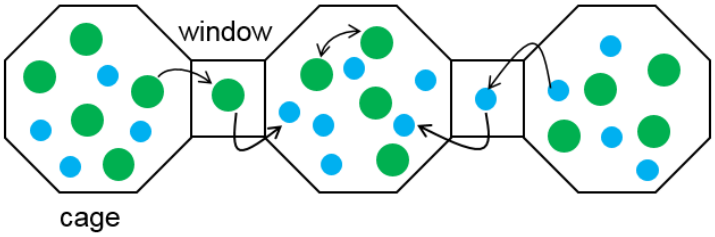

Figure 5.3. Pictorial representation of the molecular jumps in cage separated by windows (e.g. CHA, FAU, LTA, ERI etc).

There are several more key assumptions that need to be considered. Since the crystals comprising the membranes are well-interlocked, only intracrystalline diffusion is considered and intercrystalline diffusion is neglected. The actual permeance of zeolite membrane synthesized on a support layer can be calculated as:

$$\frac{1}{\bar{P}_{M,effective}} = \frac{1}{\bar{P}_{M,zeolite}} + \frac{1}{\bar{P}_{M,substrate}} \tag{5.10}$$

In general, the permeance that we measure from the apparatus is effective permeance, not a pure zeolite permeance. If the effective permeance ($\bar{P}_{M,effective}$) is high enough to be comparable with the permeance through the substrate($\bar{P}_{M,substrate}$), we need to use the Eqn 5.10 to calculate the permeance through the zeolite membrane ($\bar{P}_{M,zeolite}$). However, the effective permeances of Kr (10 – 40 GPU) and Xe (1 – 5 GPU) are relatively small compared to permeances through the substrates (~ 5000 GPU), making the last term in the equation 5.10 into zero. Therefore, it is assumed that the flux

through the alumina substrate is neglected. Finally, as explained in Section 5.2.1, the weak confinement model is considered wherein there is no significant effect of loading on diffusion.

As explained in Section 2.3.3 and **Figure 2.5**, the binary adsorption was estimated using double Langmuir isotherm without need of using IAST prediction. I have verified that the double Langmuir isotherm provides an excellent approximation of the more accurate IAST predictions in the range of pressures (up to 1.5 atm) relevant here. Therefore, thermodynamic correction factor can be simplified as:

$$\Gamma \equiv \left[\frac{\theta_i}{\theta_j}\frac{\partial\, ln f_i}{\partial \ln \theta_j}\right] = \frac{1}{1-\theta_i-\theta_j}\begin{bmatrix} 1-\theta_j & \theta_i \\ \theta_j & 1-\theta_i \end{bmatrix} \tag{5.11}$$

The permeation characteristics of the binary 10 % Kr/ 90 %Xe mixture was modeled using the Maxwell-Stefan equations for two components (**Figure 5.4**). As discussed earlier, the double Langmuir isotherm was used to approximate the binary mixture adsorption behavior and diffusion properties obtained from kinetic uptake data (**Table 2.1** and **Table 2.2**). The predicted membrane characteristics are in good agreement with the experimental results. As in the case of single-gas permeation, the slight difference in selectivity between the M-S model and experimental data was due to the uncertainty in experimental determination of the Xe permeability.

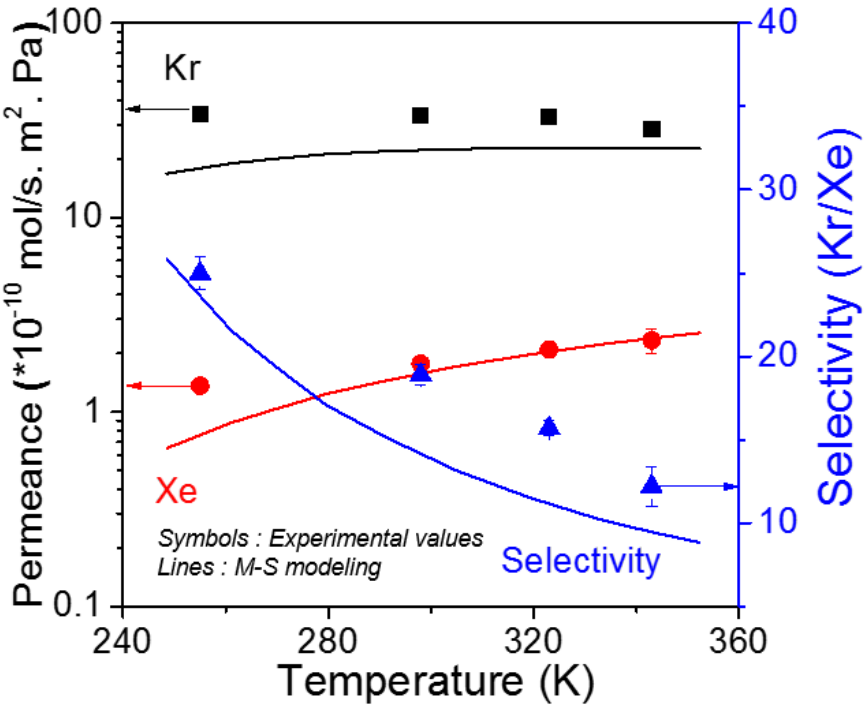

Figure 5.4. Predicted (lines) temperature dependence of Kr/Xe separation performance for tubular SAPO-34 membranes and comparison with experimental data (symbols).

Since I successfully synthesized membranes with improved permeances and selectivities (Chapter 4), the separation performances of SAPO-34 membranes were investigated and predicted after thickness reduction and post-synthesis ion exchange. The adsorption and diffusion parameters were obtained from adsorption isotherm and single component permeation experiments and are shown in **Table 4.1** and **Table 4.2**. As shown in **Figure 5.5,** the predictions show excellent agreement with experimental results at 298 K in 10 % Kr and 90% Xe mixture. This indicates that the assumptions for zeolite membrane modeling sufficiently explain the gas transport through the SAPO-34 membrane without any necessity for additional parameters.

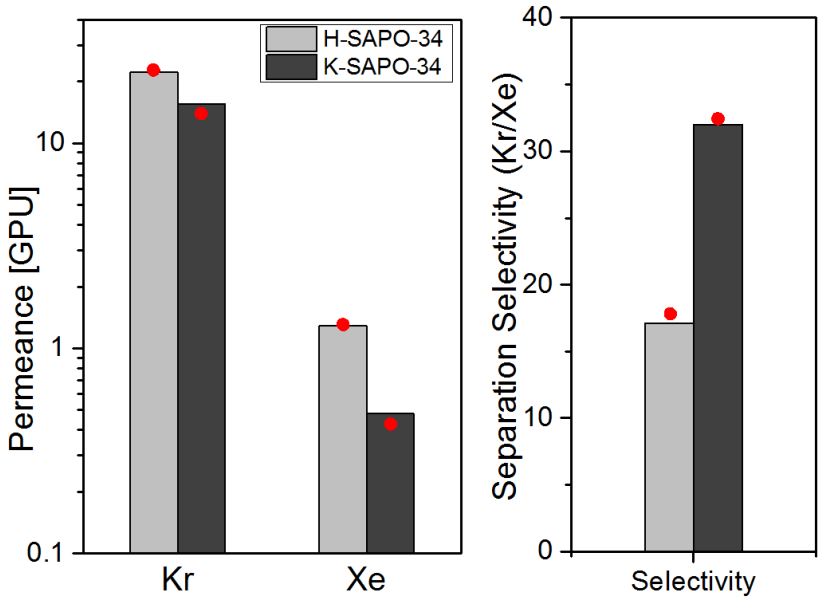

Figure 5.5. Predicted separation performance (red dot symbols) of H-SAPO-34 membrane and K-SAPO-34 membrane and comparison with experimental data at 298 K.

5.3 Process Model for Zeolite Membrane System

5.3.1 General Equations and Determination of Operating Conditions

This study employs the multi-component gas separation using a plug flow separation model (**Figure 5.6**). The governing mass balance equations for each components over a differential membrane length (*dz*) and differential membrane area (*dA*) on the retentate and permeate sides are as follows [105, 106].

$$n_i(z) - n_i(\mathrm{z} + dz) + 2\pi r J_i d\mathrm{z} = 0 \qquad (5.12)$$

where n_i is molar flow rate of component *i* along the stage length, J_i is flux of component *i* passing through the membrane.

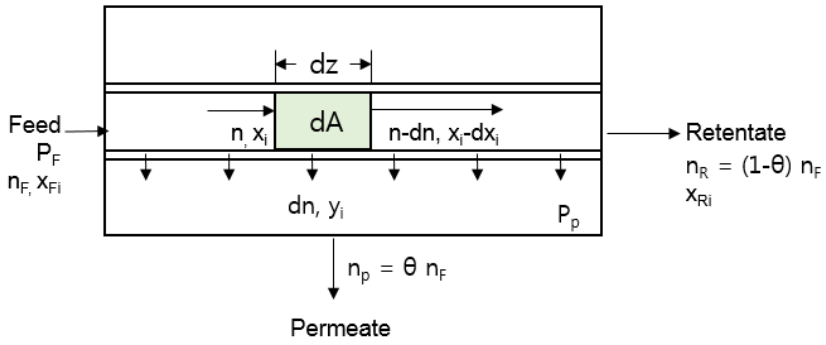

Figure 5.6. Scheme for single stage of cross-flow membrane separation system

To increase the driving force for gas separation, a sweep gas can be used as a countercurrent module to reduce the partial pressure of each gas in the permeate side. However, using sweep gas requires additional purification steps to remove undesired sweep component from permeate and retentate streams. Therefore, the zeolite membrane operation without sweep gas is considered as a simple and better configuration. Instead, depressurizing permeate stream is used to keep a certain partial pressure of Kr and Xe. **Table 5.1** shows the summary of feed conditions. Even though it was revealed from our simulation results that operations under slightly subambient temperature (250 – 280 K) can achieve higher selectivitieis, it is not practical for industrial implementations, thus membranes are assumed to be operated at ambient temperature, 298 K.

Table 5.1. Feed stream conditions for membrane system for Kr/Xe separations

Feed Composition	10 vol % Kr / 90 vol % Xe
Temperature	298 K
Flow rate	1 L/min
Pressure	100 kPa

Five different types of membranes were evaluated as potential candidates introduced in the Chapter 3 and 4 and key properties of each membrane are shown in **Table 5.2**. M1 and M2 possess different diffusivities and diffusion selectivity because M1 type membrane have more defects due to less interlocked large crystals, which makes gas molecules pass through non-zeolitic pathways. All M2 type of membranes were assumed to have same thickness with different types of cations in the framework.

Table 5.2 Key properties of SAPO-34 zeolite membranes at 298 K for evaluation

		M1	**M2**	**Li-M2**	**Na-M2**	**K-M2**
Counterbalance cation type		H+	H+	Li+	Na+	K+
Thickness [μm]		5.6	2.05	2.05	2.05	2.05
q_{sat} [mmol/g]	**Kr**	6.7	6.7	6.1	5.6	5.2
	Xe	5.2	5.2	4.8	4.4	4.1
b [* 10^{-4} kPa^{-1}]	**Kr**	9.0	9.0	8.3	8.2	8.2
	Xe	39	39	37	36	39
D [*10^{-14} m^2/s]	**Kr**	181	172	133	130	128
	Xe	3.26	2.78	1.51	1.26	1.04

Using the adsorption and diffusion properties of each membrane (M1, M2, Li-M2, Na-M2, and K-M2), the process modeling simulations were carried out for single membrane stage to obtain 99.9 % purity of Xe from the retentate stream. Our first trial of modeling included pressurizing the feed (300 – 400 kPa) and permeate stream at ambient pressure (100 kPa). However, driving force is not sufficient beyond zero stage cut because partial pressure of Kr at permeate side is expected to be 30 – 45 kPa, which is almost similar to the partial pressure of Kr at feed stream (30 – 40 kPa). Therefore, I chose to use depressurization of permeate stream (0.1 kPa) in order to obtain enough driving force.

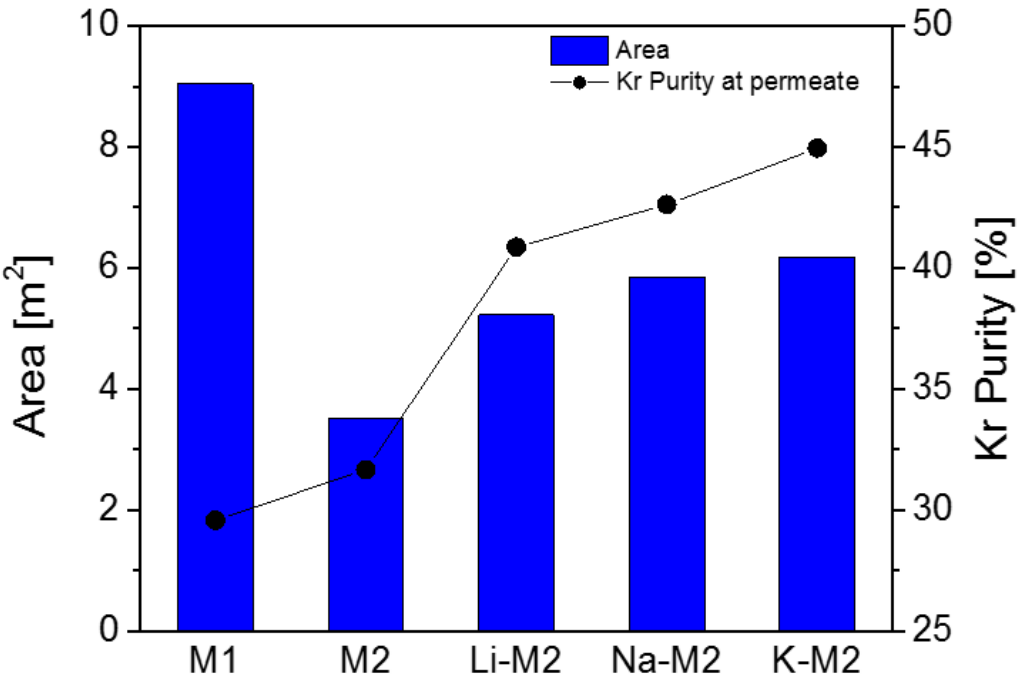

Figure 5.7. Membrane area requirement for 99.9% Xe purity and Kr purity obtained at permeate stream through a single membrane stage for each type of membrane.

As shown in **Figure 5.7**, the largest membrane area (~9 m^2) is required in case of M1 type membrane in order to achieve 99.9 % Xe from the retentate stream and the

produced Kr purity is the lowest (29.6 %). Due to slight improvement in selectivity because of decreased amount of defects and improvement in permeability, M2 membrane will require only 3.5 m^2 with 31.7 % of Kr purity. Post-synthesis ion exchange (M-M2) leads to slightly increased required area but Kr purity highly increased to ~ 40 – 45 %. Among all the membranes that I investigated, K-M2 was chosen as the best candidate because it has the sharpest separation properties with compact system size in spite of decreased permeance and modest increase in required area after ion exchange.

5.3.2 Determination of Membrane System Configuration

In the membrane separation system, single-stage membrane module is desired due to its easiness of operation and compactness [107]. However, it is very limited that the membrane can separate the feed mixture in a single stage because the number of stages can be determined by separation selectivity of the membrane [108, 109]. Several multistage membrane system configurations were evaluated. **Figure 5.8** shows the two membrane configurations considered in most detail for the Kr/Xe separation: a simple series arrangement and a cascade with recycle. For both cases, the permeate stream is enriched in Kr and fed to the next stage, and the membrane system operation continues until it reaches desired purity specifications. The membrane cascade has a recycle stream for enriching the Kr purity of the final permeate stream.

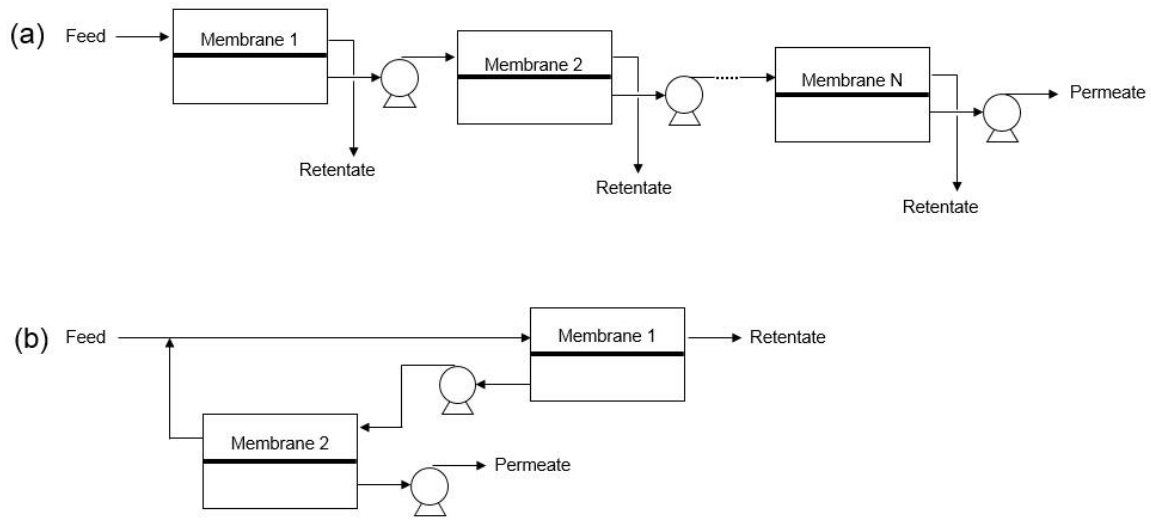

Figure 5.8. Schematic of (a) membrane modules in series and (b) two-stage enriching membrane cascade with depressurization at permeate stream using vacuum pump.

As discussed in Section 5.3.1, the K-M2 membrane is used for this evaluation since it possesses the highest selectivity of Kr/Xe. I compared 3 different purities for each component, Kr (90, 95, and 99 %) and Xe (99, 99.9, and 99.99 %). **Figure 5.9** shows that the total areas required for the cascade case are larger than those required for membrane modules in series because of the recycling step resulting in larger amount of feed to be processed through the first membranes. However, the cascade requires only two membrane stages for all cases in order to obtain the desired purity of Kr and Xe from product streams, whereas the membranes-in-series case required 2-6 membrane stages. Reduction in the number of stages is highly desirable in order to obtain savings in vacuum equipment cost and energy cost due to the requirement of vacuum pumps between the membrane stages. A membrane system requiring more than 2-3 stages makes the process cumbersome, and thus the membrane cascade is determined as a better configuration.

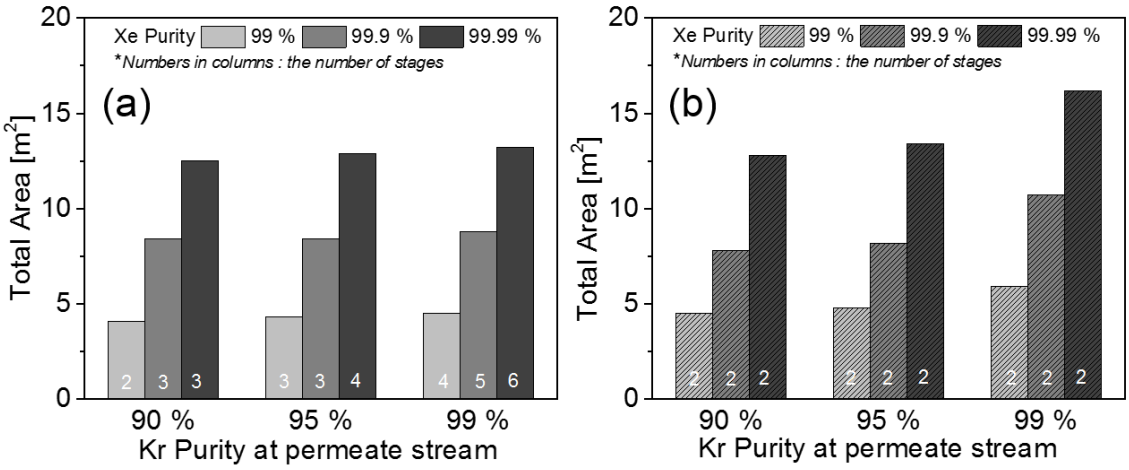

Figure 5.9. Comparison of system size and number of stages for obtaining desired purities of Kr and Xe for (a) membranes in series and (b) membrane cascade. (Membrane type = K-M2, Permeate pressure = 0.1 kPa)

5.3.3 Effect of permeate pressure on system size

In Chapter 5, I used 0.1 kPa pressure in the permeate stream so that I could achieve large driving force between feed and permeate stream. However, maintaining a permeate pressure of 0.1 kPa may not be practical for the membrane separation system in industry because of the high cost of vacuum pumps that keep the permeate stream at extremely low pressure. In addition, the energy duty of the process is mainly dominated by the pressure ratio across the membrane stages. Using our process model, it was found that it is impossible to use higher permeate pressure than 0.1 kPa for membrane in series due to insufficient driving force between feed and permeate stream. However, for the membrane cascade, it is feasible to change the permeate pressure to milder condition at around 1-5 kPa because of the existence of recycle stream. Again, three different purities of each product stream were investigated. Kr purities were identical with the previous study (90%, 95%, and 99 %) and Xe purities were expressed as “baseline” (99%), “high” (up to 99.9%), and “highest” (> 99.9%).

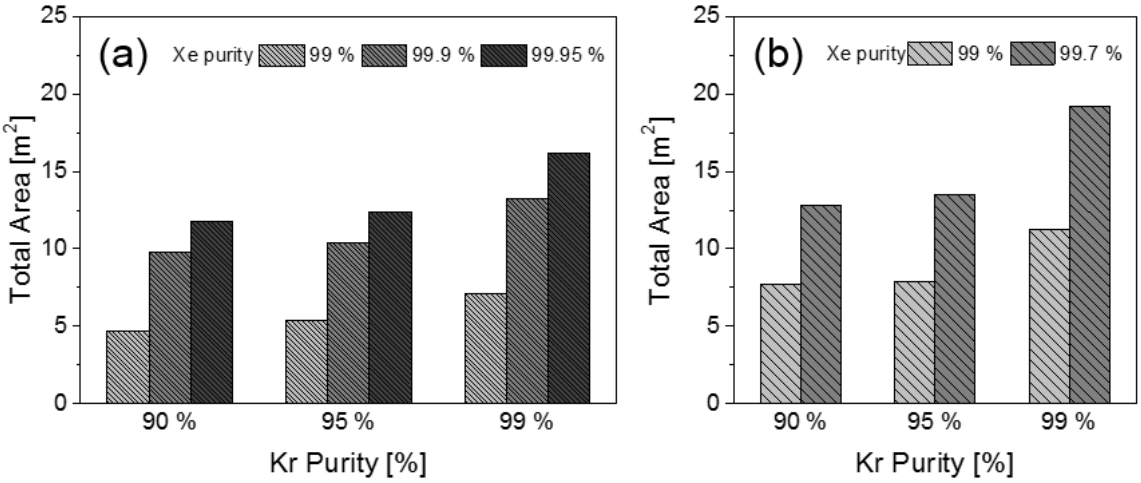

Figure 5.10. Comparison of system size for obtaining desired purities of Kr and Xe under (a) 1 kPa and (b) 5 kPa of permeate pressure. For every case, two membrane stages in the cascade are sufficient.

Figure 5.10 summarizes the permeate pressure dependence on the system size to achieve target product purities. The total area of membrane cascade system increased by 10 – 30 % compared to the results with the assumption of 0.1 kPa permeate pressure (**Figure 5.9b)** because of reduced driving force across the membrane. Even though the increase in membrane area would somewhat affect the capital cost of separation system, the total cost increment is expected to be marginal because there is a trade-off with the reduction in the energy duty. If the permeate pressure is set as 5 kPa, the two-membrane cascade with recycle would achieve the purity of product streams as high as 99.7 % Xe and 99% Kr. The total area requirements would vary in the range of 7 – 21 m^2 depending on the product purities, and this is a very compact system (when fabricated on hollow fibers) compared to cryogenic distillation.

5.4 Cost Estimation and Economic Analysis

To compare the relative advantages of the membrane system (versus cryogenic distillation) for Kr/Xe separation, it is desired to calculate the appropriate economic figures of merit. The total process cost of the membrane separation system includes (a) capital cost, (b) O&M (operation and maintenance), and (c) energy consumption [110, 111]. The capital cost of the membrane system is dominated by the membrane and equipment costs. Estimating the values for these calculations is always subject to various assumptions, therefore careful and conservative assumptions are taken into account. The fabrication price of zeolite membrane is assumed to be $\$1000/m^2$, which is a very conservative estimate of the cost of zeolite membranes especially when ceramic hollow fibers are used as substrates as shown in Chapter 4 [112]. Other assumptions and equations for estimating process capital cost are summarized in **Table 5.3**. The O&M cost of the equipment is generally assumed to be 3.6 % of its capital cost and 1.0% of its capital cost for the membrane and membrane frame [113]. The capital cost for each operating condition and target product purity can be calculated based on equations in **Table 5.3**. Capital costs are mainly determined by the size of membrane because the equipment cost is marginal compared to the membrane cost and membrane frame cost. **Figure 5.11** shows the capital cost for two-stage membrane cascade at different permeate pressures of 1 kPa and 5 kPa. As expected in previous chapter, due to increase in total membrane area caused by reduced driving force, membrane system under higher permeate pressure requires more capital cost than lower permeate pressure case.

Table 5.3. Equations for determination of process facilities capital (PFC) and O&M cost of gas separation membrane system

Estimated Investments *I* (components)	
Membrane Cost	$I_m = A_m \cdot K_m$
Membrane Frame Cost	$I_{mf} = (A_m/2000)^{0.7} \cdot K_{mf}$
Vacuum Pump	$I_{vp} = N \cdot K_{vp}$
Process Facilities Capital (PFC)	$C_{pfc} = I_m + I_{mf} + I_{vp}$
General Facilities Cost	$C_{gfc} = 0.1 \cdot C_{pfc}$
Engineering and home office fees	$C_{ehf} = 0.1 \cdot C_{pfc}$
Project Contingency Cost	$C_{project} = 0.15 \cdot C_{pfc}$
Process Contingency Cost	$C_{process} = 0.02 \cdot C_{pfc}$
Total Capital Cost	$C_{cap} = C_{pfc} + C_{gfc} + C_{ehf} + C_{project} + C_{process}$
O&M cost	$C_{O\&M} = 0.01 \cdot (I_m + I_{mf}) + 0.036 \cdot I_{vp}$

Notation: A_m: membrane area (m^2); K_m: unit cost of membrane ($1000/$m^2$); K_{mf} : $300,000; N: number of vacuum pumps ; K_{vp}: installed unit cost.

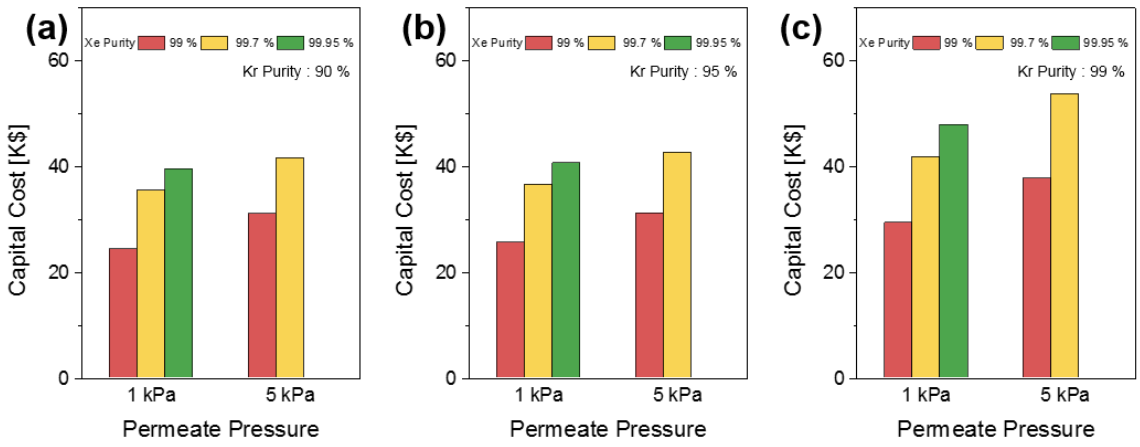

Figure 5.11. Capital cost of two-stage cascade membrane system with different permeate pressure and Xe purity when target Kr purity is **(a)** 90 % **(b)** 95 %, and **(c)** 99 %. (K$ = 10^3 $). Note that 99.9+% Xe purity is not possible with a 5 kPa permeate.

Compared to cryogenic distillation for gas separation, membrane separation is usually assumed/expected to be a less energy-intensive technology. However, it is necessary to verify this hypothesis by calculating the energy consumption per year and compare to the amount of energy consumption in cryogenic distillation. The energy consumption from vacuum pump can be calculated by using the following equation:

$$E = \frac{1}{\eta} Q_T \frac{\gamma RT}{\gamma - 1} \left[\left(\frac{p_{atm}}{p''} \right)^{(\gamma-1)/\gamma} - 1 \right] \tag{5.13}$$

where Q_T stands for the molar flow rate from permeate mixture, η for the efficiency of pump, γ for the adiabatic expansion coefficient of the downstream mixture, and p'' for the total downstream pressure. The adiabatic expansion coefficient for a mixture of Kr and Xe is assumed to be 1.67 [114]. The efficiency of the vacuum pump is taken at 80% [115]. According to Eqn 5.13, the energy consumption is highly dependent on the molar flow rate from the permeate mixture (Q_T) and ratio of feed pressure to permeate pressure. Therefore, we can expect the reduction in energy consumption as permeate pressure increases.

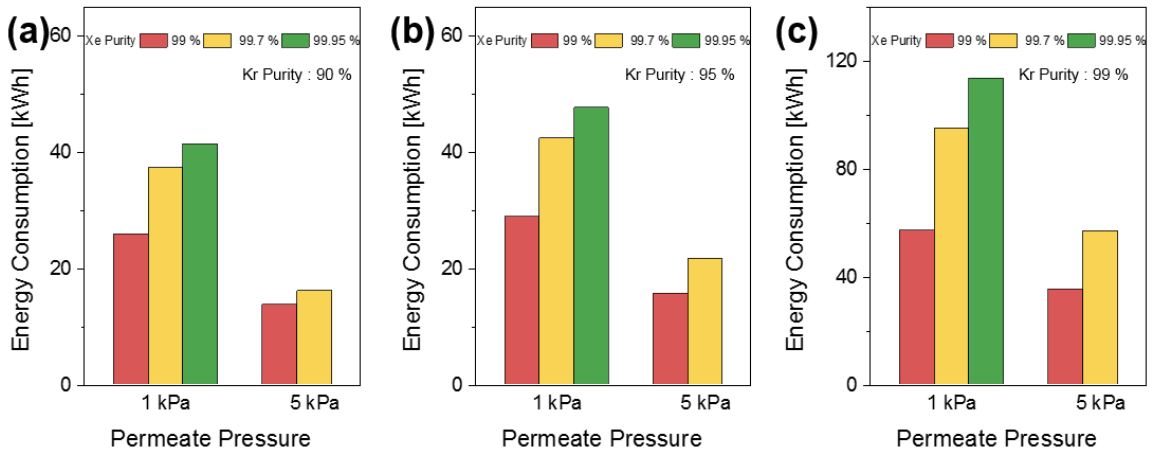

Figure 5.12. Energy duty of of two-stage cascade membrane system with different permeate pressure and Xe purity when target Kr purity is **(a)** 90 % **(b)** 95 %, and **(c)** 99 %. Note that 99.9+% Xe purity is not possible with a 5 kPa permeate.

The energy duty (in kWh) for the two-stage membrane cascade is calculated and shown in **Figure 5.12**. For every case at 5 kPa of permeate pressure, the energy consumption was about 40 – 60 % lower than the case at 1 kPa permeate pressure, according to Eqn 5.10 where the energy consumption is dependent on the pressure ratio of exhaust pressure to permeate pressure. Even though the capital cost is higher when the permeate pressure is 5 kPa, a higher permeate pressure is more desirable operating condition. The energy consumption saving is a considerable long-term factor over the 15-year operating period. Even though the calculation included different Kr purity between 90 % and 99 %, Kr purity of 90 % as a product stream is sufficient enough for saving the radioactive waste storage volume by 1/10. **Figure 5.13** shows the energy cost per year to obtain 90 % of Kr as a product stream with different permeate pressure and different Xe purity. Here the electricity cost was assumed as $ 0.08/ kW [89]. In order to produce 90% Kr and 99.7% Xe as product streams, the K-M2 membrane system will require 16.1 kWh of energy duty, which is equal to 142 MW per year of operation. This energy duty can be

converted into the energy cost, and the membrane cascade system would require $ 11,300 per year as an energy cost.

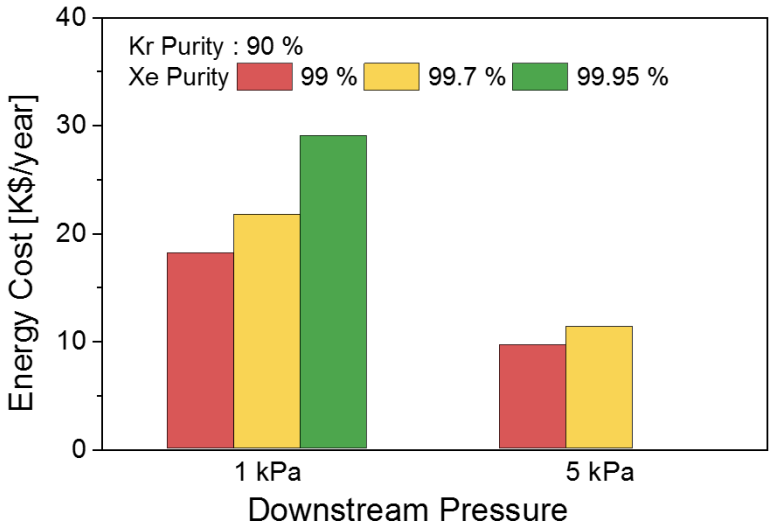

Figure 5.13. Yearly energy cost of of two-stage cascade membrane system with different permeate pressure and Xe purity when target Kr purity is 90 %. Note that 99.9+% Xe purity is not possible with a 5 kPa permeate.

For the economic assessment of membrane separation process, it is required to compare this technology with cryogenic distillation for separation of Kr/Xe. The energy duty for cryogenic distillation can be estimated using an ASPEN Plus distillation process simulator to produce Kr and Xe with same purity (90% Kr and 99.7 % Xe). The required amount of electricity for cryogenic distillation is predicted as 52 kWh and this is equivalent to 456 MW per year of operation, which is equal to $ 36,500 of energy cost per year considering the electricity cost of $0.08/kW. Therefore, I can expect to achieve ~70% energy cost savings by implementing membrane technology in Kr/Xe separation process. The ASPEN Plus simulator also estimated the total equipment cost of the cryogenic distillation system as $70,700, and the total capital cost is expected to be much higher than this value which includes contingencies. Therefore, the membrane system is

attractive in the capital cost point of view, considering much lower capital cost ($ 41,600) of the membrane system. Additionally, an important factor (neglected here due to lack of information available in open literature) is the cost of decommissioning and disposal/storage of distillation and membrane system equipment (i.e., life cycle analysis). For this reason, a formal calculation of the net present value (NPV) and cash flow for the two cases has not been carried out here. However, our calculations suggest an overwhelming advantage for the membrane-based process from both the energy and capital cost standpoints.

5.5 Conclusion

In this chapter, I investigated the economic viability of a SAPO-34 zeolite membrane system configuration for the separation of Kr/Xe mixtures produced as off-gas during nuclear fuel reprocessing. A Maxwell-Stefan model for this application has been developed by using the adsorption and diffusion parameters obtained from the experimental results. With appropriate assumptions, the M-S model showed a great agreement with the experimental results from single component and binary mixture permeation, especially because the synthesized membranes were defect-free. The M-S model of Kr/Xe permeation in K-SAPO-34 membrane (thickness = 2.1 μm) was then integrated into an overall model of a cross-flow tubular/hollow fiber membrane module to perform a system analysis for the estimation of required system size and total cost. A single stage is not expected to produce purified Kr stream. Therefore, a multistage membrane system was designed to produce Kr and Xe with higher purity. Rather than

using membranes in series, the membrane cascade configuration was found to be more suitable due to a smaller number of stages and its milder operating permeate pressure conditions up to 5 kPa. At 5 kPa of permeate pressure and feed pressure at 100 kPa, the required system size to handle 1 L/min of feed stream (10 % Kr / 90 % Xe mixture) was calculated as 13 m^2 in order to achieve 90 % Kr and 99.7 % Xe as two product streams. The size of system is considered as very compact and simple compared to cryogenic distillation, of which configuration is expected to be relatively complicated. The membrane system was found to be economically attractive and less energy intensive compared to cryogenic distillation, saving approximately 70% of energy cost. Based upon our calculation of the membrane capital cost and the ASPEN Plus estimate of cryogenic distillation capital cost, the membrane system is highly favorable also from a capital cost point of view. However, life cycle costs (including decommissioning and storage/disposal of equipment after radioactive exposure) are not included in the analysis for either the distillation or the membrane system.

CHAPTER 6. CONCLUSIONS AND FUTURE WORK

6.1 Main Findings

The aim of this thesis has been to develop multiple aspects of a Kr/Xe separation membrane technology. By implementing an economical Kr/Xe separation step in the nuclear fuel cycle, we can yield the reduction of the radioactive waste volume to 1/10 containing ^{85}Kr and can generate revenue from the sale of purified Xe, which is a noble gas with a high demand in various industries such as electronics, lighting and the medical industry. The first two parts of this thesis focused on SAPO-34 crystals and membrane synthesis to explain the transport properties of Kr and Xe in SAPO-34. Even though there exist a competing effect on adsorption selectivity and diffusion selectivity in Kr and Xe mixture, the experimental results and adsorption modeling indicated a high potential of SAPO-34 membrane for the use in Kr-Xe separation membranes. Indeed, SAPO-34 membranes could separate Kr and Xe effectively once steam-assisted conversion seeding method was introduced as seeding protocol. From the defect-free membrane, Kr permeance was found to be ~10 GPU with Kr/Xe selectivity of 18 in a binary mixture condition. Highly reproducible synthesis procedure using SAC method indicated that high quality SAPO-34 membranes can be synthesized on a macroporous ceramic substrates with reasonable price.

Even though SAPO-34 membranes have shown promising results in separation of Kr/Xe, I extended this work in order to make the zeolite membrane more favorable in separation industry that can substitute current separation method. In our attempts to reduce the manufacturing cost of zeolite membrane, three aspects were taken into

account. By controlling the amount of steam-assisted conversion (SAC) gel, it was available to reduce the thickness of the membrane resulting in dramatic increase in permeance (Kr permeance = 28 GPU) and improved separation selectivity by 30 % (Kr/Xe = 22). The improvement of flux lead to a direct reduction in membrane area to produce Kr and Xe. In order to increase the Kr permeation selectivity, post-synthesis cation exchange was introduced which was hypothesized to control the molecular sieving properties of SAPO-34 membrane by maximizing the molecular sieving properties of SAPO-34. Although there was slight decrease in Kr permeance to 16 GPU, the separation selectivity of Kr/Xe showed a great improvement to 32. The separation selectivity is closely related to the number of required stages, thus a reduced number of stages and system size were expected. Finally, the optimized synthesis protocol was transferred to ceramic hollow fiber substrates with Kr permeance of 14 GPU and separation factor of 31. In general, ~ 75 % of manufacturing cost comes from the substrates supporting the zeolite membranes. Therefore, the price of zeolite membranes would decrease greatly *via* successful synthesis of SAPO-34 membranes on ceramic hollow fiber substrates.

The Maxwell-Stefan model of Kr/Xe separation was developed for prediction of Kr/Xe permeation properties in SAPO-34 membranes. Since the simulation results presented a great agreement with experimental data, a detailed mathematical model of a zeolite membrane system was then developed for Kr/Xe separation under a wide range of operating conditions by embedding M-S model within a membrane system model for a cross flow configuration. Among 5 different types of membranes that I investigated, potassium exchanged SAPO-34 membrane was chosen as the best candidate showing the sharpest separation properties. The optimal membrane system configuration was

determined as two-stage membrane cascade module with recycle and the size of membrane separation process was also calculated. The usage of mild permeate vacuum pressure at 5 kPa can achieve two product streams with high purity of 90 % Kr and 99.7 % Xe. For 1 L/min feed stream containing 10 % Kr and 90 % Xe, the total area of membrane to produce this product specification is estimated as 13 m^2 and the energy duty of this system 16.1 kWh, which is highly energy saving process compared to cryogenic distillation with the energy duty of 52 kWh.

6.2 Future Work and Challenges

6.2.1 Demonstrating scale up of SAPO-34 membrane system

In this work, SAPO-34 membranes were successfully synthesized on α-alumina ceramic hollow fibers. This high quality SAPO-34 hollow fiber membrane showed the possibility to realize a compact and low cost separation system using zeolite membrane. To my best knowledge, there is no existence in SAPO-34 membrane scale-up using hollow fiber substrates but the only effort has been made for scale-up using stainless steel supports up to 25 cm length. Compared to tubular substrates which can achieve 600 – 800 m^2/m^3 packing density, we can obtain much higher packing density of 2000 – 4000 m^2/m^3 by exploiting high surface to volume ratio of hollow fiber modules, resulting in compact and economical system. In future work, it is desired to focus on scale-up of SAPO-34 membrane in engineering point of view. Other than Kr/Xe separation introduced in this study, there are many plausible applications of SAPO-34 membranes such as CO_2/CH_4 separation in natural gas processing. Moreover, previous research found

that post-synthesis ion exchange of SAPO-34 can exhibit improved separation properties of CO_2/CH_4 [71] and a facile ion exchange procedure using vacuum filtration was developed at Georgia Tech by S.J. Kim et al [76]. In addition to scale-up of membrane system, defect control strategies must be taken into consideration. Since it is not easy to synthesize 100% defect-free membranes, the strategies to heal the defects may be a possible requirement.

6.2.2 Generalized applications of the Steam-Assisted Conversion method

The steam-assisted conversion seeding method could realize the fabrication of defect-free SAPO-34 membrane on any type of porous substrate with high reproducibility. The SAC method can potentially be used to create continuous crystalline "proto-membrane" layers on ceramic substrates. The SAC method has only been used for producing the seed crystal layer on the substrate, which is always followed by the secondary hydrothermal growth to close the gaps between the crystals. So far, synthesis of selective zeolitic membranes without hydrothermal secondary growth has not been developed, but it is highly desirable to remove the hydrothermal growth step from the scale-up standpoint. Therefore, further study on SAC to extend the membrane synthesis protocol without hydrothermal growth would be meaningful to produce defect-free zeolite as well as zeolite-MOF hybrid/composite membranes for a range of possible applications.

REFERENCES

[1] Strategy for the Management and Disposal of Used Nuclear Fuel and High-Level Radioactive Waste. US Department of Energy. Washington, DC2013.

[2] Marques JG. Evolution of nuclear fission reactors: Third generation and beyond. Energy Conversion and Management 2010;51:1774-80.

[3] World Nuclear Performance Report 2017. World Nuclear Association; 2017.

[4] Shmidt OV, Makeeva IR, Liventsov SN. Modeling Closed Nuclear Fuel Cycle Processes. Procedia Chemistry 2016;21:503-8.

[5] Jubin R. Spent Fuel Reprocessing. Introduction to Nuclear Chemistry and Fuel Cycle Separations Course, Consortium for Risk Evaluation With Stakeholder Participation2008.

[6] Crawford PG. Zeolite membranes for the separation of krypton and xenon from spent nuclear fuel reprocessing off-gas. SMARTech Georgia Tech Theses and Dissertations: Georgia Institue of Technology; 2013.

[7] Bhave R, Koros W, Jubin R. Zeolite Membranes for the Capture of Krypton and Xenon from Voloxidation and Dissolve Off-gas. Unpublished Proposal: Oak Ridge National Laboratory, Oak Ridge, TN.; 2011.

[8] Jubin RT, DelCul GD, Patton BD, Owens RS, Ramey DW, Spencer BB. Advanced Fuel Cycle Initiative Coupled End-to-End Research, Development, and Demonstration Project: Integrated Off-Gas Treatment System Design and Initial Performance-9226. Waste Management Conference 2009. Phoenix, AZ2009.

[9] Haefner D, Law J, Tranter T. System Design Description and Requirements for Modeling the Off-Gas Systems for Fuel Recycling Facilities. INL-2010. INL-2010: Idaho National Laboratory; 2010.

[10] Gombert D. Global Nuclear Energy Partnership: Integrated Waste Management Strategy. Waste Treatment Baseline Study. DOE Report GNEP-WAST-WAST-AI-RT-2007-0003242007.

[11] Liu J, Fernandez CA, Martin PF, Thallapally PK, Strachan DM. A Two-Column Method for the Separation of Kr and Xe from Process Off-Gases. Industrial & Engineering Chemistry Research 2014;53:12893-9.

[12] Bazan RE, Bastos-Neto M, Moeller A, Dreisbach F, Staudt R. Adsorption equilibria of O2, Ar, Kr and Xe on activated carbon and zeolites: single component and mixture data. Adsorption 2011;17:371-83.

[13] Thallapally PK, Grate JW, Motkuri RK. Facile xenon capture and release at room temperature using a metal-organic framework: a comparison with activated charcoal. Chemical communications 2012;48:347-9.

[14] Jameson CJ, Jameson AK, Lim H-M. Competitive adsorption of xenon and krypton in zeolite NaA: 129Xe nuclear magnetic resonance studies and grand canonical Monte Carlo simulations. The Journal of Chemical Physics 1997;107:4364-72.

[15] Banerjee D, Simon CM, Plonka AM, Motkuri RK, Liu J, Chen X, et al. Metal-organic framework with optimally selective xenon adsorption and separation. Nature communications 2016;7:ncomms11831.

[16] Banerjee D, Cairns AJ, Liu J, Motkuri RK, Nune SK, Fernandez CA, et al. Potential of metal-organic frameworks for separation of xenon and krypton. Accounts of chemical research 2015;48:211-9.

[17] Fernandez CA, Liu J, Thallapally PK, Strachan DM. Switching Kr/Xe selectivity with temperature in a metal-organic framework. Journal of the American Chemical Society 2012;134:9046-9.

[18] Liu J, Thallapally PK, Strachan D. Metal-organic frameworks for removal of Xe and Kr from nuclear fuel reprocessing plants. Langmuir 2012;28:11584-9.

[19] Banerjee D, Simon CM, Elsaidi SK, Haranczyk M, Thallapally PK. Xenon Gas Separation and Storage Using Metal-Organic Frameworks. Chem 2018;4:466-94.

[20] Xiong S, Gong Y, Hu S, Wu X, Li W, He Y, et al. A microporous metal–organic framework with commensurate adsorption and highly selective separation of xenon. Journal of Materials Chemistry A 2018;6:4752-8.

[21] Wu T, Feng X, Elsaidi SK, Thallapally PK, Carreon MA. Zeolitic Imidazolate Framework-8 (ZIF-8) Membranes for Kr/Xe Separation. Industrial & Engineering Chemistry Research 2017;56:1682-6.

[22] Eum K, Jayachandrababu KC, Rashidi F, Zhang K, Leisen J, Graham S, et al. Highly tunable molecular sieving and adsorption properties of mixed-linker zeolitic imidazolate frameworks. Journal of the American Chemical Society 2015;137:4191-7.

[23] Wu T, Lucero J, Zong Z, Elsaidi SK, Thallapally PK, Carreon MA. Microporous Crystalline Membranes for Kr/Xe Separation: Comparison Between AlPO-18, SAPO-34, and ZIF-8. ACS Applied Nano Materials 2018;1:463-70.

[24] Wu T, Wang B, Lu Z, Zhou R, Chen X. Alumina-supported AlPO-18 membranes for CO2/CH4 separation. Journal of Membrane Science 2014;471:338-46.

[25] Wang B, Hu N, Wang H, Zheng Y, Zhou R. Improved AlPO-18 membranes for light gas separation. Journal of Materials Chemistry A 2015;3:12205-12.

[26] Li S, Carreon MA, Zhang Y, Funke HH, Noble RD, Falconer JL. Scale-up of SAPO-34 membranes for CO2/CH4 separation. Journal of Membrane Science 2010;352:7-13.

[27] Bernardo P, Drioli E, Golemme G. Membrane Gas Separation: A Review/State of the Art. Industrial & Engineering Chemistry Research 2009;48:4638-63.

[28] Baker RW. Membranes for vapor/gas separations. 2006.

[29] Ghanem BS, Swaidan R, Litwiller E, Pinnau I. Ultra-microporous triptycene-based polyimide membranes for high-performance gas separation. Adv Mater 2014;26:3688-92.

[30] Sanders DF, Smith ZP, Guo R, Robeson LM, McGrath JE, Paul DR, et al. Energy-efficient polymeric gas separation membranes for a sustainable future: A review. Polymer 2013;54:4729-61.

[31] Kim TH, Koros WJ, Husk GR, O'Brien KC. Relationship between gas separation properties and chemical structure in a series of aromatic polyimides. Journal of Membrane Science 1988;37:45-62.

[32] Stern SA, Mi Y, Yamamoto H, Clair AKS. Structure/permeability relationships of polyimide membranes. Applications to the separation of gas mixtures. Journal of Polymer Science Part B: Polymer Physics 1989;27:69-86.

[33] Kim JH, Koros WJ, Paul DR. Effects of CO2 exposure and physical aging on the gas permeability of thin 6FDA-based polyimide membranes: Part 2. with crosslinking. Journal of Membrane Science 2006;282:32-43.

[34] Lin W-H, Chung T-S. Gas permeability, diffusivity, solubility, and aging characteristics of 6FDA-durene polyimide membranes. Journal of Membrane Science 2001;186:183-93.

[35] Wang L, Cao Y, Zhou M, Zhou SJ, QuanYuan. Novel copolyimide membranes for gas separation. 2007 2007;305:338-46.

[36] Cheetham AK, FeÂrey G, Loiseau T. Open-Framework Inorganic Materials. 1999 1999;38:3268-92.

[37] Shao J, Zhan Z, Li J, Wang Z, Li K, Yan Y. Zeolite NaA membranes supported on alumina hollow fibers: Effect of support resistances on pervaporation performance. Journal of Membrane Science 2014;451:10-7.

[38] Li H, Wang J, Xu J, Meng X, Xu B, Yang J, et al. Synthesis of zeolite NaA membranes with high performance and high reproducibility on coarse macroporous supports. Journal of Membrane Science 2013;444:513-22.

[39] Peng Y, Zhan Z, Shan L, Li X, Wang Z, Yan Y. Preparation of zeolite MFI membranes on defective macroporous alumina supports by a novel wetting–rubbing seeding method: Role of wetting agent. Journal of Membrane Science 2013;444:60-9.

[40] Zhou R, Ping EW, Funke HH, Falconer JL, Noble RD. Improving SAPO-34 membrane synthesis. Journal of Membrane Science 2013;444:384-93.

[41] Auerbach SM, Carrado KA, Dutta PK. Handbook of Zeolite Science and Technology: CRC Press; 2003.

[42] Morigamia Y, Kondo M, Abe J, Kita H, Okamoto K. The first large-scale pervaporation plant using tubular-type module with zeolite NaA membrane. Separation and Purification Technology 2001;25:251-60.

[43] Rangnekar N, Mittal N, Elyassi B, Caro J, Tsapatsis M. Zeolite membranes - a review and comparison with MOFs. Chemical Society reviews 2015;44:7128-54.

[44] Li S. SAPO-34 membranes for CO2/CH4 separation. Journal of Membrane Science 2004;241:121-35.

[45] Li S, Martinek JG, Falconer JL, Noble RD. High-Pressure CO2/CH4 Separation Using SAPO-34 Membranes. Industrial & Engineering Chemistry Research 2005;44:3220-8.

[46] Ianovski D, Munakata K, Kanjo S, Yokoyama Y, Koga A, Yamatsuki S, et al. Adsorption of Noble Gases on H-Mordenite. Journal of Nuclear Science and Technology 2002;39:1213-8.

[47] Gurdal Y, Keskin S. Atomically Detailed Modeling of Metal Organic Frameworks for Adsorption, Diffusion, and Separation of Noble Gas Mixtures. Industrial & Engineering Chemistry Research 2012;51:7373-82.

[48] Krishna R, Broeke LJPvd. The Maxwell-Stefan description of mass transport across zeolite membranes. The Chemical Engineering Journal and the Biochemical Engineering Journal 1995;57:155-62.

[49] Zhang C, Lively RP, Zhang K, Johnson JR, Karvan O, Koros WJ. Unexpected Molecular Sieving Properties of Zeolitic Imidazolate Framework-8. The journal of physical chemistry letters 2012;3:2130-4.

[50] Murthi M, Snurr RQ. Effects of Molecular Siting and Adsorbent Heterogeneity on the Ideality of Adsorption Equilibria. Langmuir 2004;20:2489-97.

[51] Goldberg S, Criscenti LJ, Turner DR, Davis JA, Cantrell KJ. Adsorption–Desorption Processes in Subsurface Reactive Transport Modeling. Vadose Zone Journal 2007;6:407.

[52] MYERS AL, PRAUSNITZ JM. Thermodynamics of Mixed-Gas Adsorption. AIChE journal 1965;11:121-7.

[53] Challa SR, Sholl DS, Johnson JK. Adsorption and separation of hydrogen isotopes in carbon nanotubes: Multicomponent grand canonical Monte Carlo simulations. The Journal of Chemical Physics 2002;116:814-24.

[54] Krishna R. Diffusion of binary mixtures in zeolites: molecular dynamics simulations versus Maxwell–Stefan theory. Chemical Physics Letters 2000;326:477-84.

[55] Liu H. Transport diffusivity of propane and propylene inside SWNTs from equilibrium molecular dynamics simulations. Physical chemistry chemical physics : PCCP 2014;16:24697-703.

[56] Li S, Fan CQ. High-Flux SAPO-34 for CO2/N2 Separation. Industrial & Engineering Chemistry Research 2010;49:4399-404.

[57] Chew TL, Ahmad AL, Bhatia S. Ba-SAPO-34 membrane synthesized from microwave heating and its performance for CO2/CH4 gas separation. Chemical Engineering Journal 2011;171:1053-9.

[58] Catherine M. Zimmerman, Anshu Singh, Koros WJ. Diffusion in gas separation membrane materials: A comparison and analysis of experimental characterization techniques. Journal of Polymer Science Part B : Polymer Physics 1998;36:1747-55.

[59] Nugent P, Belmabkhout Y, Burd SD, Cairns AJ, Luebke R, Forrest K, et al. Porous materials with optimal adsorption thermodynamics and kinetics for CO2 separation. Nature 2013;495:80-4.

[60] Hong M, Li S, Falconer JL, Noble RD. Hydrogen purification using a SAPO-34 membrane. Journal of Membrane Science 2008;307:277-83.

[61] Kim J-Y, Kim J, Yang S-T, Ahn W-S. Mesoporous SAPO-34 with amine-grafting for CO2 capture. Fuel 2013;108:515-20.

[62] Zhang C, Lively RP, Zhang K, Johnson JR, Karvan O, Koros WJ. Unexpected Molecular Sieving Properties of Zeolitic Imidazolate Framework-8. The journal of physical chemistry letters 2012;3:2130-4.

[63] Ruthven DM, Loughlin KF. The effect of crystallite shape and size distribution on diffusion measurements in molecular sieves. Chemical Engineering Science 1971;26:577-84.

[64] Kassaee MH, Sholl DS, Nair S. Preparation and Gas Adsorption Characteristics of Zeolite MFI Crystals with Organic-Functionalized Interiors. The Journal of Physical Chemistry C 2011;115:19640-6.

[65] Zhou L, Yang J, Li G, Wang J, Zhang Y, Lu J, et al. Highly H2 permeable SAPO-34 membranes by steam-assisted conversion seeding. International Journal of Hydrogen Energy 2014;39:14949-54.

[66] Huang A, Lin YS, Yang W. Synthesis and properties of A-type zeolite membranes by secondary growth method with vacuum seeding. Journal of Membrane Science 2004;245:41-51.

[67] Zhang Y, Avila AM, Tokay B, Funke HH, Falconer JL, Noble RD. Blocking defects in SAPO-34 membranes with cyclodextrin. Journal of Membrane Science 2010;358:7-12.

[68] PILLAY KKS. A REVIEW OF THE RADIATION STABILITY OF ION EXCHANGE MATERIALS Journal of Radioanalytical and Nuclear Chemistry 1986;102:247-68.

[69] DANIELS EA, Puri M. PHYSICO-CHEMICAL INVESTIGATIONS OF GAMMA-IRRADIATED ZEOLITE-4A International Journal of Radiation Applications and Instrumentation Part C Radiation Physics and Chemistry 1986;27:225-7.

[70] Wang LM, Chen J, Ewing RC. Radiation and thermal effects on porous and layer structured materials as getters of radionuclides. Current Opinion in Solid State and Materials Science 2004;8:405-18.

[71] Hong M, Li S, Funke HF, Falconer JL, Noble RD. Ion-exchanged SAPO-34 membranes for light gas separations. Microporous and Mesoporous Materials 2007;106:140-6.

[72] Feng X, Zong Z, Elsaidi SK, Jasinski JB, Krishna R, Thallapally PK, et al. Kr/Xe Separation over a Chabazite Zeolite Membrane. Journal of the American Chemical Society 2016;138:9791-4.

[73] Kwon YH, Kiang C, Benjamin E, Crawford P, Nair S, Bhave R. Krypton-xenon separation properties of SAPO-34 zeolite materials and membranes. AIChE Journal 2017;63:761-9.

[74] Bernardo P, Drioli E, Golemme G. Membrane Gas Separation: A Review/State of the Art. Industrial & Engineering Chemistry Research 2009;48:4638-63.

[75] Li M, Zhang J, Liu X, Wang Y, Liu C, Hu D, et al. Synthesis of high performance SAPO-34 zeolite membrane by a novel two-step hydrothermal synthesis + dry gel conversion method. Microporous and Mesoporous Materials 2016;225:261-71.

[76] Kim S-J, Liu Y, Moore JS, Dixit RS, Pendergast JG, Sholl D, et al. Thin Hydrogen-Selective SAPO-34 Zeolite Membranes for Enhanced Conversion and Selectivity in Propane Dehydrogenation Membrane Reactors. Chemistry of Materials 2016;28:4397-402.

[77] Huang Y, Wang L, Song Z, Li S, Yu M. Growth of High-Quality, Thickness-Reduced Zeolite Membranes towards N2 /CH4 Separation Using High-Aspect-Ratio Seeds. Angewandte Chemie 2015;54:10843-7.

[78] Zong Z, Feng X, Huang Y, Song Z, Zhou R, Zhou SJ, et al. Highly permeable N2 /CH4 separation SAPO-34 membranes synthesized by diluted gels and increased crystallization temperature. Microporous and Mesoporous Materials 2016;224:36-42.

[79] Pastore HO, Coluccia S, Marchese L. POROUS ALUMINOPHOSPHATES :From Molecular Sieves to Designed Acid Catalysts. Annual Review of Materials Research 2005;35:351-95.

[80] Civalleri B, Ferrari AM, Llunell M, Orlando R, Me´rawa M, Ugliengo P. Cation Selectivity in Alkali-Exchanged Chabazite: An ab Initio Periodic Study. Chemistry of Materials 2003;15:3996-4004.

[81] Hartmann M, Kevan L. Transition-Metal Ions in Aluminophosphate and Silicoaluminophosphate Molecular Sieves: Location, Interaction with Adsorbates and Catalytic Properties. Chemical Reviews 1999;99:635-64.

[82] Calligaris M, Nardin G. Cation site location in hydrated chabazites. Crystal structure of barium- and cadmium- exchanged chabazites. ZEOLITES 1982;2:200-4.

[83] Fischer M, Bell RG. Cation-exchanged SAPO-34 for adsorption-based hydrocarbon separations: predictions from dispersion-corrected DFT calculations. Physical chemistry chemical physics : PCCP 2014;16:21062-72.

[84] Smith LJ, Eckert H, Cheetham AK. Site Preferences in the Mixed Cation Zeolite, Li,Na-Chabazite: A Combined Solid-State NMR and Neutron Diffraction Study. Journal of the American Chemical Society 2000;122:1700-8.

[85] Wang Z, Yan Y. Controlling Crystal Orientation in Zeolite MFI Thin Films by Direct In Situ Crystallization. Chemistry of Materials 2001;13:1101-7.

[86] Yuan W, Lin YS, Yang W. Molecular Sieving MFI-Type Zeolite Membranes for Pervaporation Separation of Xylene Isomers. Journal of the American Chemical Society 2004;126:4776-7.

[87] Choi J, Jeong H-K, Snyder MA, Stoeger JA, Masel RI, Tsapatsis M. Grain Boundary Defect Elimination in a Zeolite Membrane by Rapid Thermal Processing. Science 2009;325:590-3.

[88] Sebastian V, Kumakiri I, Bredesen R, Menendez M. Zeolite membrane for CO2 removal: Operating at high pressure. Journal of Membrane Science 2007;292:92-7.

[89] Lin H, He Z, Sun Z, Kniep J, Ng A, Baker RW, et al. CO 2 -selective membranes for hydrogen production and CO 2 capture – Part II: Techno-economic analysis. Journal of Membrane Science 2015;493:794-806.

[90] Lin H, He Z, Sun Z, Vu J, Ng A, Mohammed M, et al. CO2-selective membranes for hydrogen production and CO2 capture – Part I: Membrane development. Journal of Membrane Science 2014;457:149-61.

[91] Wang Z, Ge Q, Shao J, Yan Y. High Performance Zeolite LTA Pervaporation Membranes on Ceramic Hollow Fibers by Dipcoating-Wiping Seed Deposition. Journal of the American Chemical Society 2009;131:6910-1.

[92] Kapteijn F, Moulijn JA, Krishna R. The generalized Maxwell-Stefan model for diffusion in zeolites: sorbate molecules with different saturation loadings. Chemical Engineering Science 2000;55:2923-30.

[93] Krishna R, Paschek D. Separation of hydrocarbon mixtures using zeolite membranes: a modelling approach combining molecular simulations with the Maxwell–Stefan Theory. Separation and Purification Technology 2000;21:111-36.

[94] Krishna R, Baur R. Modelling issues in zeolite based separation processes. Separation and Purification Technology 2003;33:213-54.

[95] Krishna R, Li S, van Baten JM, Falconer JL, Noble RD. Investigation of slowing-down and speeding-up effects in binary mixture permeation across SAPO-34 and MFI membranes. Separation and Purification Technology 2008;60:230-6.

[96] Skoulidas AI, Sholl DS, Krishna R. Correlation Effects in Diffusion of CH4/CF4 Mixtures in MFI Zeolite. A Study Linking MD Simulations with the Maxwell−Stefan Formulation. Langmuir 2003;19:7977-88.

[97] Yu M, Falconer J, Noble R, Krishna R. Modeling transient permeation of polar organic mixtures through a MFI zeolite membrane using the Maxwell–Stefan equations. Journal of Membrane Science 2007;293:167-73.

[98] Chmelik C, Heinke L, Kärger J, Schmidt W, Shah DB, van Baten JM, et al. Inflection in the loading dependence of the Maxwell–Stefan diffusivity of iso-butane in MFI zeolite. Chemical Physics Letters 2008;459:141-5.

[99] Zhai H, Rubin ES. A Two-Stage Membrane System with Air Sweep for Postcombustion Carbon Capture and Storage. 2018.

[100] Zhai H, Rubin ES. Techno-economic assessment of polymer membrane systems for postcombustion carbon capture at coal-fired power plants. Environmental science & technology 2013;47:3006-14.

[101] Bounaceur R, Lape N, Roizard D, Vallieres C, Favre E. Membrane processes for post-combustion carbon dioxide capture: A parametric study. Energy 2006;31:2556-70.

[102] Aprile E, Aalbers J, Agostini F, Alfonsi M, Amaro FD, Anthony M, et al. Removing krypton from xenon by cryogenic distillation to the ppq level. The European Physical Journal C 2017;77.

[103] Abe K, Hosaka J, Iida T, Ikeda M, Kobayashi K, Koshio Y, et al. Distillation of liquid xenon to remove krypton. Astroparticle Physics 2009;31:290-6.

[104] Burggraafa AJ, Vroonb ZAEP, Keizera K, Verweij H. Permeation of single gases in thin zeolite MFI membranes. Journal of Membrane Science 1998;144:77-86.

[105] Mittal N, Bai P, Kelloway A, Siepmann JI, Daoutidis P, Tsapatsis M. A Mathematical Model for Zeolite Membrane Module Performance and its Use for Techno-Economic Evaluation of Improved Energy Efficiency Hybrid Membrane-Distillation Processes for Butane Isomer Separations. Journal of Membrane Science 2016.

[106] Seader JD, Henley EJ, Roper DK. Separation process principles: chemical and biochemical operiations. 3 ed: Wiley; 2011.

[107] Muellerlanger F, Tzimas E, Kaltschmitt M, Peteves S. Techno-economic assessment of hydrogen production processes for the hydrogen economy for the short and medium term. International Journal of Hydrogen Energy 2007;32:3797-810.

[108] Brunetti A, Drioli E, Lee YM, Barbieri G. Engineering evaluation of CO2 separation by membrane gas separation systems. Journal of Membrane Science 2014;454:305-15.

[109] Binns M, Lee S, Yeo Y-K, Lee JH, Moon J-H, Yeo J-g, et al. Strategies for the simulation of multi-component hollow fibre multi-stage membrane gas separation systems. Journal of Membrane Science 2016;497:458-71.

[110] Yang D, Wang Z, Wang J, Wang S. Potential of Two-Stage Membrane System with Recycle Stream for CO2Capture from Postcombustion Gas. Energy & Fuels 2009;23:4755-62.

[111] Ho MT, Leamon G, Allinson GW, Wiley DE. Economics of CO2 and Mixed Gas Geosequestration of Flue Gas using Gas Separation Membranes. Industrial & Engineering Chemistry Research 2006;45:2546-52.

[112] Caro J. Are MOF membranes better in gas separation than those made of zeolites? Current Opinion in Chemical Engineering 2011;1:77-83.

[113] Zhao L, Riensche E, Blum L, Stolten D. Multi-stage gas separation membrane processes used in post-combustion capture: Energetic and economic analyses. Journal of Membrane Science 2010;359:160-72.

[114] Adiabatic Index for all the elements in the Periodic Table. Wolfram Research, Inc: Wolfram Research, Inc.

[115] Merkel TC, Lin H, Wei X, Baker R. Power plant post-combustion carbon dioxide capture: An opportunity for membranes. Journal of Membrane Science 2010;359:126-39.